Inaugural dissertation

for

obtaining the doctoral degree

of the

Combined Faculty of Mathematics, Engineering and Natural Sciences

of the

Ruprecht - Karls - University

Heidelberg

Presented by

M.Sc. (Molecular Biotechnology) Moritz Jakab

Born in: Heidenheim, Germany

Oral examination: 20.03.2023

Vascular control of metastatic tumor cell fates

Referees:

Prof. Dr. Ana Martin-Villalba

Prof. Dr. Hellmut G. Augustin

The presented research was carried out in the department of Vascular Oncology and Metastasis at the German Cancer Research Center (DKFZ), Heidelberg, Germany, between October 2016 and September 2022.

Acknowledgments

I would like to take the opportunity to thank all the people who supported and guided me.

First and foremost I would like to thank my Ph.D. supervisor and mentor **Prof. Dr. Hellmut Augustin** for his continuous guidance, his belief in my capabilities, and his trust in my scientific work, which was evidenced by the great scientific freedom I enjoyed and his patience and understanding he showed when things were off to a very slow start. It's been an eventful 6 years, which exposed me to all facets of academic research and gave me a clear picture of what life as a scientist is all about. Upon my arrival in the lab, you said it was your primary duty as a mentor to provide opportunities and I would like to think that I took full advantage of that.

I am thankful to **Prof. Dr. Ana Martin-Villalba** for serving as my Prüfungsvorsitz and, hence, enabling me to pursue my doctorate in the combined faculties of Natural Sciences and Mathematics of the Ruprecht-Karls-Universität of Heidelberg. Additionally, I want to thank you for your critical feedback and scientific advice during my thesis advisory committee meetings. In one breath, I also want to thank **Prof. Dr. Karin de Visser** for her active participation and thoughtful comments during the very same meetings. Moreover, I am grateful to **Dr. Josephine Bageritz** and **Prof. Dr. Simon Anders** for taking part in my defense examination.

I want to thank my bioinformatic collaborators Shubhada Kulkarni, Alexey Uvarovskii, and Svetlana Ovchinnikova for helping with analyses and for opening a whole new field of science for me. I am especially thankful to Simon Anders for always being available for discussions and furnishing me with great feedback and food-for-thought that extended far beyond my doctoral studies.

I am very appreciative of the financial support I received from the Helmholtz International Graduate School for Cancer Research and the scientific support I received from the numerous core facilities at the German Cancer Research Center, most notably the Flow Cytometry Core Facility, the Single-Cell Open Lab, the Genomics and Proteomics Core Facility, the Omics IT and Data Management Core Facility, the Laboratory Animal Core Facility and the Light Microscopy Core Facility.

I would like to highlight current and past team members of the laboratory who created a beautiful work environment, helped with major experiments, and always had time for scientific discussions, ears for complaints, and words of encouragement. Thank you to Anja G., Anja R., Ann-Kathrin, Barbara, Ben, Benni, Carleen, Caro, Cata, Claudine, Corinne, Courtney, Daniela, Denise, Dimi, Eva B. and Eva G., Joseph, Katha, Laura M., Laura K., Lorena, Maike, Maria, Martin A., Miki, Niklas, Paula, Petra, Sandra, Silvia, Stephanie G., Stephanie K., Stephanie P. and Tina. I want to give a special thanks to my Asian squad Ashik, Mahak, Guanxiong, and Xiaowen, as well as the gruesome twosome Jingjing

and Donato for many unforgettable moments and Till, who made me realize how challenging, but also how fun and rewarding supervising students can be.

I want to thank all my friends, most notably Erwin, Fabi, Tamás, Seba, and Klym for anchoring me, helping me stay connected to reality, and proving to me that at heart I am still the same moron I used to be 20 years ago.

I cherish my parents for making and shaping me – ahogy Leonardo da Vinci már mondta: "Gondolkozz, ahogy apád tanított! Élj, ahogy anyád tanított!" I love my brothers for being the living proof that blood is thicker than water and for always being my safety net, my grandfather, the smartest and humblest person I have ever met and my biggest scientific inspiration, my remaining grandmother, my aunts and uncles, and my two Kosengs.

I want to express my deepest gratitude to my brother in arms Ki Hong Lee, who is more than just a colleague but became a part of my family. This journey would have been a lot more difficult without you and definitely less fun. You are the stoic Ying to my emotional Yang - thanks for 6 years of service!

Lastly and most importantly, I want to thank my wife. Your contribution to my life is unmeasurable – you bring the best out of me, but also the worst, your presence fulfills me, while your absence drains me. You are the only person who can make me speechless and struggle to find the right words. I will never… ever… not… try to love you.

Table of contents

List of Figures

List of tables

Summary

Metastasis is the fatal hallmark of cancer, although representing a highly inefficient biological process. During metastasis, cancer cells hijack blood vessels and travel via the circulation to colonize distant sites, while closely interacting with endothelial cells (EC) throughout the various steps of dissemination. Albeit the endothelium emerged as a crucial regulator of primary tumor growth, tumor cell (TC) invasion, and metastasis formation, its role in priming metastasizing tumor cell (mTC) fates as the interface of dissemination remains largely elusive. This thesis therefore aimed at i) dissecting mTC-EC interactions in the metastatic niche and ii) identifying and functionally characterizing fate instructing endothelial-derived angiocrine signals.

Due to the rarity of metastasis, a novel experimental strategy to enrich specifically for mTC subpopulations capturing all cell states of the early colonization process was developed. In combination with single-cell RNA-sequencing, a first blueprint of the transcriptional basis of early mTC decisions was generated and the temporal interactome of mTCs with lung ECs was resolved. Upon their arrest at the metastatic site, TCs either started proliferating intravascularly or extravasated and preferably reached a state of quiescence. Homeostatic endothelial-derived angiocrine Wnt factors were found to drive this bifurcation by inducing a mesenchymal-like phenotype instructing mTCs to follow the extravasation-dormancy route. In-depth analyses of the single-cell data revealed that the responsiveness of mTCs towards angiocrine Wnt signaling was not regulated at the receptor-ligand level. Moreover, *in vivo* niche-labeling approaches identified that dormant and proliferative TCs occupied the same vascular niches and that the endothelium elicited a bimodal response toward the tumor challenge. This was marked by focal upregulation of biosynthesis genes and matrix remodeling events in the physical vascular micro-niche of proliferating TCs but not dormant TCs, and the systemic upregulation of immune-regulatory angiocrine factors. Surprisingly, morphologically homogenous TCs displayed unexpected baseline transcriptional heterogeneity in culture, which was established at the epigenetic level and served as the impetus of mTC behavior. Epigenetically plastic cells were marked by high Wnt signaling activity and a mesenchymal-like state, leading them to preferably follow the extravasation-dormancy route. Epigenetically sealed TCs had low activity and proliferated intravascularly. Collectively, the data identified the predetermined methylation status of disseminated TCs as a key regulator of mTC behavior in the metastatic niche. While metastatic niche-derived factors per default instruct the acquisition of quiescence, mTCs unwind a default proliferation program and only deviate from it if epigenetic plasticity renders them responsive toward the microenvironment.

Zusammenfassung

Metastasierung ist der tödlichste Schritt einer Krebserkrankung. Während der Metastasierung infiltrieren Tumorzellen (TZ) Blutgefäße, verbreiten sich über die Blutbahn und kolonisieren fremde Organe, wobei sie mit Gefäß auskleidenden Endothelzellen (EZ) interagieren. Das Endothel selbst hat sich als wichtiger Regulator des Primärtumorwachstums, der Tumorzellinvasion und des metastatischen Auswuchses hervorgetan; seine Rolle als Instruktor des metastatischen Verhaltens metastasierender TZ (mTZ) ist jedoch wenig erforscht. Diese Thesis befasst sich demnach mit i) der Entschlüsselung der mTZ-EZ Interaktionen in der metastatischen Nische und ii) der Identifikation und Charakterisierung instruktiver angiokriner Signale.

Aufgrund der Ineffizienz und der damit verbundenen Seltenheit metastatischer Dissemination, wurde im ersten Schritt dieser Arbeit ein experimentelles Model entwickelt, das die Anreicherung mTZ-Subpopulationen und damit die gesamtheitlich Abbildung des Kolonisierungsprozesses ermöglichte. Mit Hilfe von Einzelzell-RNA-Sequenzierung wurde die transkriptomische Grundlage des frühen mTZ Entscheidungsprozesses, sowie das temporale Interaktom zwischen mTZ und EZ entschlüsselt. Es wurde festgestellt, dass mTZ nach ihrer Ankunft im metastasischen Organ entweder extravasieren und präferiert in einen Ruhezustand fallen oder innerhalb des Blutgefäßes anfangen zu proliferieren. Diese Zweiteilung wurde durch homöostatische angiokrine Wnt Faktoren getrieben, welche einen mesenchymalen Phänotypen in mTZ induzierten, der wiederum Extravasation und zelluläre Quieszenz begünstigte. Bioinformatische Analysen und *in vivo* Markierungstechniken offenbarten, dass dieses Verhalten nicht über differenzielle Rezeptor-Ligand Interaktion reguliert war und dass dormante und proliferierende TZ dieselbe vaskuläre Nische besetzten. Im Gegensatz zu dormanten TZ war die physische vaskuläre Nische proliferierender TZ charakterisiert durch die Expression biosynthetischer Gene, die den Umbau der extrazellulären Matrix bedingten, während das Endothel gesamtheitlich eine immun-regulatorische Funktion aufwies. Überraschenderweise besetzten morphologisch homogene TZ in Kultur verschiedene transkriptomische Zustände, was epigenetisch gesteuert wurde und direkt das metastatische Verhalten von mTZ bestimmte. Epigenetische Plastizität ermöglichte eine hohe Wnt-Grundaktivität and einen mesenchymalen Phänotyp, was wiederum Extravastion und Tumordormanz begünstigte. Epigenetisch beschränkte TZ waren durch niedrige Signalaktivität charakterisiert und proliferierten folglich intraluminal. Zusammengefasst identifiziert die hier präsentierte Arbeit das prädeterminierte Verhalten disseminierter TZ basierend auf ihrem epigenetischen Status. Während Faktoren der vaskulären metastatischen Nische Tumorzellquieszenz fördern, starten TZ ein Proliferationsprogramm und weichen davon nur ab, falls epigenetische Plastizität die Zellen empfänglich für Nischfaktoren macht.

Contributions

The work in this thesis is the result of a highly collaborative effort. The overall study was designed and conceptualized under the guidance of my mentor and Ph.D. supervisor Prof. Hellmut G Augustin. All experiments outlined in this work were planned, performed, and analyzed by me. Additionally, all the plots and experimental figures were generated by me.

I received technical assistance for all *in vivo* experiments from my colleague Ki Hong Lee (justification for shared first authorship on the corresponding manuscript) and other members of the laboratory, most notably Till Rostalski, for large animal experiments. I further received assistance in the analysis and interpretation of sequencing data from my bioinformatic collaborators Alexey Uvarovskii, Svetlana Ovchinnikova, Shubhada R. Kulkarni, and Simon Anders.

Introduction

1.1 Angiodiversity

1.1.1 Macroscopic angiodiversity - form follows function

The main purpose of the endothelium is the transportation of oxygen and nutrients. As such, the vascular system can be viewed as a systemically distributed organ, encompassing all body parts and tissues. In fact, due to the limited diffusion distance of oxygen, nearly all body cells rely in close proximity to the nearest blood vessel. It is no surprise then that the vascular endothelium forms one of the body's largest surfaces with a surface area surpassing 1000 m^2 for a 70kg adult, which translates into roughly 10^{12} endothelial cells (ECs), making ECs one of the most abundant cell populations of the body [1]. Having to fulfill distinct physiological functions, blood vessels show high functional specialization that is reflected by their morphological features (Fig. 1).

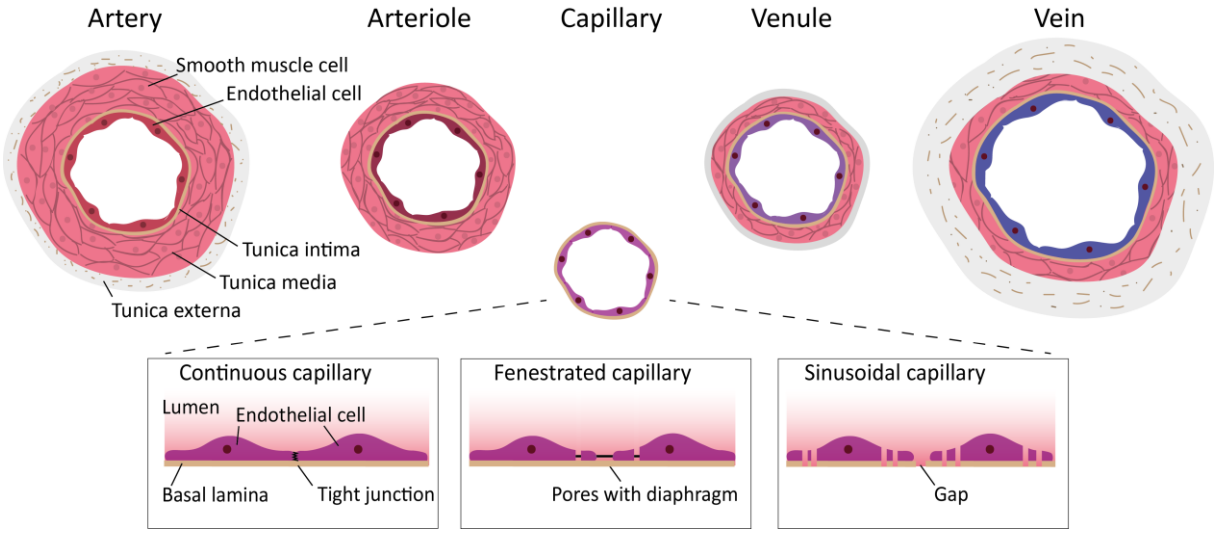

Figure 1: Schematic of morphological angiodiversity. Arteries (except for pulmonary and umbilical arteries) carry oxygenated blood away from the heart and consist of endothelial cell (EC) lining, tunica intima, media, and externa. Arterioles only possess the tunica media and intima but represent the main site of vascular resistance. Capillaries are lined by a single layer of ECs only and show strong organotypicity, which is reflected by three major types of capillaries: continuous, fenestrated, and sinusoidal. Continuous capillaries are the most prevalent and besides having barrier function, permit the diffusion of water, small solutes, and lipid-soluble material. Fenestrated and sinusoidal capillaries have discontinuous EC lining, which enables a high exchange of water and macromolecules. Fenestrated capillaries are present in endocrine organs (e.g. kidney) and are characterized by intracellular pores that are spanned by diaphragms, while sinusoidal endothelia can be found in hematopoietic organs, including bone marrow, spleen and liver and have flattened, irregular shapes and lack basement membranes. Blood from capillaries is ultimately collected in venules and drained into veins. Venules have a tunica externa and media, in contrast to arterioles, however, the media is poorly developed. Veins are characterized by a thick tunica externa and generally a much thinner media compared to arteries.

Arteries, except for the pulmonary and the umbilical artery, supply oxygenated blood away from the heart and, hence, are subjected to high blood pressure and high oxygen. To counterbalance pressure, the arterial wall is built up of three main layers. The tunica externa forms the outermost layer and is composed of collagen fibers and elastic tissue. The tunica media is made up of smooth muscle cells, elastic tissue, and collagen fibers, whereas the innermost layer, the tunica intima, is mainly made up of endothelial cells and is in direct contact with blood. Depending on the composition of the tunica media one can further differentiate elastic arteries that contain high elastic tissue, which enables size and diameter increase in response to high systolic pressure from muscular arteries that have high smooth muscle content. Muscular arteries mainly distribute blood from larger elastic arteries into resistant vessels by maintaining the blood pressure through contraction.

Arteries branch into arterioles, which are directly connected to capillaries. In most cases, arterioles consist of only tunica media and intima and represent the primary site of vascular resistance, facilitating the transition from high-pressure and high-velocity arterial blood flow to lower pressure and flow in the capillaries. Blood from capillary beds is collected by venules and drained to veins. Compared to arterioles, venules possess the tunica externa. Their media, however, is poorly developed so that venules have thinner walls and a larger lumen than arterioles. While blood in the capillary bed is under high pressure and low velocity, which increases the exchange of substances, venule blood flow is of low pressure and high velocity. This leads to a decreased exchange of substances which is further attenuated in the veins. Compared to arteries, veins have thick externa, but generally much thinner media, as veins do not function primarily in a contractile manner. Consequently, the lumen of veins is significantly larger than of arteries, which is why up to 70% of the blood volume is contained within veins and venules (Table 1) [2].

Table 1: Rheological and morphological features of vessel types. Summarizing table of the rheological and biophysical features of distinct blood vessel types, as well as important morphological metrics in humans and mice.

	Artery	Arteriole	Capillary			Venule	Vein
			Continuous	Fenestrated	Sinusoidal		
Pressure	↑ ↑ ↑ ↑	↑ ↑	↑			~	↑↑
Oxygen	↑↑↑	↑↑↑	↑			~	~
Velocity	↑↑↑	↑	~			↑	↑↑
Diameter/ lumen (in µm) human	~ 4000/2000	~ 30/10	~ 8/6			~ 20/16	~ 5000/4000
Diameter/ lumen (in µm) mouse	~ 150/50	~ 18/9	~ 5/4			~ 14/12	~ 250/150
Primary rheological function	Supply of oxygenated blood	Major site of vascular resistance	Demarcation, passive water and solute exchange	Accelerated fluid and solute exchange	Free fluid and solute exchange	Reabsorption of interstitial fluid	Collection of deoxygenated blood

1.1.2 Organotypic capillaries

While arteries, arterioles, veins, and venules show very similar structural organization throughout the body, capillaries display great diversity in their morphology reflecting organotypic specialization. Lined by a single layer of ECs, capillaries can typically be distinguished into three major types: continuous, fenestrated, and sinusoidal. Continuous capillaries are present in any tissue of the body, except epithelia and cartilage, and permit the passive diffusion of water, small solutes, and lipid-soluble materials into the surrounding tissue. Macromolecules and blood cells are retained in the lumen and require specific transportation mechanisms to transmigrate through the endothelial barrier. Fenestrated and sinusoidal capillaries both display discontinuity in their EC lining. While fenestrated capillaries have intracellular pores with a diaphragm, sinusoidal endothelia are characterized by flattened, irregular shapes and deficient coverage by basal lamina (Fig. 1). Pores and gaps lead to accelerated (pores) or even free (gaps) exchange of water and therefore to an enhanced exchange of macromolecules between plasma and interstitial fluid. Unsurprisingly, both types of capillaries are mainly to be found in endocrine organs (secretion of macromolecules), as well as filtration and absorption sites, such as the kidney and liver [3-6].

1.1.3 Microscopic angiodiversity – gradients and specialization

Besides this morphological specialization, angiodiversity extends to the cellular building blocks of blood vessels. Recent technological advances have made it possible to profile the genomic and transcriptomic features of individual cells. This new era of single-cell analyses has yielded unparalleled insights into the cellular diversity of distinct capillary beds [7]. For instance, single-cell

RNA sequencing (scRNA-Seq) has identified that the lung alveolar capillary bed harbors a specialized EC subtype that is defined by a distinct gene expression program and physiological function [8-10]. These aerocytes (aCap) were found to mark the major site of gas exchange and were morphologically characterized by a lack of pericyte coverage and a thin basement membrane. On the other hand, classical continuous endothelial cells (gCap) were identified as the structural vessel component by displaying pericyte coverage and having thick basement membranes. Additionally, gCaps were identified to represent the regenerative endothelial cell pool upon lung injury. Within a single capillary, both EC types are closely intertwined to form a functional vessel [8-10].

Being directly exposed to the circulating blood, ECs sense and immediately respond to changes in physical and biochemical properties. Alongside a vessel, these parameters form gradients, which can direct the endothelial gene expression program. The liver sinusoidal endothelium serves as a prototypic example for such gradual intra-vessel angiodiversity. Here, oxygen-rich blood from the hepatic artery converges with nutrient-rich blood from the portal vein and exits the liver via the central vein, resulting in a strong nutrient and oxygen gradient along the liver sinusoidal capillaries. Recent studies have identified that this gradient is reflected in the transcriptome, proteome, and epiproteome of liver sinusoidal ECs and that the zonated expression pattern is causative for the overall metabolic zonation of the liver [11-16]. These findings put the endothelium at the center of controlling homeostatic liver function, which marked a dramatic shift from the previous prevalent view of ECs as passive bystander cells.

1.2 Vascular control of organ function

1.2.1 The angiocrine endothelium

Instructive functions were first attributed to endothelial cells in the context of endothelial-immune interactions in the 1980s. During this period, it was established that ECs do not only receive and react to immune-derived signals but also actively shape the immune response by secretion of instructive signaling peptides [17]. Building on these findings, Lammert and colleagues provided first evidence of a vascular control of solid tissues. In their work, the endothelium was found to produce decisive signals for pancreatic organogenesis and insulin production [18]. Such perfusion-independent vascular control of organogenesis was also discovered for the central nervous system (CNS) [19] and the liver [20]. Especially the hepatic endothelium was identified as a tightly-controlled signaling hub that is essential for liver regeneration. Upon stimulation, liver ECs were found to release crucial trophogens such as hepatocyte growth factor (HGF), which were sufficient to boost hepatocyte proliferation and which in turn was shown to be fine-tuned by an endothelial-autocrine signaling feedback loop [21-24]. These instructive endothelial-derived paracrine-acting signaling molecules were collectively termed “angiocrine factors” [25] and further characterized as master regulators of

regenerative processes in various other organs [26], including the lung [27-32] and kidney [33-36]. In the liver, Wingless-related integration site (Wnt) factors were identified as imperative angiocrine factors that control liver homeostasis and establish overall hepatic metabolic zonation. Mechanistically, liver sinusoidal ECs near the central vein were found to express angiocrine Wnt2 and Wnt9b, which are essential for establishing a niche of self-renewing Axin2-positive hepatocytes [12, 37-40]. Loss of angiocrine Wnt consequently resulted in perturbed metabolic zonation of the liver and impaired its regenerative capacity [37, 41].

1.2.2 Angiocrine Wnt signaling

The Wnt system itself belongs to the promiscuous signaling pathways that consist of multiple ligands that can engage a multitude of receptors. The first Wnt ligand was simultaneously identified as a developmental gene driving segmentation in *Drosophila melanogaster* and as a proto-oncogene in murine breast cancer [42-47]. The current nomenclature is a fusion of *Wingless*, the original gene identified in Drosophila, and its mammalian homolog *Integration 1* [48]. Over the last four decades, the Wnt signaling pathway has emerged as a key regulator of development across the animal kingdom that is crucial for tissue homeostasis by maintaining adult stem cell pools. As such, Wnt ligands are viewed as prototypical growth factors and mutations in the Wnt signaling pathway are causative of numerous growth-related pathologies including cancer [49]. By now, 15 receptors and co-receptors of seven protein classes have been identified that can be activated by a total of 19 main ligands, as well as Wnt-potentiators such as the *R-spondin* gene family. The pathway can, in its essence, be divided into two main branches; i) a canonical branch, in which activation of the receptor leads to the stabilization of β-Catenin, its translocation to the nucleus, and the transcription of effector genes by acting as a co-transcription factor of the T-cell factor/lymphoid enhancer factor (Tcf/Lef) complex and ii) a non-canonical branch that is mediated either by planar cell polarity (PCP) signaling or by Ca^{2+}-signaling (Figure 2) [50].

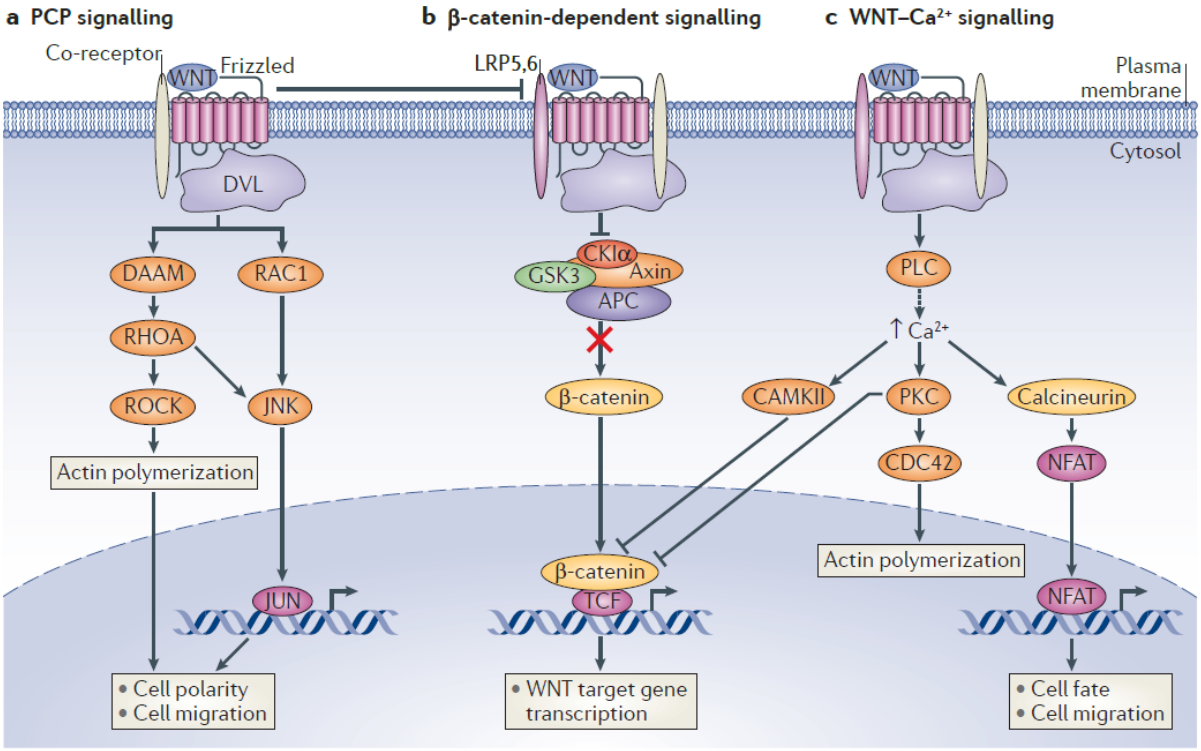

Figure 2: Schematic overview of the main WNT pathways. a) Planar cell polarity (PCP) signaling activates the small GTPases RHOA and RAC1, which leads to activation of RHO kinase (ROCK) and JUN-N-terminal kinase (JNK), respectively. Ultimately, this pathway results in actin polymerization and microtubule stabilization and is predominantly involved in the control of cell polarity and cell motility. **b**) Canonical WNT-signaling is directed by β-catenin. During homeostasis, glycogen synthase kinase 3 (GSK3) phosphorylates β-catenin, which leads to its proteasomal degradation. Upon binding of WNT ligands to the receptor, the β-catenin destruction complex (comprising GSK3, casein kinase Iα (CKIα), Axin, and adenomatosis polyposis coli (APC)) is inactivated, leading to the accumulation of β-catenin and its translocation to the nucleus. Here, β-catenin acts as a co-transcription factor of, among others, T cell factor (TCF) to activate the transcription of target genes. **c**) WNT–Ca2+ signaling leads to activation of Ca2+-and calmodulin-dependent kinase II (CAMKII), protein kinase C (PKC), and calcineurin to promote the expression of genes involved in cell fate and cell migration via nuclear factor of activated T cells (NFAT). Both PCP and Ca2+ pathways can inhibit β-catenin-mediated canonical WNT-signaling and thereby act as negative feedback loops. DAAM, DVL-associated activator of morphogenesis 1; DVL, Dishevelled; LRP, low-density lipoprotein receptor-related protein; MUSK, muscle skeletal receptor Tyr kinase; PLC, phospholipase C; PTK7, protein Tyr kinase 7; ROR, receptor Tyr kinase-like orphan receptor; RYK, receptor Tyr kinase. Adapted with permission from [50].

Wnt ligands are short-range acting signaling molecules that are acylated by porcupine (POCN), and packaged into vesicles for secretion by the Wnt-cargo receptor evenness interrupted (Evi/Wls) [51-53]. While the downstream effector signaling of Wnt is well described, the mechanisms regulating the expression and secretion of Wnt ligands remain rather elusive. In the vascular system, the expression of Wnt ligands follows organotypic Wnt codes, with ECs of distinct organs expressing distinct Wnt ligand repertoires [54]. Recently, our laboratory has identified that the endothelial cell

receptor tyrosine kinase with immunoglobulin like and EGF like domains 1 (Tie1) directly controls the transcription of Wnt2 and Wnt9b in the liver. Acute blockade of the receptor with neutralizing antibodies led to a dramatic downregulation of Wnt-ligand expression in liver ECs that was already visible 30 minutes post-antibody treatment and reached its maximum two hours after administration of the antibody [14]. These findings indicated that the Wnt signaling pathway may act as a signaling rheostat that has high adaptability due to its fast regulation and its organotypicity. However, the functional consequences of organotypic Wnt codes in physiology and more importantly during disease, as well as their developmental establishment, remain unknown. For most organs, the endothelium represents a major source of Wnt ligands. Depleting angiocrine Wnt in the heart was shown to impair cushion remodeling [55], whereas depletion of angiocrine *R-spondin 3* (Rspo3) prevented the formation of pulmonary anti-inflammatory interstitial macrophages in endotoxemic mice [56]. Interestingly, angiocrine Wnt and Rspo3 were found to also act in an autocrine manner, thereby controlling vascular pruning and remodeling during development and tumor angiogenesis [57, 58]. In the bone, arterial EC-derived Wnt was identified to drive the proliferation and engraftment of hematopoietic stem and progenitor cells (HSPCs). Genetic ablation of angiocrine Wnt consequently resulted in lower numbers of HSPCs, which impaired physiological blood formation and, hence, affected the organism at the systems level [59]. However, the hematopoietic vascular niche is not only defined by angiocrine Wnt ligands but harbors synergistically acting angiocrine factors that lead to the establishment of a conducive vascular stem cell niche [60-65].

1.2.3 Vascular control of development and ageing

In recent years, such vascular stem cell niches that harbor adult stem cells were identified in various tissues, including the central nervous system [66-68], skeletal muscle, pancreas, and adipose tissue [69, 70]. Besides its role in tissue maintenance, the endothelium actively governs developmental organ growth, patterning, and morphogenesis [71-77]. Such vascular control of organogenesis can even be modeled *in vitro*. Recent technological advances based on the transient reactivation of the embryonic-restricted ETS variant transcription factor 2 (ETV2) enabled the creation of fully vascularized organ-on-a-chip models that, in turn, allowed to decipher the crosstalk between organotypic endothelial cells and parenchymal cells [78]. One specialized case of a vascular-controlled developmental process is hematopoiesis. Embryonic ECs are highly plastic and, during gastrulation, can give rise to HSPCs. In the first wave of hematopoiesis, cells transit through a molecular state that does not exhibit classical EC characteristics to produce primarily red blood cells and macrophages. Only upon maturation of ECs, during the second wave of hematopoiesis, classical HSPCs are formed directly from hemogenic ECs via the formation of intra-aortic hematopoietic clusters [79-84].

Given the importance of the endothelium in controlling hematopoiesis and organ development, it is no surprise that endothelial dysfunction is a main cause of disease and age-related degeneration. In fact, already in the seventeenth century, the British surgeon Thomas Sydenham coined the axiom that a "man is as old as his arteries" [85]. While the phrase primarily referred to age-related stiffening of arteries, it is now accepted that the aged microcirculation contributes to systemic ageing. In the brain, aged ECs were found to secret a soluble form of the endothelial surface molecule vascular cell adhesion molecule 1 (VCAM1), which directly impaired the blood-brain-barrier and led to cognitive deficits. Transfusing aged blood into young mice was sufficient to induce age-related phenotypes, whereas blockade of soluble VCAM1 rejuvenated aged mice [86]. Similarly, age-dependent reprograming of ECs in the vascular hematopoietic niche was shown to activate platelets and macrophages, which in turn was driving fibrosis and suppressing regeneration [87]. Additionally, age-related reduction of liver EC-derived apolipoprotein M in mice was identified to render lungs and kidneys more susceptible to pro-fibrotic insults [88].

This vascular control of ageing is not only established through systemically-acting angiocrine factors but also by age-related vascular disturbances affecting endocrine organ function. In fact, one of the most prevalent effects of ageing is a general decline in blood vessel density [89-91]. This vascular attrition was found to precede the manifestation of aging hallmarks such as loss of bone mass, which could be restored by specifically increasing organ vessel density [91]. Moreover, loss of endothelial vascular endothelial growth receptor 2 (VEGFR2) was found to cause an early onset of ageing-related phenotypes, demonstrating a direct link between vessel density and organ function [90]. A recent landmark publication expanded this concept by showing that low-dose administration of the vascular endothelial growth factor A (VEGFA) was sufficient to counteract the age-related loss of vessel density and significantly expanded the life- and health span of mice [92]. Grunewald and colleagues identified that the production of VEGF decoy receptors increased with age, which impaired VEGFA signaling by scavenging circulatory VEGFA, thereby driving physiological aging across multiple organ systems. Artificial elevation of circulatory VEGFA directly affected the body composition and ameliorated aging-associated pathologies such as sarcopenia, osteoporosis, hepatic steatosis, age-related inflammation, and tumor incidence [92]. While a moderate systemic angiogenic stimulus was found to limit tumor incidence in aged mice by enabling vessel normalization, localized high concentrations of VEGFA have the exact opposite effect on the vasculature. Indeed, pathological angiogenesis, as best-described during tumor angiogenesis, is characterized by vascular leakage and aberrant vessel formation.

1.2.4 Vascular control of tumor progression

These immature, aberrant vessels are symptomatic for solid tumors and are the main reason for the limited efficacy of anti-angiogenic treatment. Indeed, anti-angiogenic monotherapies failed for most solid cancer types [93]. The underlying idea of an anti-angiogenic treatment was first formulated in 1972 by Judah Folkman [94]. Based on previous work that established the induction of blood vessel growth by neoplastic tissues through secretion of a pro-angiogenic factor [95-97], which was later identified as VEGFA [98], Folkman and colleagues reasoned that by cutting off the blood supply, one would be able to starve tumors and inhibit their growth [94, 99]. While the concept of limiting tumor angiogenesis by treatment with anti-VEGF antibodies showed promising preclinical results [100], it could not be translated into efficacious treatments in the clinic. Rather than inhibiting angiogenesis, anti-angiogenic treatment was found to promote vessel normalization - the mechanisms of which and the discovery of novel druggable targets are subject of current studies [101-104] - which is now exploited in combination therapies to enhance drug bioavailability and efficacy [105, 106]. Combining anti-angiogenic therapy with immunotherapy showed tremendous antitumor activity in a phase 1 clinical trial involving patients with unresectable hepatocellular carcinoma (HCC), making it the new standard of care for the disease [107, 108]. It is of note that current anti-angiogenic treatment strategies mostly rely on the inhibition of VEGF. However, recent work identified VEGF-independent growth and remodeling of blood vessels in models of colorectal carcinoma that was found to be driven by the endothelial peptide Apelin [109]. The discovery of more VEGF-independent angiogenic pathways and combinatorial anti-angiogenic treatment strategies could bring the concept of tumor starvation to fruition.

1.2.5 From local to systemic disease

Primary tumors arise from aberrantly growing tissue cells that were transformed by either gain-of-function (G-O-F) mutations that drive oncogenes, loss-of-function (L-O-F) mutations in tumor-suppressor genes that keep pro-proliferative signals in check or a combination of both [110]. At the macroscopic level, tumors are usually classified by their primary organ site and their histological traits. Carcinomas are epithelium-derived tumors that can be subdivided into adenocarcinomas (glandular epithelium) or squamous cell carcinomas (squamous epithelium). Sarcomas originate from connective and supportive tissue, whereas leukemias are blood-born cancers. Lastly, lymphomas arise from the lymphatic system, while myelomas are plasma cell-derived. For long, primary tumors have been viewed as a locally occurring disease that over time accumulate a certain set of mutations that allow the spread of single tumor cells or tumor cell clusters through the circulation to colonize distant organ sites – a process referred to as metastasis. During metastasis, tumor cells acquire motility through a transdifferentiation process termed epithelial-to-mesenchyme-transition (EMT).

EMT leads to the loss of epithelial characteristics in cancer cells, such as the expression of epithelial cadherin (E-cadherin) and the simultaneous acquisition of mesenchymal traits. This is controlled by a group of EMT-associated transcription factors, including snail family transcriptional repressor 1 (SNAI1), twist family BHLH transcription factor 1 (TWIST1), krüppel like factor 4 (KLF4), and zinc finger E-box binding homeobox 1 (ZEB1) [111]. The mesenchymal phenotype enables TC entry into the circulation, promotes TC survival in the bloodstream, and facilitates TC exit from the vessel for successful colonization [111-114]. Due to the close interactions of the endothelium with the disseminating tumor cell at the various steps of the metastatic cascade (Fig. 3), it is no wonder that the tumor-controlling properties of the vasculature go beyond the initially described hallmark roles of supplying oxygen and nutrients to the primary tumor [115-117].

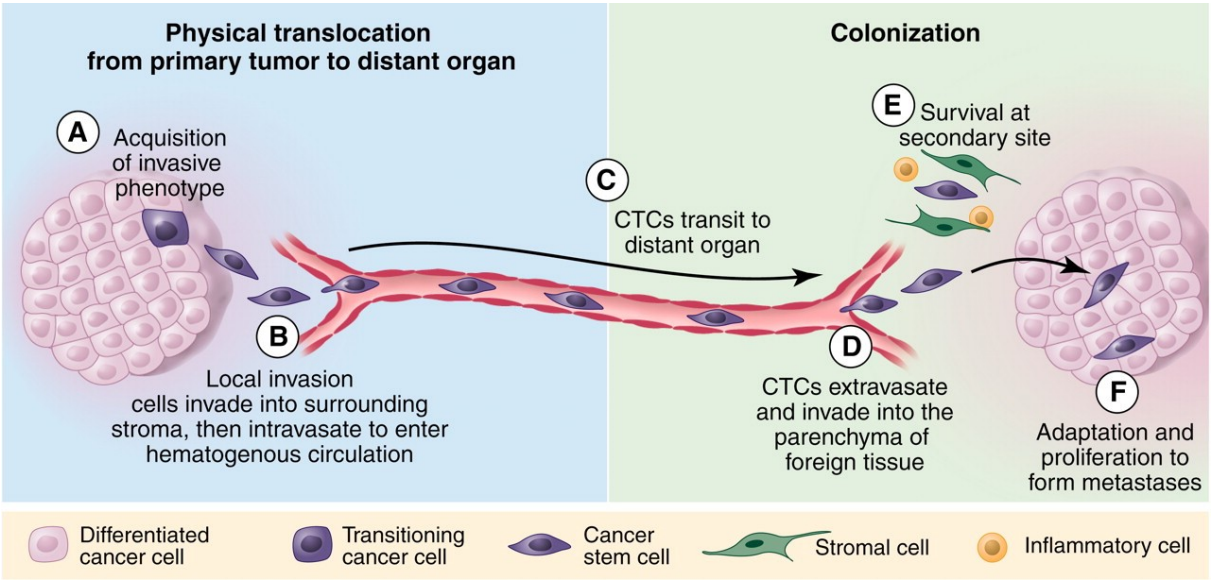

Figure 3: The metastatic cascade. Schematic overview of the metastatic cascade, which can be conceptualized in two main phases i) translocation from the primary tumor and ii) colonization of a distant organ. **A**) TCs acquire an invasive, mesenchymal and stem-like phenotype through EMT. **B**) Invasive stem-like TCs invade the surrounding stroma and intravasate to enter the circulation. **C**) Circulating TCs (CTCs) travel the blood stream to reach distant organ sites. **D**) Upon their arrest, invasive CTCs extravasate from the blood vessel and infiltrate the foreign tissue. Extravasated TCs either remain in a state of **E**) quiescence or **F**) start to proliferate to form metastases. Adapted with permission from [114].

1.3 Vascular control of metastasis

1.3.1 Pre-metastatic niches

Initially hypothesized by Stephen Paget in 1889 as a “seed-soil” mechanism [118], the primary tumor was indeed found to release factors into the circulation that prime distant organ sites for the arrival of metastasizing tumor cells. The establishment of such pre-metastatic niches by tumor-derived exosomes or other primary tumor-derived factors has now been described for most solid cancers

[119-127]. These factors are not only distributed by the endothelium but also affect vascular cells directly. It was shown that the vascular pre-metastatic niche is characterized by remodeling events, such as the accumulation of pericytes, which was directed by angiocrine factors [128, 129]. Moreover, the endothelium, with its vast surface area, was identified as a systemic amplifier of primary tumor-derived signals and thereby contributing directly to the systemic regulation of metastatic disease [129-131]. However, recent work has put the notion that pre-metastatic niche formation is a necessity for metastatic spread at least in question. For breast cancer, metastatic dissemination was identified as an early event during tumor progression with the majority of metastases deriving from tumor lesions that are barely palpable [132-134]. Furthermore, non-malignant tissue cells were shown to be equally capable of colonizing foreign organs and forming metastasis if transformed once disseminated [135]. These findings have great clinical ramifications. After all, metastasis is considered to be the fatal hallmark of cancer and the final frontier in curing the disease [136]. However, taking the early dissemination model into account, it is clear that metastatic tumor cells co-evolve with the primary tumor and, hence, display a distinct mutational status and cellular properties that require different treatment strategies [137, 138]. One popular idea to circumvent metastatic heterogeneity is to develop novel treatment strategies targeting the metastatic niche and not the tumor cell per se [139].

1.3.2 Endothelial control of intravasation, extravasation, and colonization

Given the endothelium's involvement in all steps of the metastatic cascade and its immediate exposure to the blood stream (Fig. 3), it provides an attractive therapeutic target to limit metastasis [140]. Vessel normalization in the primary tumor by anti-angiogenic treatment was found to not only benefit drug penetrance but also limit tumor cell intravasation by reinstating vascular integrity [101-103]. Furthermore, normalizing the inflammatory response of ECs in established metastasis in combination with metronomic chemotherapy proved to be effective to limit metastatic growth [141]. Quenching the inflammatory response in primary tumor ECs by genetic deletion of the main pro-inflammatory transcription factor signal transducer and activator of transcription 3 (STAT3) similarly limited metastasis [142]. In addition, tumor ECs were shown to directly attract tumor cells and actively promote intravasation via the secretion of angiocrine factors [143-146]. Quenching the inflammatory response in endothelial cells may therefore act as a double-edged sword, as the inflammation-induced expression of surface receptors such as endothelial-leukocyte adhesion molecule 1 (E-selectin) not only enhanced tumor cell invasiveness but also facilitated tumor cell arrest and colonization at the metastatic site [142, 147].

The colonization of TCs was found to follow specific patterns, as circulating tumor cells mainly homed to vascular niches that were characterized by active remodeling. This argues for a model, in which

TCs actively shape their vascular niche upon arrest at the metastatic site [129, 130, 148]. Once arrested, TCs need to penetrate the vascular barrier to successfully colonize the organ. Tumor cell-activated platelets were found to contribute to the transendothelial migration of TCs by releasing adenine nucleotides that promote vascular leakiness [149]. Similarly, TCs were identified to directly compromise the vascular barrier by inducing endothelial cell necroptosis, which facilitated extravasation [150-153]. Upon extravasation, TCs were shown to compete with vascular mural cells for space in the perivascular niche and even displayed vascular co-option [154-156]. The mechanic stretching of TCs that accompanied this process was shown to activate the pro-proliferative yes-associated protein (YAP) and transcriptional coactivator with PDZ-binding motif (TAZ) signaling pathway, which induced metastasis formation [157]. However, in the lung, tumor cell extravasation was found to be dispensable for metastatic outgrowth, but to be a pre-requisite of cellular quiescence [158, 159]. Prolonged periods of metastatic tumor cell quiescence are referred to as dormancy, which poses a major hurdle in the combat of metastatic disease by contributing to therapy-resistance and tumor recurrence [160].

1.3.3 Principles of metastatic dormancy

Mechanistically, dormant tumor cells retain the mesenchymal phenotype that enabled them to enter the bloodstream in the first place and acquire additional stem-like properties. Similar to adult stem cells, dormant tumor cells rely in close proximity to blood vessels [139, 160-162]. The peri-vascular niche, which dormant tumor cells occupy, was found to harbor several factors that induce and maintain the dormant phenotype [163]. The cellular source of these factors is promiscuous and different paracrine factors are likely to act synergistically. In the bone marrow, high levels of mesenchymal stem cell-derived TGFβ2 and osteoblast-derived Wnt5a were found to induce dormancy [164-166]. Wnt-signaling was also reported to be crucially involved in dormancy-induction in the lung. However, in the context of lung and breast carcinoma, acquisition of dormancy required autocrine Wnt-inhibition [167], whereas dormancy of metastatic melanoma was dependent on autocrine Wnt-signaling [168]. Melanoma cells were also shown to respond to angiocrine bone morphogenic protein 2 (BMP2) in the lung, which similarly promoted a dormant phenotype [169]. Besides active signaling, the homeostatic biophysical properties of the peri-vascular niche can determine the metastatic phenotype of disseminated tumor cells. High oxidative stress and stiffness of the extracellular matrix were shown to not only keep tumor cell proliferation in check but also to desensitize tumor cells to chemotherapy [170-174]. Conversely, changes in the composition of the extracellular matrix due to inflammation was identified to reactivate dormant tumor cells and enable metastatic outgrowth [175]. Such inflammatory-induced secondary growths can also be observed in the clinics, as breast cancer patients undergoing surgical resection of the primary tumor show a high

incidence of metastatic recurrence 12 to 18 months after surgery. The reawakening of dormant metastatic tumor cells could directly be linked to surgery-induced inflammation [176]. Mechanistically, inflammatory signals were shown to stimulate the activation of EMT-related cellular programs in tumor cells forcing them into cycle [177]. However, immune cells were also found to directly repress metastatic growth through the release of cytokines such as interferon-γ [178]. Interestingly, recent work indicated that the metastatic behavior of disseminated TCs might already be preset in the primary tumor. Areas of high hypoxia or interaction with immune cells in the primary tumor were found to cause phenotypic heterogeneity of TCs, which determined metastatic TC behavior [179-182]. While the endothelium has emerged as a crucial instructor of tumor progression and metastatic colonization, its role during the initial priming of TC fates at the metastatic site remains unknown. Given the endothelium comprises the interface of dissemination and is involved in all steps of the metastatic cascade, it is not far-fetched to hypothesize a similar regulatory function of the endothelium during the acquisition and maintenance of metastatic tumor dormancy.

Aims of the study

Metastatic tumor dormancy poses a major hurdle in the treatment of cancer. While in recent years an increasing number of factors that maintain and drive the dormant phenotype of disseminated tumor cells was identified, the mechanistic basis of how and why certain tumor cells reach a state of quiescence remains virtually unknown. In this thesis, I hypothesized that the behavior of disseminated tumor cells is primed as early as during the initial arrival of circulating tumor cells at the metastatic niche and that the vascular endothelium, as the interface of dissemination, is a crucial fate instructor.

The aims of the thesis are, hence, to i) provide a temporal transcriptional blueprint of tumor-endothelial cell interactions during the initial phases of metastatic colonization *in vivo*, to ii) identify angiocrine factors that serve as instructors of metastatic tumor cell behavior, and to iii) probe their functional consequences in murine metastasis models.

Results

2.1 Probing tumor cell-endothelial cell interactions in the metastatic niche

2.1.1 Enriching rare tumor cell subpopulations by FACS

While metastasis is considered the fatal hallmark of cancer [136], the process of metastatic dissemination itself is highly inefficient [183]. Already modest-sized primary tumors can shed several millions of tumor cells (TCs) into the bloodstream of mice [184], however, only a handful are capable of colonizing distant organ sites and subsequently outgrowing to form metastases. Due to the rarity of this event and given the spontaneous nature of dissemination, probing TC-EC interactions at the metastatic niche requires an experimental model that allows for the enrichment of the interaction, and the synchronization of the cellular events, while enabling high-resolution readouts. To suffice these criteria, I developed a reductionist experimental mouse metastasis model based on intravenous injections of an aggressive syngeneic breast cancer cell line. Wildtype Balb/c mice were injected twice with $1x10^6$ GFP-expressing 4T1 breast cancer cells (4T1-GFP) into the lateral tail vein. To measure the temporal transcriptional changes of metastasizing TCs and interacting ECs, TCs and matching ECs were isolated from the lung at day 1.5 (peak phase of tumor cell extravasation) and day 3.5 (induction of tumor cell proliferation) post-injection using a novel fluorescence-activated cell sorting (FACS) gating strategy. Lung ECs from non-injected mice, as well as leftover non-injected tumor cells, served as baseline controls (Fig. 4a). At day 1.5, TCs were discriminated based on their extravasation status. For this purpose, mice were injected intravenously shortly before euthanasia with fluorescently labeled anti-H-2Kd antibody. This antibody is directed against the haplotype of Balb/c mice and labels all body cells exposed to the bloodstream, including syngeneic 4T1-GFP cells, which creates a self-validating system. Sorting gates were set for each mouse based on the staining intensity of cell types that are (i.e. ECs and immune cells) or are not (i.e. epithelial cells, tissue-resident immune cells) exposed to the blood stream (Fig. 4b, c). At day 3.5, TCs were discriminated by proliferation status. Therefore, 4T1-GFP cells were stained prior to injection with CellTracer dye, which is diluted upon each cell division, and which can be measured by a decreased signal intensity in FACS. TCs with dye retention were considered latent and deemed for dormancy, whereas cells with dye dilution were considered proliferative (Fig. 4b, d).

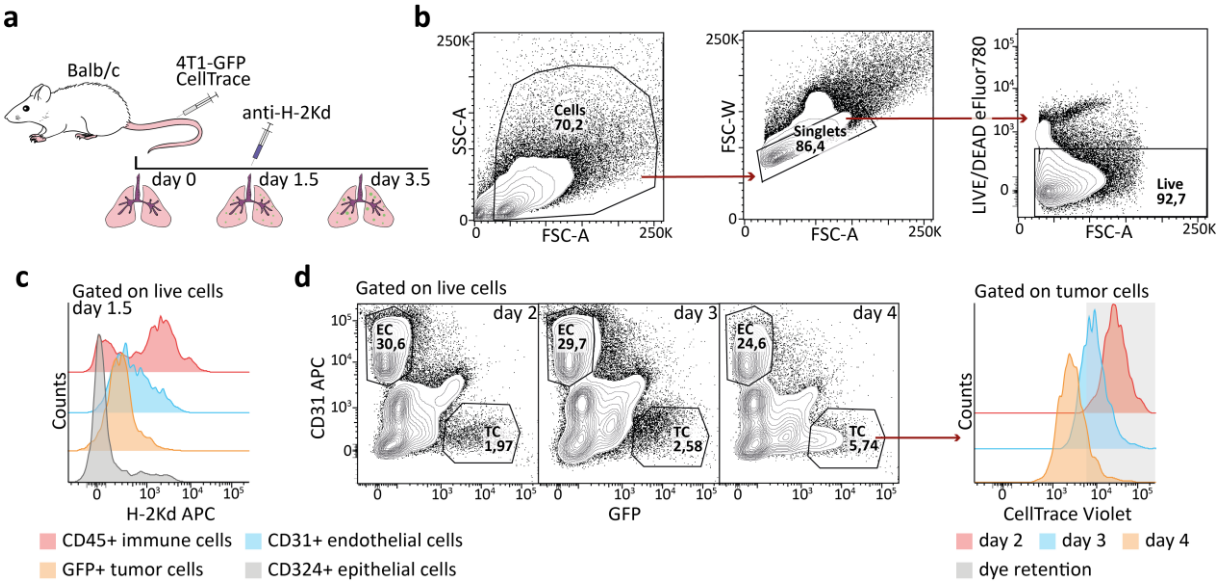

Figure 4: A self-validating FACS strategy to purify rare tumor cell subpopulations. a) Schematic of experimental approach. TCs were labeled with CellTracer dye and wildtype Balb/c mice received two intravenous injections of $1x10^6$ syngeneic 4T1-GFP breast cancer cells into the lateral tail vein. At day 1.5 mice were injected intravenously shortly before euthanasia with anti-H-2Kd antibody. Tumor cells and sample-matched lung endothelial cells were isolated at day 1.5 and day 3.5 post-injection. Lung ECs from non-injected littermates, as well as leftover TCs served as baseline controls. **b**) General gating strategy to purify live, single cells. **c**) H2-Kd *in vivo* staining histograms of isolated cell populations 1.5 days post-injection of 4T1-GFP. Cell types were differentiated based on marker expression. Equal cell numbers per cell type were recorded and staining histograms were overlayed. Note the two peaks for CD45+ immune cells, reflecting circulating immune cells and tissue-resident macrophages that are not exposed to the blood stream. **d**) Temporal tracing of tumor cell proliferation in the lung. TC abundance was assessed in relation to non-proliferative ECs (<1% of dividing ECs 4 days post-injection) as an intra-sample control cell type. TC:EC ratios were stable between day 2 and day 3. The proliferative burst occurred between day 3 and day 4 (left panels). Histogram of CellTracer dye staining intensity in TCs isolated at day 2, day 3, and day 4 post-injection (right panel). Grey background indicates area under the curve of dormant TCs that are characterized by dye retention.

2.1.2 Benchmarking vascular single-cell RNA-seq platforms

To enable single-cell resolution measurements of the temporal transcriptional dynamics of metastatic TCs and ECs, I developed a dedicated lung cell isolation protocol that ensured minimal processing time of the sample (< 1.5 hours from euthanasia to freezing of the sample, see Methods for details), which translates into a minimal introduction of technical artifacts and highest quality of RNA, with typical RNA integrity number (RIN) values >9 (Fig. 5a). For the single-cell RNA-sequencing (scRNAseq), I chose the SMART-Seq2 protocol initially developed by the laboratory of Rickard Sandberg [185]. Here, a template-switching oligo-nucleotide (TSO) is used to generate full-length cDNA, which in turn is used for Tn5 transposase-based library generation (Fig. 5b, c). Given the peculiar features of ECs that have low RNA content (approximately 0.5 pg RNA/EC compared to 4 pg RNA/TC) and are very sensitive towards shear stress imposed by microfluidics devices, I

benchmarked three major single-cell platforms including customized SMART-Seq2 and CEL-Seq2 protocols (both plate-based), as well as the commercially available scRNAseq platform by 10x Genomics (droplet-based). While manual labor and total costs were slightly higher for the SMART-Seq2 protocol compared to CEL-Seq2 and dramatically higher compared to 10x Genomics, the SMART-Seq2 protocol outperformed CEL-Seq2 and 10x Genomics both in depth, as well as the recovery rate (Fig. 5d, e). Here, 10x Genomics especially performed badly with an average recovery of only 23% of the cellular input. This was most likely due to endothelial cell death imposed by high shear stress from cell sorting and additional droplet generation [7].

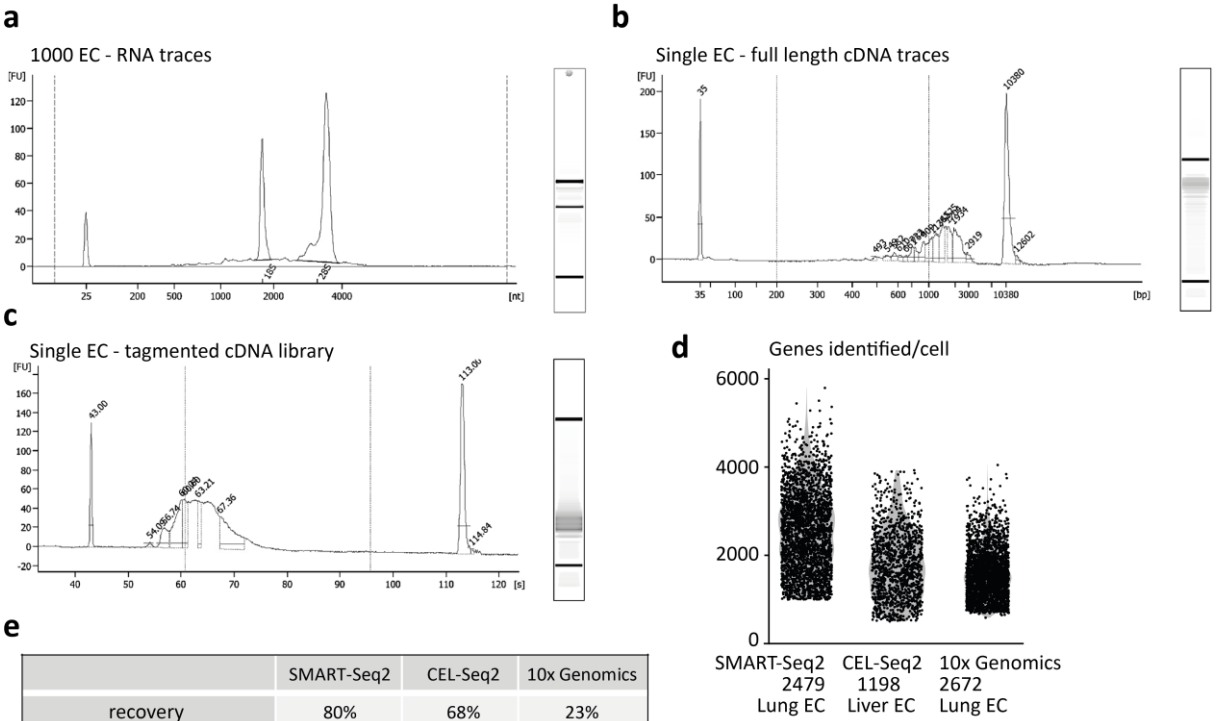

e

	SMART-Seq2	CEL-Seq2	10x Genomics
recovery	80%	68%	23%
real time (5000 cells)	3 weeks	3 weeks	2 days
manual labor	++++	++	+
€ per cell (w/o sequencing)	4	3	0.80
mean genes/cell	~2500	~1790	~1400
UMI	-	✓	✓

Figure 5: Benchmarking vascular single-cell RNA-sequencing platforms. Representative bioanalyzer traces of **a**) RNA isolated from 1000 FACS purified lung ECs of non-injected control lungs with RIN value > 9, **b**) full-length cDNA library of a single FACS purified control lung EC using template switching reverse transcription and subsequent PCR amplification with 23 cycles and **c**) tagmented library of a single control lung EC using the SMART-Seq2 protocol. **d**) Violin plots of genes identified per cell passing quality control using a customized SMART-Seq2 protocol on 2.479 lung ECs (left panel), a customized CEL-Seq2 protocol on 1.198 liver ECs (mid panel), and the commercially available 10x Genomics platform on 2.672 lung ECs. **e**) Summarizing table of performance metrics and key features of the three benchmarked scRNAseq platforms.

2.2 Characterization of metastatic tumor cell fate decisions

2.2.1 Experimental setup

In addition to higher depth and recovery, plate-based scRNA-seq protocols allowed for high flexibility of the study design and the inclusion of biological replicates. Leveraging these advantages, equal portions of matched TC subpopulations (96 cells/mouse and FACS gate) and ECs (384 cells/mouse and timepoint) were sorted from each timepoint, while including at least three biological replicates (Fig. 6a, b). After filtering for high-quality cells (see Methods for specifications), the remaining cells in the dataset showed homogenous distribution for genes identified per cell, normalized and raw gene counts (Fig, 6a, b), and the replicates displayed a seamlessly overlapping embedding in a Uniform Manifold Approximation and Projection (UMAP) (Fig. 6d, e), demonstrating the robustness of the data. Most importantly, the expression of *H2-K1* did not differ between the intravascular and extravascular TC fraction (Fig. 6c), highlighting that differences in H-2Kd antibody staining intensity were due to the TC exclusion from the blood stream and not to lower expression levels of the gene. Although TCs from the different FACS gates showed considerable overlap in the UMAP, substructures enriched for cells coming specifically from the extravascular (day 1.5) or the dormant (day 3.5) gate could be identified, indicating that the gating strategy is suitable for enriching rare TC subpopulations, but does not yield high purity (Fig. 6d).

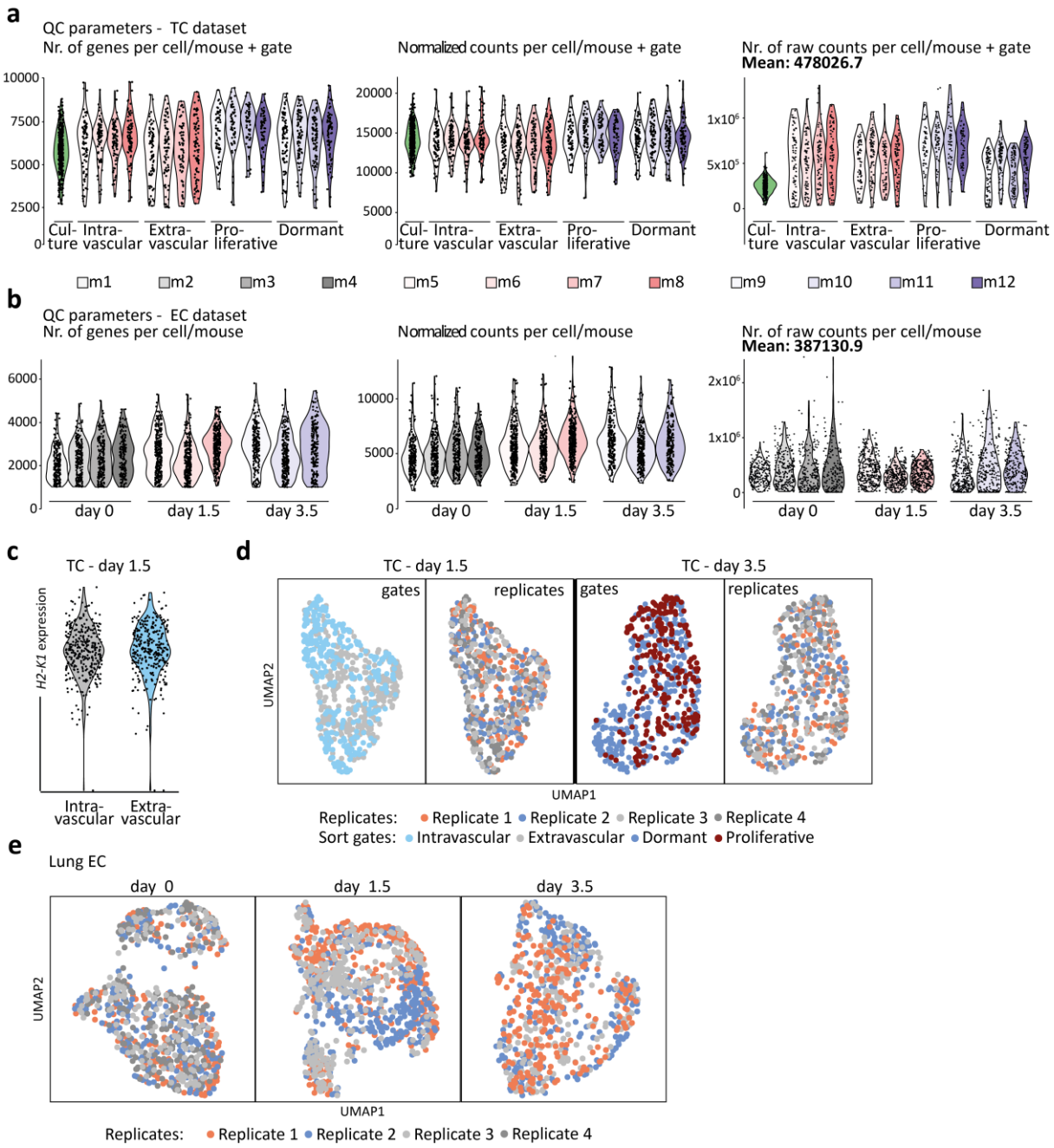

Figure 6: Experimental setup and quality control. a) Number of genes (left panel), normalized gene counts (mid panel) or total gene counts (right panel) for each tumor cell passing quality filtering split by FACS-gate and biological replicate and **b**) for each endothelial cell passing quality filtering. Violins are colored according to biological replicate. **c**) *H2-K1*-expression in individual TCs isolated 1.5 days post-injection split by their respective FACS-gates. **d**) UMAP of TCs extracted from lungs 1.5 days (left panels) or 3.5 days post-injection (right panels). Cells are colored by FACS sort gate (left) or by biological replicate (right), respectively. **e**) UMAP of lung ECs extracted from control lungs (left panel), 1.5 days post-injection (mid panel) or 3.5 days post-injection (right panel). Cell are colored by biological replicate.

2.2.2 The lung endothelium displays a bimodal response towards mTCs

To assess the endothelium's response towards arriving mTCs, ECs of the combined dataset were first classified into the known lung-specific EC subtypes, which were previously reported [8-10] and included ECs of arteriole and venule origin (large vessel EC), general capillary ECs (gCap), aerocytes (aCap) and ECs that are in cell cycle (cycling EC) (Fig. 7a-c). For this purpose, each EC was scored for the expression of the marker gene sets (Fig. 7c, Table 17) and thresholds were set for classifying the endothelial cell type (Fig. 7a, b, d). ECs with large vessel gene scores > 1 were considered large vessel ECs, whereas cycling ECs were defined by a cycle gene score > 0.5. ECs displaying aCap gene score > 0 and gCap gene score < 0 were specified as aerocytes and distinguished from general capillary ECs, which were defined by aCap gene score < 0 and gCap gene score > -0.5 (Fig. 7d). Interestingly, most of the transcriptional dynamics upon tumor challenge was restricted to gCap, ultimately resulting in the emergence of cycling ECs that were of gCap identity (Fig. 7e, f).

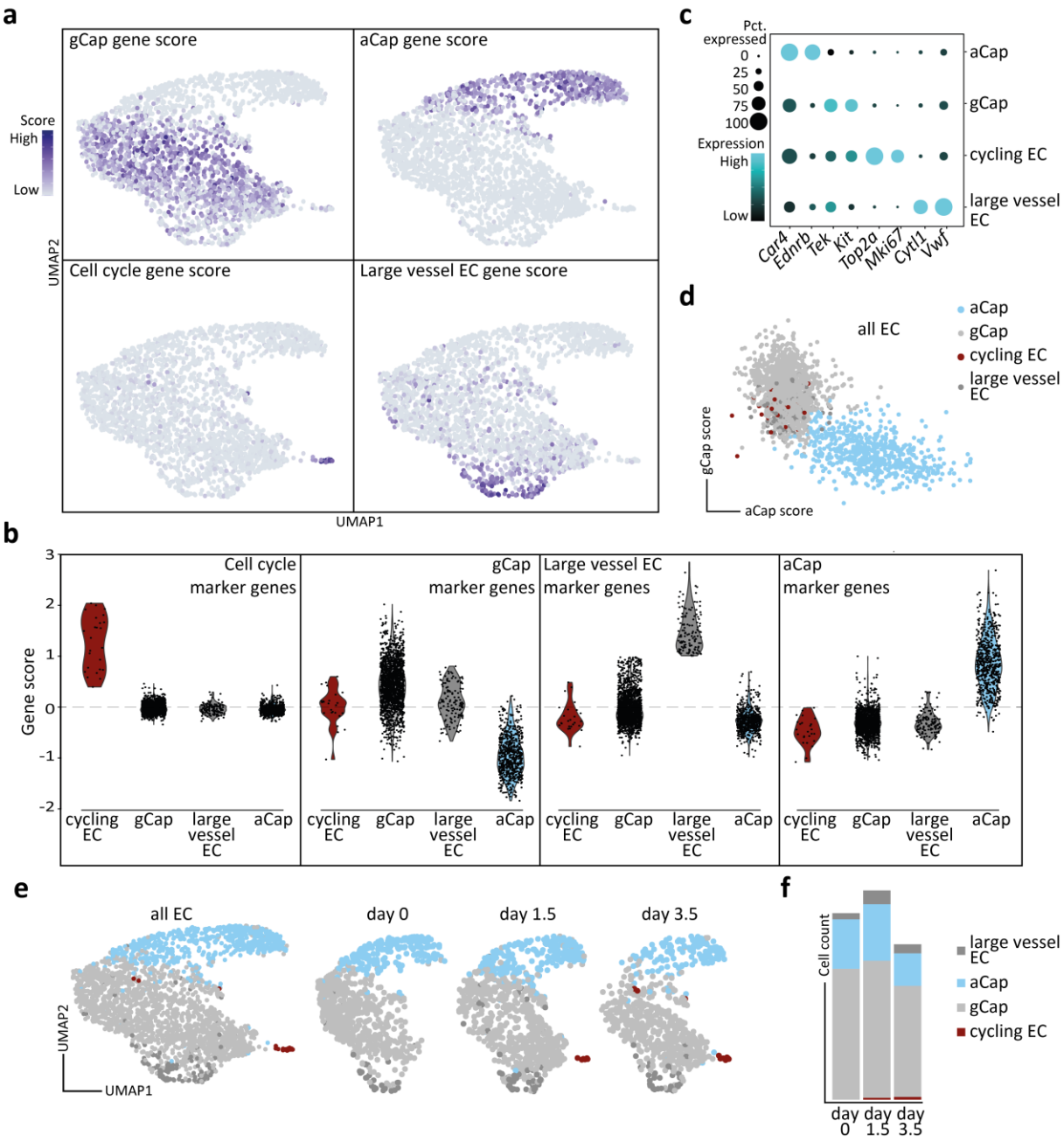

Figure 7: Lung EC scRNAseq captures distinct endothelial subtypes and transcriptional dynamics. **a**) Gene scores of the respective marker gene panels visualized on UMAP of the combined EC dataset. **b**) Violin plot of gene scores of the respective marker gene panels in individual lung ECs split by classified EC subtype. **c**) Dot plot of representative marker gene expression used for classification of the respective EC subtypes split by EC class. **d**) Scatter plot of gCap score vs. aCap score of lung ECs colored by EC class. **e**) UMAP of total lung ECs (left panel) and UMAP split by timepoints (panels to the right). ECs were colored by class identity. **f**) Stacked bar plot of EC class distribution split by timepoint.

To determine the molecular basis of the transcriptional shift observed in gCap, differential gene expression analysis (DGEA) on filtered capillary EC pseudo-bulks using DESeq2 with subsequent gene set enrichment analysis (GSEA) was performed. For this purpose, ECs classified as large vessel ECs were subsetted from the dataset. The remaining cells were then grouped based on biological replicate and timepoint of extraction and expression counts across all cells were summed for each pseudo-bulk sample. Interestingly, capillary EC gene regulation took place in an immediate response pattern, with genes being mostly upregulated at day 1.5 with subsequent reversion to a more homeostatic state at day 3.5 (Fig. 8a, b). These early response genes were mainly involved in immune regulatory and proliferation pathways (Fig. 8c), which was reflected by the focal upregulation of biosynthesis genes (Fig. 8d, e) and the systemic upregulation of endothelial-derived cytokines and chemokines, collectively termed “angiokines” (Fig. 8d, f). While angiokines were upregulated constitutively across all cells including aerocytes in a temporal fashion, the enrichment of biosynthesis gene expression was restricted to a specialized gCap subpopulation (Fig. 8e). This led me to conclude that the lung endothelium acts in a bimodal-manner and serves as a local producer of biomass while exerting important immune regulatory functions at the systems level. A similar concept of the endothelium serving as a systemic amplifier of primary tumor-derived factors has been acknowledged previously [129], whereas ECs isolated from lung metastases showed enrichment for biosynthesis genes [130]. The here presented data expanded and solidified the previous findings and provided first evidence of a systemic and a micro-niche-specific response of the endothelium during the initial phases of metastatic dissemination.

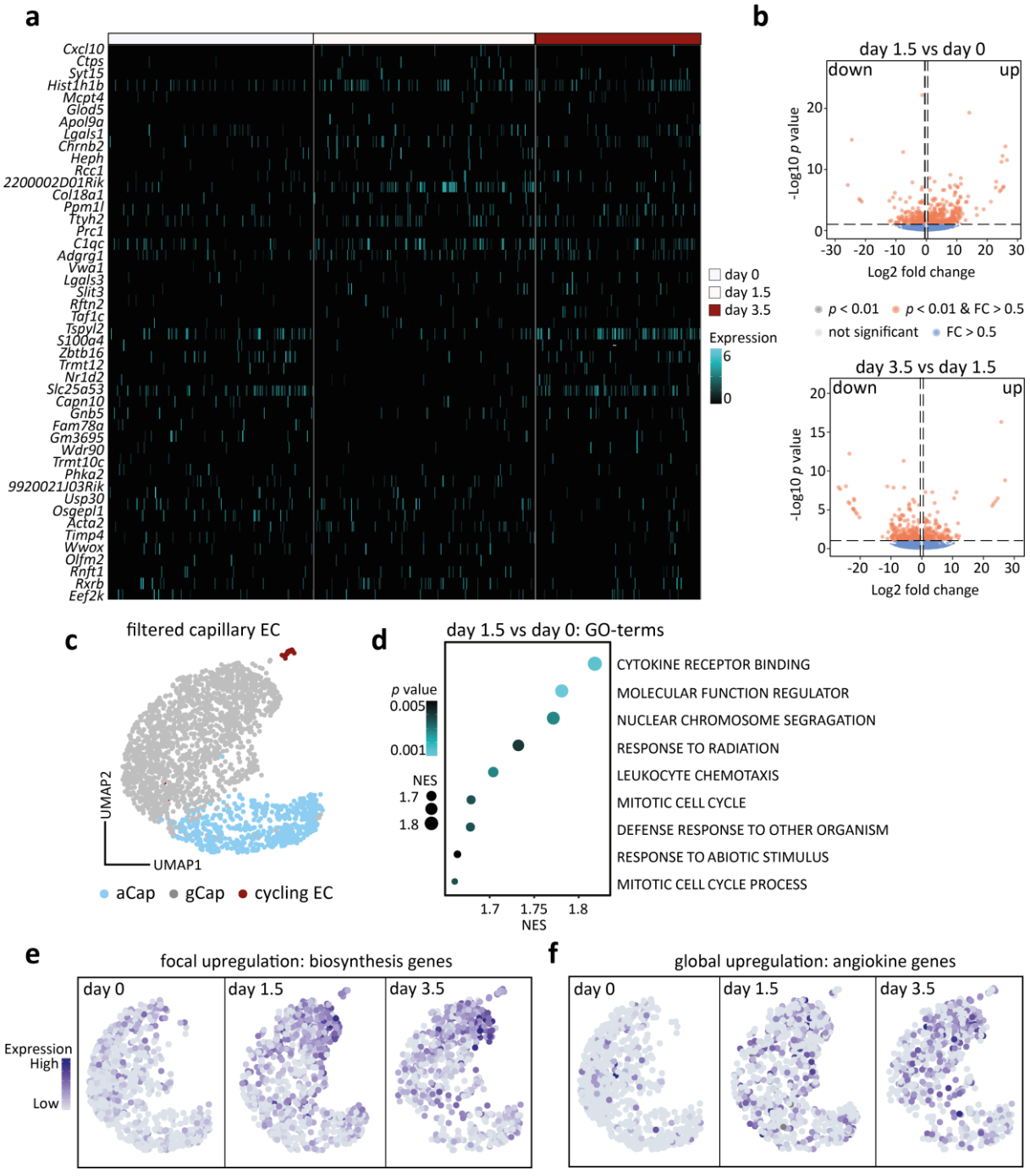

Figure 8: Lung endothelium elicits a bimodal response. a) Heatmap of top 50 regulated genes as identified for differential gene expression analysis across the experimental timeline. **b**) Volcano plots of differentially expressed genes for the day 1.5 versus day 0 comparison (left panel) and day 3.5 versus day 1.5 comparison of total lung EC pseudo-bulks. Fold change and *p* values were computed using DESeq2. FC, Log2 fold change. **c**) UMAP of the filtered capillary EC dataset colored by EC class. **d**) Gene ontology (GO-) terms enriched for genes upregulated in day 1.5 lung ECs compared to baseline control cells. NES, normalized enrichment score. **e**) Visualization of biosynthesis gene expression scores in capillary lung ECs in the UMAP split by timepoint and **f**) of angiokine gene expression scores.

2.2.3 Canonical Wnt-signaling drives tumor cell quiescence

While these findings were conceptually very important, they did not provide answers to how metastatic TCs acquire their fate. I, therefore, pursued a reverse strategy, by comparing the different TC states with each other and deducing fate-instructing angiocrine factors from differentially active signaling pathways and cellular programs in TCs. Clustering analysis of the combined TC dataset identified five clusters that were enriched for cells from the respective FACS gates (Fig. 9a, b). Cultured TCs showed distinct transcriptomic signatures and were therefore excluded from subsequent analyses (Fig. 9a). Trajectory analysis of TCs extracted from the lungs revealed three main branches (Fig. 9c). Setting the cells from the intravascular cluster as the starting point, the branches of trajectory were found to 1) transition directly from intravascular to proliferative cells, 2) transition directly from intravascular cells to a subset of extravascular cells and 3) transition through a subset of extravascular cells to dormant cells. Of note, the pseudo-temporal order of the events reflected the real-time sequence, with proliferative and dormant cell states being established last in pseudotime (Fig. 9d). These data also indicated that induction of proliferation preceded dormancy and that TC extravasation was a pre-requisite of tumor dormancy, but dispensable for TC proliferation, which molecularly defines earlier microscopy-based concepts [158, 159]. Based on these findings, I next compared the proliferative vs. dormant state. To identify bona fide dormant TCs (DTC), each cell from the day 3.5 dataset was scored for the expression of G2M-phase and S-phase specific genes. To exclude cells that have proliferated and dropped out of cycle, only cells that showed dye retention in FACS and had a summed cell cycle gene score of <-1 were selected (Fig. 9e). Cell cycle-associated genes were regressed out and DGEA comparing DTCs and cells with summed cell cycle gene scores of >0 from the proliferative gate was performed using Wilcoxon rank sum test with subsequent GSEA. Confirming previous reports [164, 165], transforming growth factor beta (TGFβ) and epithelial-to-mesenchyme transition (EMT) gene sets were enriched in DTCs. One of the most significantly enriched pathways, however, was beta-Catenin mediated canonical Wnt-signaling (Fig. 9f). This was insofar surprising, as Wnt-ligands are prototypic growth factors [49, 50] and were shown to promote tumor growth in both primary tumors and metastasis [167, 186]. Here, the expression of Wnt-pathway genes was enriched on the extravascular-dormancy branch (Fig. 9g), leading to the hypothesis that niche-derived Wnt-ligands elicit an EMT program that enables tumor cell motility, extravasation, and induction of dormancy.

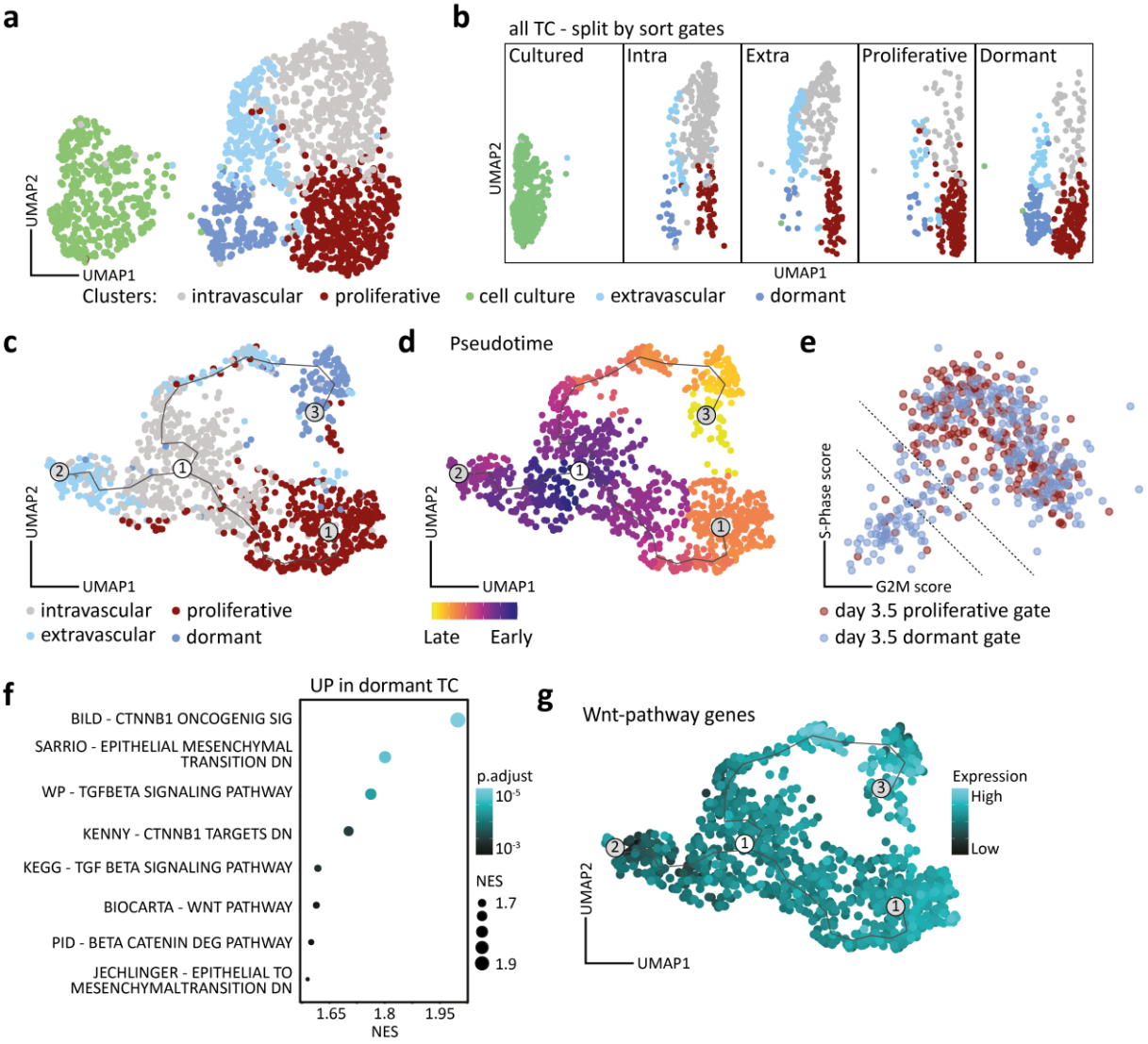

Figure 9: A canonical Wnt-signature defines extravasating-dormant tumor cells. **a**) UMAP visualization of complete TC dataset. Clustering analysis resolves TC transcriptomes into 5 clusters that are enriched for cells of a particular FACS gate. **b**) UMAP of complete TC dataset split by FACS gates. **c**) Trajectory analysis of extracted TCs reveals three transition branches. Cells are colored by cluster identity as resolved in **a**) or **d**) by pseudotime. **e**) Scatter plot of S-Phase and G2M gene expression scores for individual cells extracted on day 3.5 and colored by the respective FACS gate. Dotted lines indicate thresholds of cells with score sums < -1 (lower line) and score sums < 0 (upper line). **f**) Gene set enrichment analysis (GSEA) of genes upregulated in bona fide dormant tumor cells ranked by fold change. NES, normalized enrichment score. **g**) Aggregated expression of 146 genes associated with the canonical Wnt pathway plotted on the trajectory graph from **c**).

2.2.4 Niche-derived angiocrine Wnt ligands are instructors of tumor dormancy

I, therefore, tested the functionality of the Wnt-enrichment in extravasating-dormant TCs in a gain-of-function (G-O-F) and a loss-of-function (L-O-F) experimental approach. For the G-O-F approach, 4T1-GFP cells were treated *in vitro* for two weeks with the canonical Wnt-pathway agonists CHIR-90221 (selective GSK3-inhibitor) or SKL2001 (β-Catenin stabilizer) prior to injection (Fig. 10a).

Conversely, mice were treated daily with the porcupine (POCN) inhibitor LGK974 starting one day prior to injection to create a Wnt-deficient environment (Fig. 10a). As expected, Wnt G-O-F programmed TCs to follow the extravasation-dormancy route, as evidenced by a significantly increased percentage of extravasated TCs 1.5 days post-injection (Fig. 10b, c) and lower metastatic burden and higher incidence of DTCs 3.5 days post-injection, respectively, for both CHIR90221 (Fig. 10d, f) and SKL2001 treatment (Fig. 10g). Contrarily, the L-O-F approach enhanced short-term metastatic outgrowth (Fig. 10d) without affecting extravasation or TC homing capacity (Fig. 10b, e). Intriguingly, the observed short-term phenotypes were found to be stable for up to two weeks, the longest mice could be kept in the experiment as endpoint criteria were reached, even though the treatment with Porcupine inhibitor was stopped at day 4 post-injection (Fig. 10h, i). This clearly pointed towards the initial priming of mTCs by niche-derived Wnt factors that led to the acquisition of a stable, dormant phenotype.

To exclude experimental model specificity, a spontaneous metastasis model in combination with surgical removal of the primary tumor was used to confirm the initial results. For this, 4T1-GFP breast cancer cells were inoculated orthotopically into the mammary fat pad of NOD-SCID mice, which were used to avoid GFP immunogenicity, and primary tumors were grown. Upon reaching a primary tumor size of 100 μm^3, mice were treated daily for five consecutive days with LGK974, and tumors were subsequently resected. To ensure CTC arrival in a Wnt deficient lung niche, mice were treated for an additional two days and left to develop metastases (Fig. 10j). Importantly, LGK974 treatment did not affect primary tumor growth, tumor size at resection or mouse body weight (Fig. 10k-m). However, Wnt-depletion resulted in a significantly increased metastatic burden as evidenced by an increased lung weight/body weight ratio and increased abundance of metastatic TCs in the lung (Fig. 10n-p). Inhibition of autocrine endothelial Wnt-signaling was previously reported to reduce primary tumor vessel density, which in turn could affect metastasis [58]. A similar effect was not observed for the LGK974 treatment, as vehivle control and LGK974 treated tumors did not show differences in vessel area or desmin coverage (Fig. 10q-s). Collectively, these data strongly suggest that metastatic niche-derived Wnt-ligands play a crucial role in the initial priming of tumor cell dormancy.

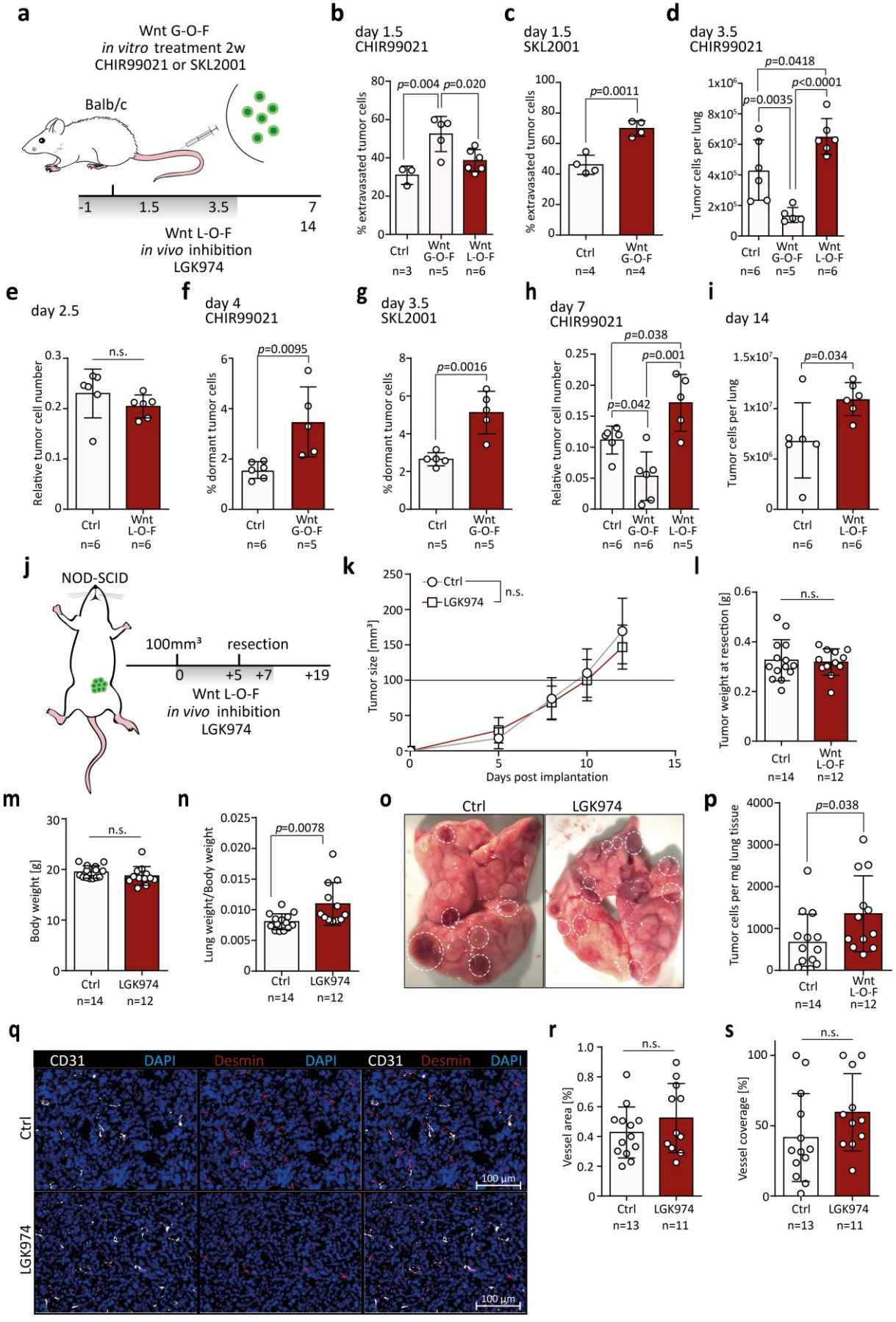
a
Wnt G-O-F
in vitro treatment 2w
CHIR99021 or SKL2001
Balb/c
-1
1.5
3.5
7
14
Wnt L-O-F
in vivo inhibition
LGK974
b
day 1.5
CHIR99021
% extravasated tumor cells
p=0.004 p=0.020
Ctrl n=3
Wnt G-O-F n=5
Wnt L-O-F n=6
c
day 1.5
SKL2001
% extravasated tumor cells
p=0.0011
Ctrl n=4
Wnt G-O-F n=4
d
day 3.5
CHIR99021
Tumor cells per lung
p=0.0418
p<0.0001
p=0.0035
Ctrl n=6
Wnt G-O-F n=5
Wnt L-O-F n=6
e
day 2.5
Relative tumor cell number
n.s.
Ctrl n=6
Wnt L-O-F n=6
f
day 4
CHIR99021
% dormant tumor cells
p=0.0095
Ctrl n=6
Wnt G-O-F n=5
g
day 3.5
SKL2001
% dormant tumor cells
p=0.0016
Ctrl n=5
Wnt G-O-F n=5
h
day 7
CHIR99021
Relative tumor cell number
p=0.038
p=0.001
p=0.042
Ctrl n=6
Wnt G-O-F n=6
Wnt L-O-F n=5
i
day 14
Tumor cells per lung
p=0.034
Ctrl n=6
Wnt L-O-F n=6
j
NOD-SCID
100mm³
resection
0
+5
+7
+19
Wnt L-O-F
in vivo inhibition
LGK974
k
Ctrl
LGK974
n.s.
Tumor size [mm³]
Days post implantation
l
Tumor weight at resection [g]
n.s.
Ctrl n=14
Wnt L-O-F n=12
m
Body weight [g]
n.s.
Ctrl n=14
LGK974 n=12
n
Lung weight/Body weight
p=0.0078
Ctrl n=14
LGK974 n=12
o
Ctrl
LGK974
p
Tumor cells per mg lung tissue
p=0.038
Ctrl n=14
Wnt L-O-F n=12
q
CD31
DAPI
Desmin
DAPI
CD31
Desmin
DAPI
Ctrl
LGK974
100 µm
r
Vessel area [%]
n.s.
Ctrl n=13
LGK974 n=11
s
Vessel coverage [%]
n.s.
Ctrl n=13
LGK974 n=11

Figure 10: Niche-derived Wnt ligands instruct tumor dormancy. a) Schematic of the experimental gain-of-function (G-O-F) and loss-of-function (L-O-F) strategy. Grey bar indicates timespan (in days) of daily treatment with LGK974. **b**) Percentage of extravasated TCs for control treatment, G-O-F (CHIR-99021) or L-O-F approach 1.5 days post-injection. Error bars s.d., *p* values by one-way ANOVA with Tukey post-test are shown. **c**) Percentage of extravasated TCs for control and SKL2001 G-O-F treatment 1.5 days post-injection. Error bars s.d., *p* value by two-tailed t-test. **d**) Quantification of total TC abundance in lungs of mice 3.5 days post-injection of TCs with control, G-O-F (CHIR-99021), or L-O-F treatment. Error bars s.d., *p* values by one-way ANOVA with Tukey post-test are shown. **e**) Percentage of dormant TCs for control and CHIR99021 treatment 4 days post-injection and **f**) for control and SKL2001 treatment 3.5 days post-injection. Error bars s.d., *p* value by two-tailed t-test. **g**) Quantification of relative TC abundance in lungs normalized to total lung EC abundance in mice 7 days post-injection of TCs with control, G-O-F (CHIR-99021) or L-O-F treatment. Error bars s.d., *p* values by one-way ANOVA with Tukey post-test are shown. **h**) Quantification of total TC abundance in lungs of mice 14 days post-injection of TCs with control or L-O-F treatment. Error bars s.d., *p* value by two-tailed t-test. **i**) Fold change in tumor cell abundance in comparison to mean control abundance for LGK974 treated mice 2.5 days, 4 days, 1 week, and 2 weeks post-injection of 4T1-GFP cells. Error bars s.d., *p* values were calculated by one-way ANOVA with Tukey post-test. **j**) Schematic of the experiment. $1x10^6$ 4T1-GFP cells were implanted into the mammary fat pad of NOD-SCID mice. Once tumors reached a size of $100mm^3$, mice were treated with LGK974 for five days until tumor-resection. After tumor resection, mice were treated for an additional two days and left to develop metastases. Grey bar indicates timespan (in days) of daily treatment with LGK974. **k**) Primary tumor growth curves for vehicle control and LGK974 treated mice. n = 14 for control group, n = 12 for LGK974 treatment group. Error bars s.d., *p* values for each measurement timepoint were calculated by two-tailed t-test. n.s., not significant. **l**) Tumor weight at resection and **m**) mouse body weights at the experimental endpoint. Error bars s.d., *p* values were calculated by two-tailed t-test. n.s., not significant. **n**) Lung weight to body weight ratio of mice at the experimental endpoint. Error bars s.d., *p* value by two-tailed t-test. **o**) Representative images of metastatic lungs of mice treated with vehicle control (upper panel) or LGK974 at the experimental endpoint. Dotted white circles indicate metastatic nodules. **p**) Quantification of absolute TC abundance per mg lung tissue in control and LGK974 treated mice at the experimental endpoint. Error bars s.d., *p* value by two-tailed t-test. **q**) Representative images of primary tumor vasculature for control (upper panels) and LGK974 treated mice (lower panels). **r**) Corresponding quantifications of total vessel area per region of interest and **s**) desmin coverage of CD31+ vessels. Error bars s.d., *p* values were calculated by two-tailed t-test. n.s., not significant.

2.2.5 The lung endothelium is a major source of dormancy-instructing Wnt ligands

As Wnt-ligands are short-range acting signaling molecules and tumor cells are closely associated with endothelial cells during the initial steps of metastatic colonization, I hypothesized that the lung endothelium might comprise the major source of dormancy-inducing Wnt ligands. Indeed, lung ECs robustly expressed several Wnt ligands across the experimental timeline (Fig. 11a-c), with *Wnt4* showing the highest expression level. Yet, surprisingly, the overall Wnt ligand expression, as well as the expression of individual Wnt ligands remained constant and was not induced upon tumor challenge. This was true for the total lung endothelium, but also the specific lung EC subtypes (Fig. 11b, d-f). Nevertheless, depleting Wnt ligands specifically from the vascular niche by EC-specific knockout of *Evi/Wls* (Fig. 11f, g) led to a significantly increased metastatic burden in experimental

metastasis models. This was true for syngeneic B16F10 melanoma and E0771-GFP breast cancer cell lines, respectively, as evidenced by an increase in macro-metastatic nodules (B16F10 model) or higher total TC abundance in the lung (E0771 model) (Fig. 11h, i), thereby closely mimicking the systemic pharmacological inhibition. Altogether, these data demonstrated that the lung endothelium is a major source of dormancy-inducing Wnt-ligands.

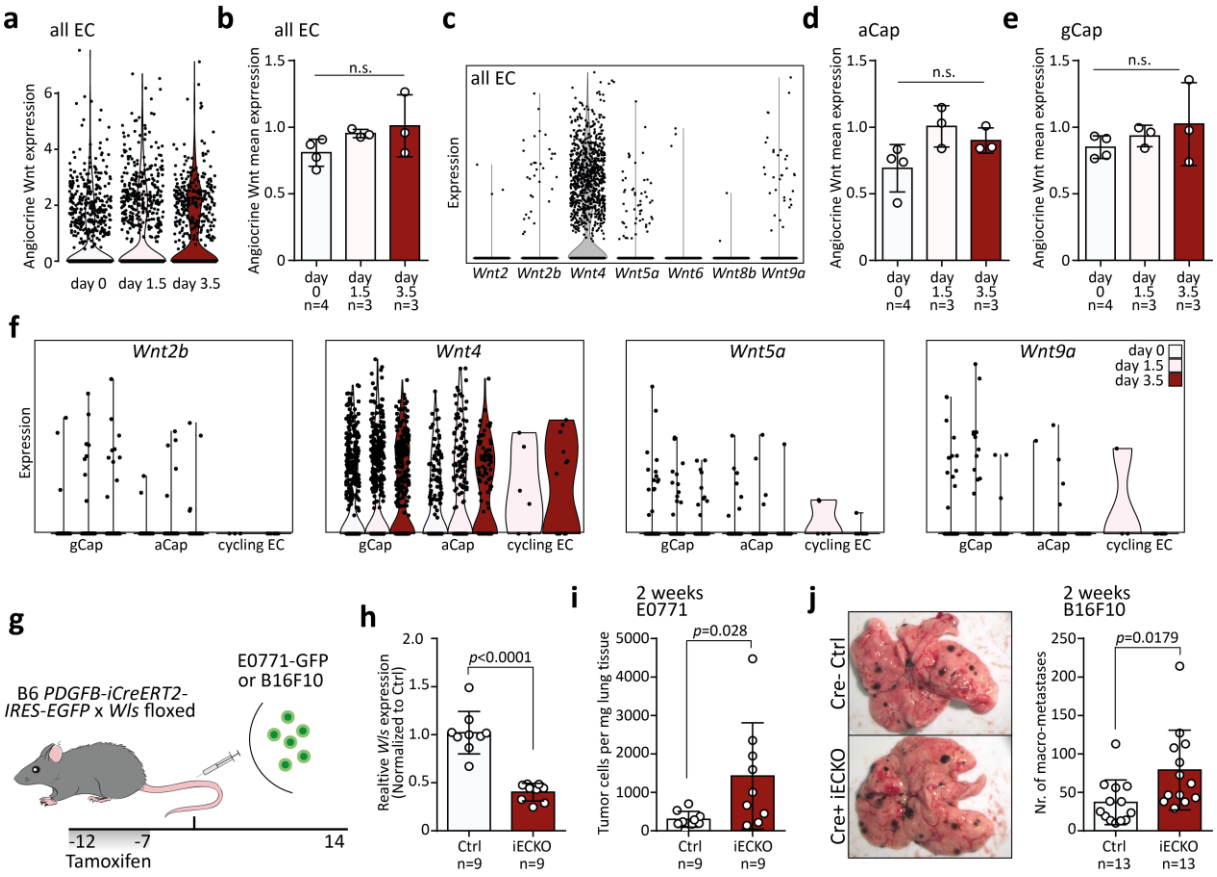

Figure 11: Lung endothelium is a major source of dormancy-instructing Wnt ligands. a) Violin plot of summed Wnt ligand expression in individual lung ECs split by timepoint. **b**) Mean summed expression of Wnt ligands for total lung endothelium pseudo-bulks grouped according to biological replicate and timepoint. Error bars s.d., *p* values were calculated by one-way ANOVA with Tukey post-test. n.s., not significant. **c**) Expression profile for detected Wnt ligands in individual lung ECs of the combined scRNAseq dataset. **d**) Mean summed expression of Wnt-ligands in filtered aCap and **e**) filtered gCap pseudo-bulks of biological replicates grouped by timepoint. Error bars s.d., *p* values were calculated by one-way ANOVA with Turkey post-test. n.s., not significant. **f**) Violin plots depicting the expression level of individual Wnt ligands in capillary lung ECs split by timepoint and EC class. **g**) Schematic of experiment. Gene recombination was induced by tamoxifen administration. $2x10^5$ E0771-GFP or B16F10 cells were injected into the tail vein of EC-specific knockout (iECKO) and control animals. Grey bar indicates timespan (in days) of daily tamoxifen treatment. **h**) Recombination efficiency of *Wls*-iECKO mice. Expression of *Wls* was normalized to *Actb* and fold changes were calculated using the $2^{-\Delta\Delta Ct}$-method. Error bars s.d., *p* value by two-tailed t-test is shown. **i**) Quantification of absolute TC abundance per mg lung tissue in control and iECKO mice at the experimental endpoint. Error bars s.d., *p* value by two-tailed t-test. **j**) Representative images of metastatic lungs from Cre- control (upper image) and Cre+ iECKO mice (lower image) two weeks post-injection of $2x10^5$ B16F10 melanoma cells (left panel) and corresponding quantification of visible metastatic foci per lung (right panel). Error bars s.d., *p* value by two-tailed t-test is shown.

2.2.6 Dormancy is not regulated at the receptor-ligand level or by niche occupancy

As angiocrine Wnt-ligands were not found to be differentially expressed between timepoints and EC subtypes, but clearly exerted crucial dormancy-inducing function, I reasoned that the observed differential TC behavior may result from distinct receptor repertoires between the distinct TC states. To test this, TC pseudo-bulks were formed by grouping cells reflecting the biological replicates and FACS gates. DGEA was performed using DESeq2 and differentially expressed genes (DEGs) of the intravascular versus extravascular and proliferative versus dormant comparison were mapped to CellPhoneDB database [187]. This yielded a list of putative TC-derived ligands (Fig. 12a) and differentially expressed receptors. The receptor list was further filtered for matched EC-derived ligands that were differentially expressed compared to the homeostatic day 0 baseline. TC receptors that were enriched for both comparisons were considered trajectory-defining (Fig. 12b). Surprisingly, the analysis did not reveal components of the Wnt-signaling pathway. I assumed that this might be explained by the constant expression level of endothelial Wnt-ligands and repeated the analysis in a supervised manner and tested only for known Wnt-receptors expressed in TCs. This approach identified five (co-)receptors that were differentially expressed in either the intravascular versus extravascular or the proliferative versus dormant comparison, but not for both comparisons (Fig. 12c). Moreover, the expression of the identified receptors was not enriched for the intravascular-proliferative or the extravasation-dormancy branch of the trajectory (Fig. 12d), suggesting that observed differential Wnt-signaling activity was not regulated at the receptor-ligand level.

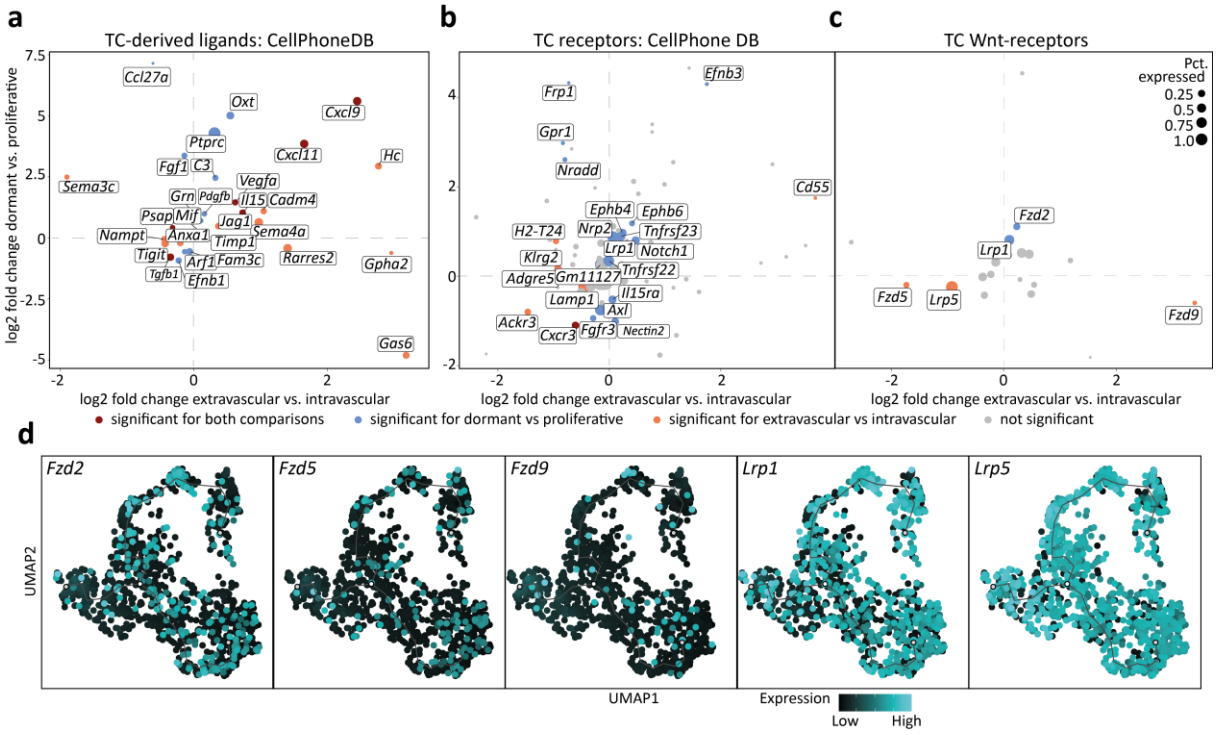

Figure 12: Resolving the Wnt-interactome of endothelial and tumor cells. a-**c**) DGEA of TC pseudo-bulks comparing extravascular versus intravascular and dormant versus proliferative fractions was performed. Differentially expressed genes were mapped against CellPhoneDB and filtered for genes that had predicted and regulated interaction partners expressed in the lung EC scRNAseq dataset. **a**) Putative differentially expressed TC-derived ligands. **b**) Putative differentially expressed TC-receptors as identified by CellPhoneDB. **c**) Supervised analysis of Wnt-receptors expressed in TCs. Log2 fold changes and *p* values were computed using DESeq2. DEG with adjusted p-values < 0.05 were considered significant. Dot size represents percentage of cells with detectable gene expression in the scRNAseq dataset. **d**) Expression pattern of differentially expressed Wnt-receptors on the trajectory graph.

The lung endothelium harbors two distinct vascular beds with presumably less penetrable pericyte-covered gCaps that contain thick basement membranes and more permissive uncovered aCaps without basement membranes (Fig. 13a). Taking the unique anatomical features of the lung vasculature into consideration, TC fates might be driven by distinct niche occupancy rather than by active niche-derived signaling cues. In this scenario, TCs that arrest at permissive aCaps would penetrate the endothelium, extravasate, and reach dormancy, whereas TCs in contact with gCaps would not be able to penetrate the endothelial barrier and either start proliferating intraluminally or be cleared. To probe for the anatomical position of proliferative and dormant TC vascular micro-niches in the lung, an *in vivo* niche-labeling system that allows for the labeling of tissue cells that are in the immediate vicinity of a donor cell [188] was employed. In this system, the donor cells release a lipid-soluble mCherry (tatCherry) that penetrates the cell membrane and is retained upon cell entry. Interacting niche cells can thereby be discriminated by mCherry-positivity. As 4T1-GFP are highly

efficient metastasizers with only a small fraction of cells reaching dormancy (approximately 3-4% dormant TCs at day 3.5), the bulk metastatic micro-niche of this cell line was considered proliferative. To model the dormant niche, the quiescent D2.0R-GFP breast cancer cell line was used, which homes efficiently to the lung, extravasates, but does not form metastases. Both cell lines were transduced to stably express the niche-labeling tatCherry construct and injected into the tail vein of mice. Labeled niche ECs as well as matched unlabeled EC counterparts were purified using FACS and subjected to bulk RNAseq (Fig. 13b, c). PBS- and LPS-injected controls were included to account for injection-related inflammatory responses. Intriguingly, micro-niche-derived ECs were found to explain most of the variance in a principal component analysis (PCA) of the combined samples. While total unlabeled lung ECs extracted from 4T1-injected lungs also separated from the control samples, total lung ECs from D2.0R-injected lungs clustered together with the controls. These data indicated that TCs actively reprogram their micro-niche, while only proliferative TCs provoked pronounced systemic vascular changes (Fig. 13 c). Next, the temporal expression profile of the marker gene sets used for aCap and gCap classification was examined. Selected marker genes showed high specificity and stable and robust expression across the experimental timeline for the EC scRNAseq dataset (Fig. 13d). The marker gene panel was then used to deconvolute the bulk RNA-seq samples and to estimate the abundance of aCap and gCap in the bulk samples compared to PBS control-injected mice (Fig. 13e). While a general bias towards the aCap signature was observed for all tumor-bearing samples, no differences between samples of the dormant and proliferative niche or their matched unlabeled counterparts were detected. This led to the conclusion that dormant TCs and proliferative TCs occupy the same anatomical vascular niches in the lung.

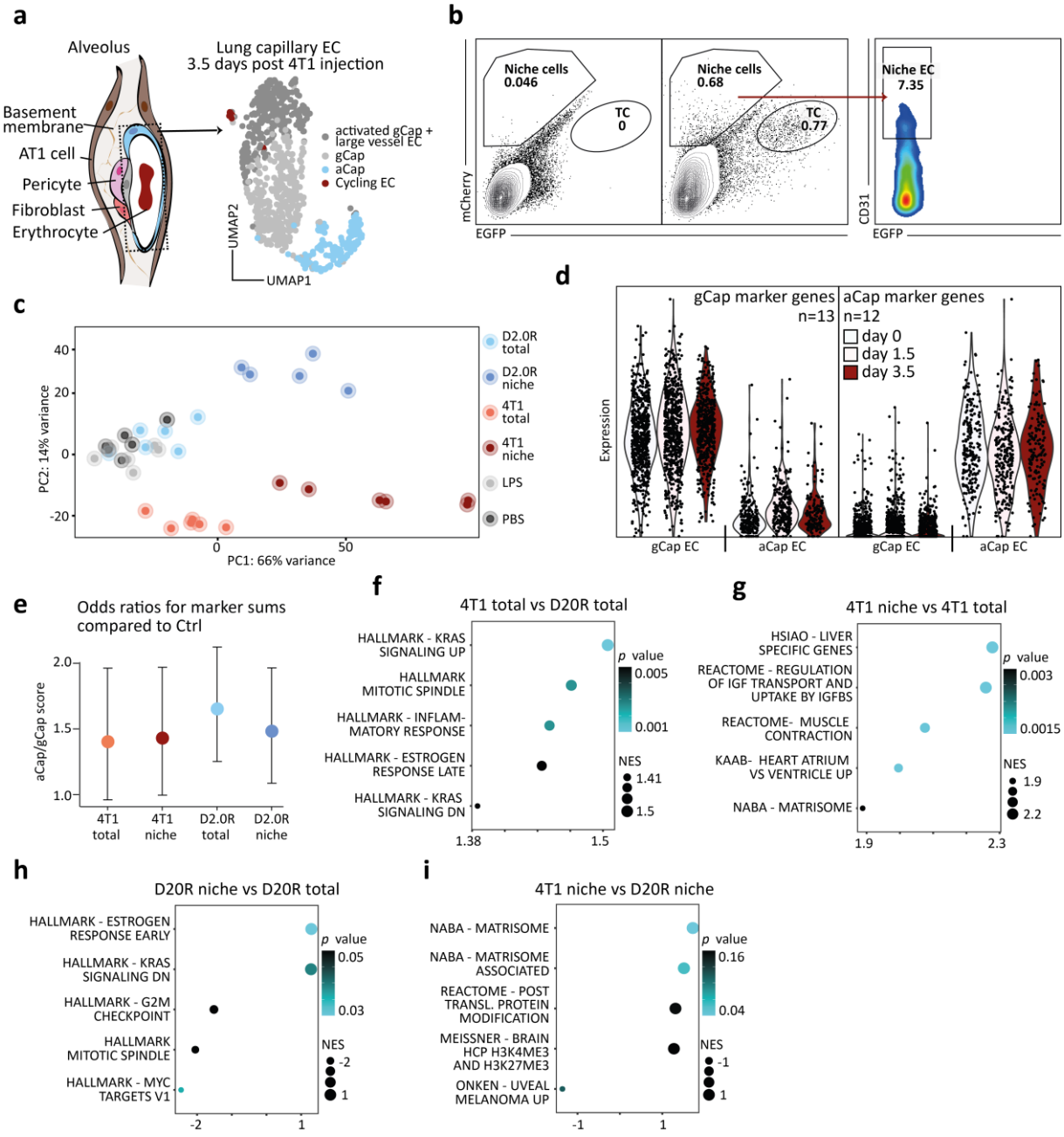
a
Alveolus
Lung capillary EC
3.5 days post 4T1 injection
Basement membrane
AT1 cell
Pericyte
Fibroblast
Erythrocyte
activated gCap + large vessel EC
gCap
aCap
Cycling EC
UMAP2
UMAP1
b
Niche cells 0.046
TC 0
Niche cells 0.68
TC 0.77
Niche EC 7.35
mCherry
EGFP
CD31
EGFP
c
PC2: 14% variance
PC1: 66% variance
D2.0R total
D2.0R niche
4T1 total
4T1 niche
LPS
PBS
d
gCap marker genes n=13
aCap marker genes n=12
day 0
day 1.5
day 3.5
Expression
gCap EC
aCap EC
gCap EC
aCap EC
e
Odds ratios for marker sums compared to Ctrl
aCap/gCap score
4T1 total
4T1 niche
D2.0R total
D2.0R niche
f
4T1 total vs D20R total
HALLMARK - KRAS SIGNALING UP
HALLMARK MITOTIC SPINDLE
HALLMARK - INFLAM-MATORY RESPONSE
HALLMARK - ESTROGEN RESPONSE LATE
HALLMARK - KRAS SIGNALING DN
p value
0.005
0.001
NES
1.41
1.5
g
4T1 niche vs 4T1 total
HSIAO - LIVER SPECIFIC GENES
REACTOME - REGULATION OF IGF TRANSPORT AND UPTAKE BY IGFBS
REACTOME- MUSCLE CONTRACTION
KAAB- HEART ATRIUM VS VENTRICLE UP
NABA - MATRISOME
p value
0.003
0.0015
NES
1.9
2.2
h
D20R niche vs D20R total
HALLMARK - ESTROGEN RESPONSE EARLY
HALLMARK - KRAS SIGNALING DN
HALLMARK - G2M CHECKPOINT
HALLMARK MITOTIC SPINDLE
HALLMARK - MYC TARGETS V1
p value
0.05
0.03
NES
-2
1
i
4T1 niche vs D20R niche
NABA - MATRISOME
NABA - MATRISOME ASSOCIATED
REACTOME - POST TRANSL. PROTEIN MODIFICATION
MEISSNER - BRAIN HCP H3K4ME3 AND H3K27ME3
ONKEN - UVEAL MELANOMA UP
p value
0.16
0.04
NES
-1
1

Figure 13: Dormant and proliferative tumor cells occupy the same vascular niche. a) Schematic of lung alveolus (left panel). Dotted box highlights intertwined aerocytes and general capillary cells. UMAP of EC transcriptomes reflecting the composition of bulk EC samples 3.5 days post-injection of 4T1-GFP cells. Aerocytes form a transcriptomically distinct cellular entity. **b**) Representative FACS plots of total lung cells of PBS-injected control mice (left panel) and niche-labeling 4T1-GFP cells (right panel). Niche cells were discriminated by mCherry-positivity. Niche ECs were purified from total mCherry+ niche cells by expression of CD31 (right panel). **c**) Principal component analysis of transcriptomes from samples included in the experiment. Samples labeled as "total" refer to unlabeled CD31+ ECs; samples labeled "niche" to mCherry+ ECs, dormant samples refer to injections of niche-labeling D2.0R-GFP; proliferative samples refer to injections of niche-labeling 4T1-GFP; LPS controls were injected intraperitoneally with LPS 24 hours prior to euthanasia; PBS controls were injected intravenously with PBS 3.5 days prior to euthanasia. **d**) Summed expression of gCap and aCap marker genes in individual ECs split by timepoints and by EC identity. **e**) Log2 fold changes of aCap marker genes to gCap marker genes odds ratios normalized to PBS-injected control samples. Error bars indicate 95% confidence interval. **f-i**) GSEA of upregulated genes. NES, normalized enrichment score. **f**) Gene sets enriched in unlabeled total ECs from 4T1-injected lungs compared to unlabeled total ECs from D2.0R-injected lungs. **g**) Gene sets enriched in labeled ECs from 4T1-injected lungs compared to matched unlabeled total ECs. **h**) Gene sets enriched in labeled ECs from D2.0R-injected lungs compared to matched unlabeled total ECs. **i**) Gene sets enriched in labeled ECs from 4T1-injected lungs compared to labeled ECs from D2.0R-injected lungs.

Interestingly, ECs extracted from the proliferative niche showed strong enrichment for genes related to extracellular matrix (ECM) production and metabolic activation with induction of proliferation. While proliferative TCs induced a systemic proliferative and inflammatory response, their physical vascular niche was defined by matrix-remodeling processes (Fig. 13f-i). This was in line with the scRNAseq data, which identified focal induction of biosynthesis genes and global upregulation of angiokines (Fig. 8e, f). I next aimed to deduce a marker gene panel to specifically predict ECs that are in physical interaction with proliferative TCs. To achieve that, all bulk conditions were tested against each other, including PBS and LPS injected controls to exclude general inflammatory response genes, and only genes that were specifically upregulated in the proliferative niche sample were selected (Fig. 14a). The resulting gene panel was used to predict tumor-interacting ECs in the scRNAseq data (ECs with gene score > 0.5). Predicted tumor-interacting ECs were specific to the day 1.5 and day 3.5 datasets and showed temporal enrichment reflecting tumor cell proliferation (Fig. 14b, d). To test the generality of the gene panel, a publicly available scRNAseq dataset was utilized [189] and a similar enrichment of the gene set was found specifically for primary lung tumor ECs compared to non-tumorous matched samples (Fig. 14c). Intriguingly, predicted tumor-interacting ECs co-localized with the previously identified biosynthetic ECs in the UMAP of the combined EC scRNAseq dataset and both gene scores showed a significant positive correlation (Fig. 14e, f). This confirmed the hypothesis that the endothelium elicited a bimodal response towards the arrival of metastatic tumor cells that included systemic immunomodulatory function through angiokine expression and biomass production in the physical micro-niche.

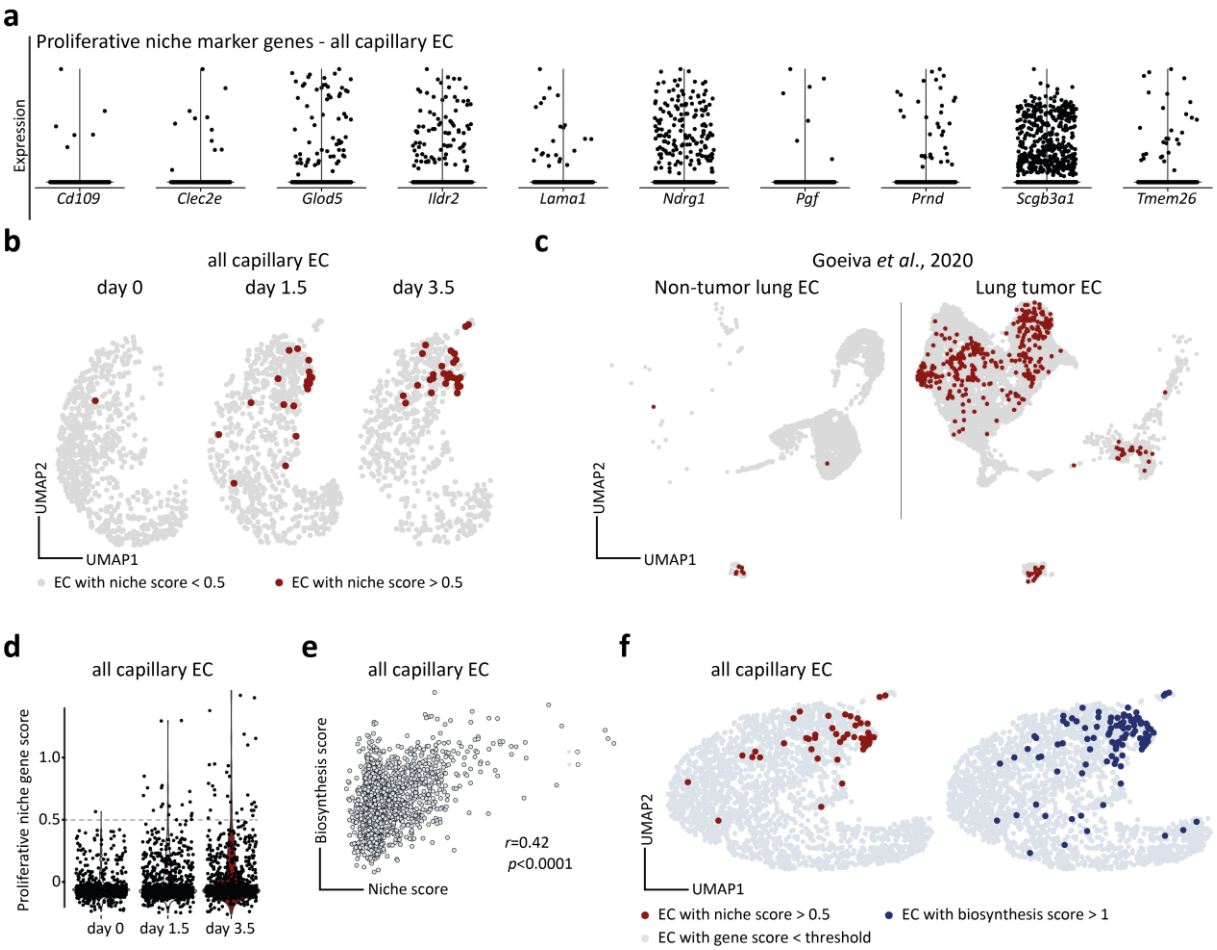

Figure 14: Prediction of tumor cell-interacting endothelial cells. a) Expression profile of proliferative niche marker genes in individual capillary ECs from the combined scRNAseq dataset. **b**) Localization of predicted tumor cell-interacting ECs (niche score > 0.5, red color) in a UMAP of the capillary EC dataset split by timepoint. **c**) Prediction of tumor cell-interacting ECs in a publicly available scRNAseq dataset of control non-tumorous and primary mouse lung tumor ECs. Predicted tumor-interacting ECs are in red. **d**) Gene expression scores for marker genes in **a**) for individual ECs from the combined scRNAseq dataset split by experimental timepoint. Dotted line indicates threshold for ECs with niche gene score > 0.5. **e**) Scatter plot of biosynthesis and niche gene scores in capillary lung ECs. *P* value and *r* value by Pearson correlation are shown. **f**) Localization of tumor cell-interacting ECs (left panel, red dots) and biosynthetic ECs as defined in Fig. 8 (right panel, blue dots).

2.2.7 Tumor cells display surprising baseline transcriptomic heterogeneity

Collectively, the data revealed that metastatic tumor cell behavior in the lung was instructed by angiocrine Wnt-signaling. The regulation of the pathway, however, was not exerted at the receptor-ligand level or by distinct niche occupancy. I, therefore, hypothesized that tumor cell-intrinsic properties might drive the observed differential responsiveness. Surprisingly, and in line with the hypothesis, cultured TCs displayed unexpected heterogeneous baseline EMT states and Wnt-pathway activity (Fig. 15a, b). This pattern was not random, as EMT state and Wnt-activity correlated

in cultured TCs, suggesting that morphologically homogenous cell populations are heterogeneous in their cell state (Fig. 15c). Moreover, a similar heterogeneity in EMT state and Wnt-activity could be observed in freshly isolated CTCs from breast cancer patients [190, 191] (Fig. 15d), suggesting that the observed heterogeneity of cultured TCs reflected the clinical situation.

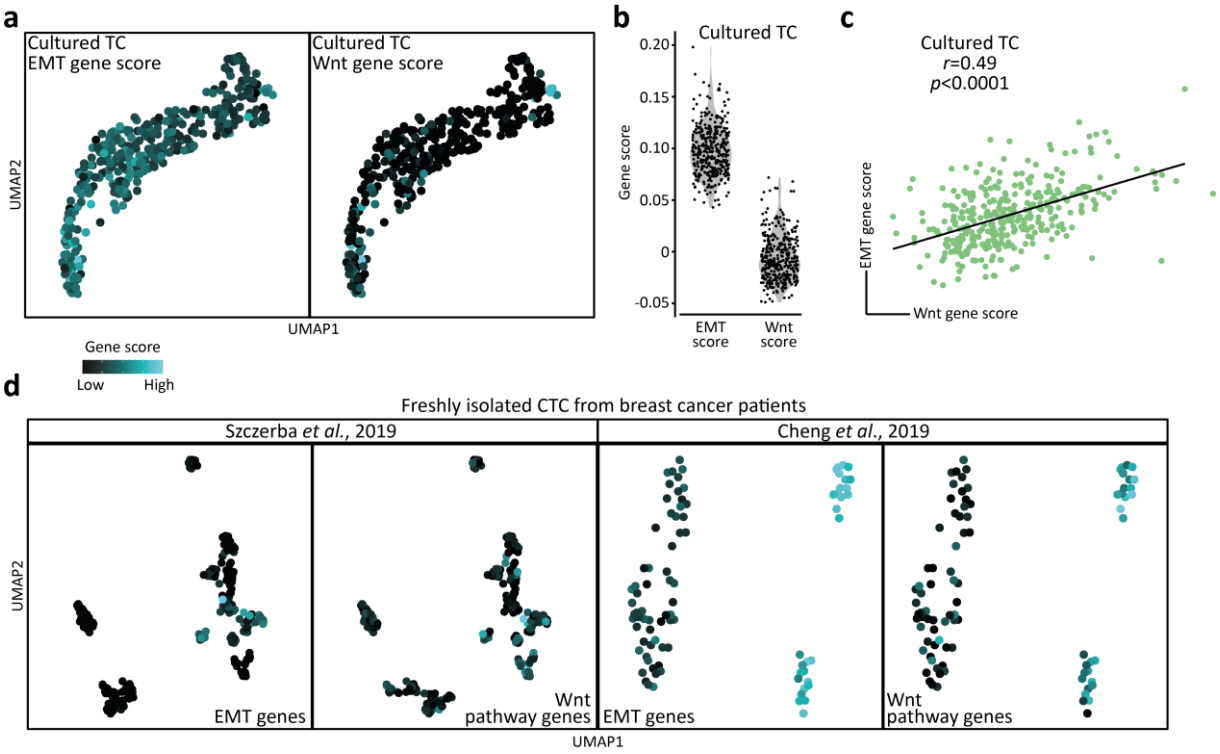

Figure 15: Transcriptional heterogeneity of cultured tumor cells. a) Gene expression scores of EMT (left panel) and Wnt pathway-associated genes (right panel) in cultured TCs visualized in a UMAP and **b**) in a violin plot. **c**) Correlation of the gene expression scores. *P* value and *r* value by Pearson correlation are shown. **d**) Gene scores of EMT and Wnt pathway genes from **a**) in two publicly available datasets of CTCs freshly isolated from breast cancer patients and visualized in a UMAP.

2.2.8 An epigenetic barrier predetermines metastatic tumor cell behavior

As cultured tumor cells were not exposed to exogenous Wnt, the finding of Wnt-high cells could also be interpreted as cellular plasticity that is established at the epigenetic level, which was previously reported for breast cancer CTCs [192]. I found first evidence for an epigenetic barrier that separates the extravasation-dormant phenotype from the intravascular-proliferative phenotype by comparing the metastatic behavior of TCs that received over-night pulse treatment or two weeks of treatment with Wnt-agonists. Only long-term treated TCs exhibited a pronounced shift towards the extravasation-dormancy branch, while pulse-treated TC behavior *in vivo* was not altered compared to vehicle-treated control cells (Fig. 16a, b). This suggested that long-term agonistic treatment led to cellular reprogramming, which affected TC responsiveness towards Wnt *in vivo*, without affecting the

epithelial identity of the carcinoma cells, as evidenced by a similar expression profile of crucial EMT-inducing genes for pulse and long-term treated cells (Fig. 16c, d).

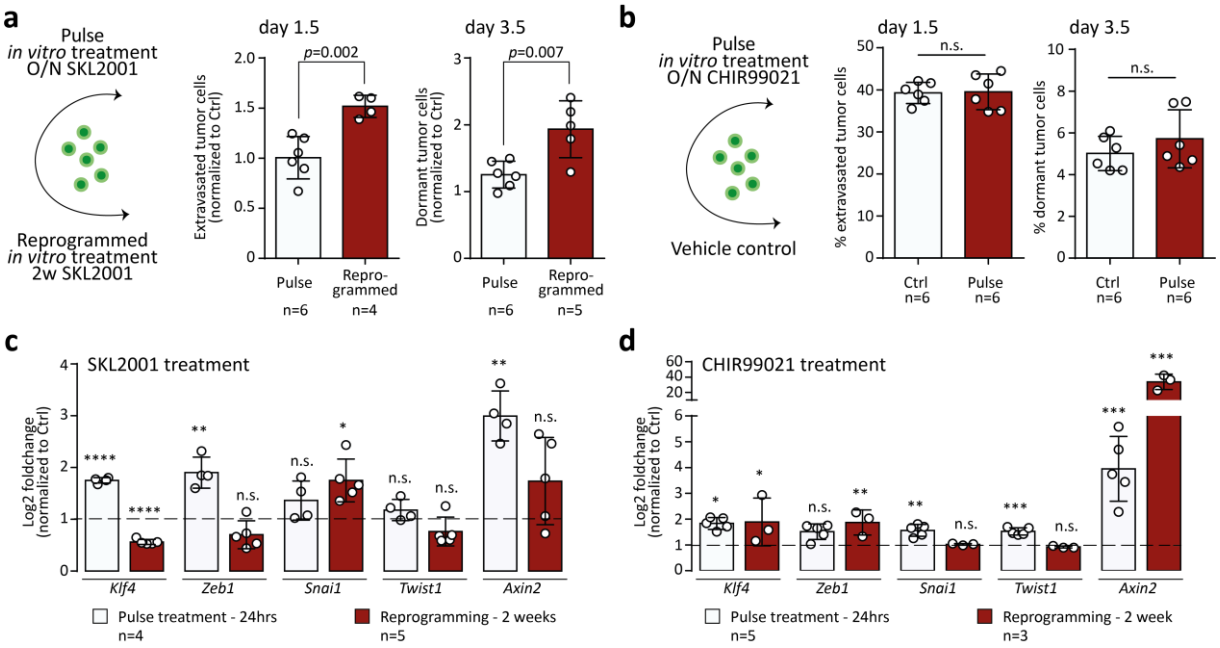

Figure 16: An epigenetic barrier defines tumor cell fates. a) Schematic of the experimental approach. 4T1-GFP cells were either pulse-treated overnight or reprogrammed by two weeks of treatment of SKL2001 prior to injection in mice (left panel). Relative fraction of extravasated TCs normalized to the respective control 1.5 days post-injection (mid panel) and relative fraction of dormant TCs normalized to the respective control 3.5 days post-injection (right panel). Error bars, s.d., *p* values by two-way ANOVA with Sidak post-test are shown. **b**) Schematic of experiment. 4T1-GFP cells were pulse-treated overnight with CHIR99021 or vehicle control prior to injection (left panel). Percentage of extravasated TCs 1.5 days post-injection (mid panel) and percentage of dormant TCs 3.5 days post-injection (right panel). Error bars s.d., *p* values were calculated by two-tailed t-test. n.s., not significant. **c**) Relative expression of key EMT-inducing transcription factors *Klf4*, *Zeb1*, *Snai1* and *Twist1* and canonical Wnt-downstream target *Axin2* in 4T1-GFP cells pulse-treated or reprogrammed with Wnt-agonist SKL2001 or **d**) CHIR-99021. Target gene expression was normalized to *Actb* and relative expression to respective controls was calculated using the $2^{-\Delta\Delta Ct}$-method. Error bars s.d., *p* value by two-tailed t-test are shown. n.s., not significant. * *p* value < 0.05, ** *p* value < 0.01, *** *p* value < 0.001, **** *p* value < 0.0001.

To remove epigenetic barriers, 4T1-GFP cells were treated with the de-methylating drug decitabine. Over-night treatment with the hypomethylating agent did not affect cellular fitness or alter the epithelial identity of the cells (Fig. 17a-d). However, hypomethylation massively increased TC extravasation and induction of dormancy *in vivo* suggesting that epigenetic plasticity underlies TC responsiveness towards niche-derived factors (Fig. 17e, f). This ultimately resulted in a dramatic impairment in metastatic outgrowth, as evidenced by a 2-fold decrease in metastatic tumor cells two weeks post-injection (Fig. 17g). Collectively, these data indicated that epigenetic plasticity renders TCs responsive towards tumor-suppressive niche factors, which induce a stable, dormant phenotype.

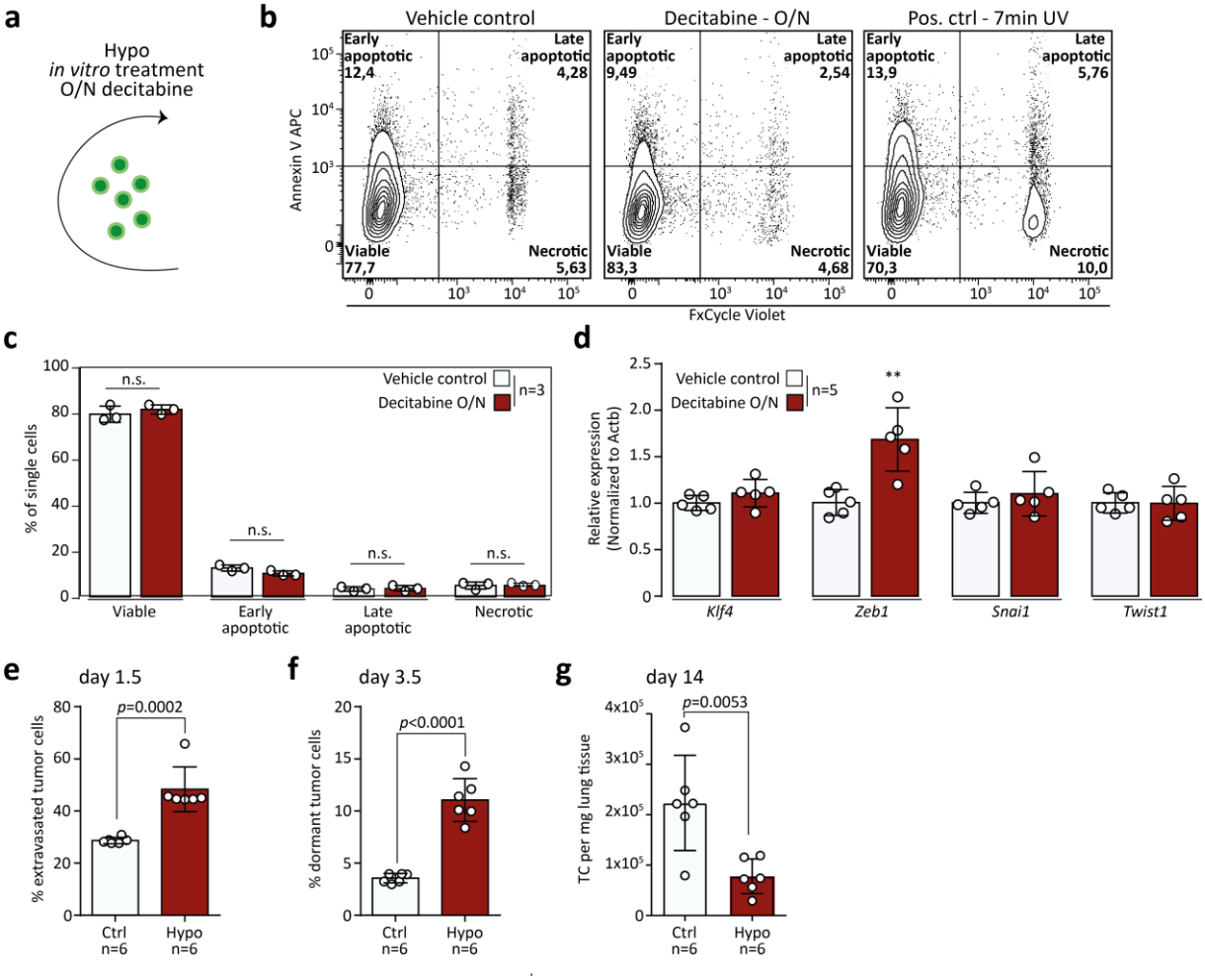

Figure 17: Tumor cell hypomethylation promotes extravasation and dormancy. a) Schematic overview of the experiment. 4T1-GFP cells were treated overnight with the de-methylating agent decitabine. **b**) Representative flow cytometry gates for assessing cell viability of vehicle control treated (left panel), hypomethylated (mid panel) and UV irradiated positive control cells (right panel). **c**) Corresponding quantification of viable, early apoptotic, late apoptotic, and necrotic vehicle control or overnight decitabine-treated 4T1 cells. Error bars s.d., *p* values were calculated by two-tailed t-test. n.s., not significant. **d**) Relative expression of key EMT-inducing transcription factors *Klf4*, *Zeb1*, *Snai1* and *Twist1* in 4T1-GFP cells treated overnight with decitabine or vehicle control. Target gene expression was normalized to *Actb* and relative expression to respective controls was calculated using the $2^{-\Delta\Delta Ct}$-method. Error bars s.d., *p* value by two-tailed t-test is shown. ** *p* value < 0.01. **e**) Overnight decitabine (Hypo) or vehicle control (Ctrl) tumor cells were injected into Balb/c mice. Percentage of extravasated TCs 1.5 days post-injection, **f**) percentage of dormant TCs 3.5 days post-injection and **g**) absolute abundance of TCs per mg lung tissue 14 days post-injection. Error bars s.d., *p* values by two-tailed t-test are shown.

Using a cellular competition model by co-injecting vehicle treated control cells and hypomethylated TCs in a 1:1 ratio confirmed that reduced metastatic outgrowth of hypomethylated TCs was a consequence of dormancy induction and not caused by a diminished homing (Fig. 18a). Importantly, dormancy induction of hypomethylated tumor cells was still dependent on Wnt-signaling, as Wnt L-O-F by means of LGK974 treatment partially rescued the dormant phenotype, as shown by an overall

reduction in DTCs, which consequently resulted in a higher short-term metastatic burden (Fig. 18b). Curiously, Wnt G-O-F by pulse co-treatment of TCs with decitabine and Wnt-agonist did not alter the *in vivo* phenotype (Fig. 18c). Moreover, none of the *in vitro* treatments affected the proliferation capacity of proliferation-committed TCs per se (Fig. 18d). Altogether, these data suggested that niche-derived Wnt-signaling is saturated and that changes in short- and long-term metastatic burden are a direct consequence of dormancy induction and not of altered proliferation rates *in vivo*. Moreover, these findings indicated that tumor cell behavior is primed as early as during the initial arrival of TCs at the metastatic niche, implying that TC behavior is predetermined epigenetically.

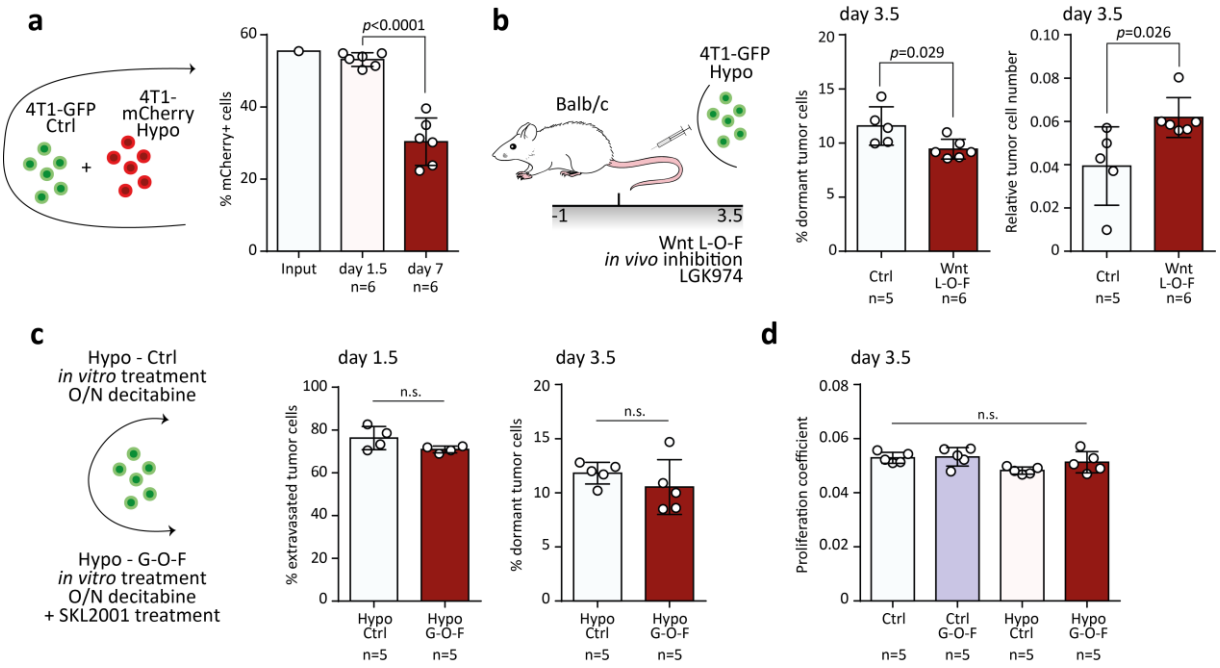

Figure 18: Niche-signaling is saturated and sufficient to instruct dormancy. a) Schematic of experiment. 4T1-EGFP control cells were mixed with over-night decitabine-treated 4T1-mCherry cells in 1:1 ratio and injected into the tail vein of mice (left panel). Quantification of mCherry+ TCs within the TC pool at the timepoint of injection, 1.5 days and 3.5 days post-injection (right panel). Error bars s.d., *p* value by two-tailed t-test is shown. **b**) Schematic of experimental L-O-F approach (left panel). 4T1-GFP cells were treated overnight with decitabine. Grey bar indicates timespan (in days) of daily treatment with LGK974. Percentage of dormant TCs 3.5 days post-injection for control and LGK974 treated animals (mid panel) and relative tumor cell number normalized to lung EC abundance (right panel). Error bars, s.d., *p* values by two-tailed t-test are shown. **c**) Schematic of experiment. 4T1-EGFP cells were treated over-night with either decitabine (Hypo Ctrl) or decitabine and SKL2001 (Hypo G-O-F) and injected into the tail vein of mice. Percentage of extravasated TCs (mid panel) or dormant TCs (right panel) was measured 1.5 days post-injection or 3.5 days post-injection, respectively. Error bars s.d., *p* values were calculated by two-tailed t-test. n.s., not significant. **d**) Proliferation coefficients were calculated as the ratio of CellTracer mean fluorescence intensity (MFI) at day 3.5 and average CellTracer MFI at day 1.5 from matched experiments for 4T1-GFP control cells (Ctrl), SKL2001 reprogrammed cells (Ctrl G-O-F), over-night decitabine treated cells (Hypo Ctrl) and over-night decitabine and SKL2001 treated cells (Hypo G-O-F). Low proliferation coefficients reflect high proliferation rates. Cells with dye retention were excluded from the analysis. Error bars s.d., *p* values were calculated by one-way ANOVA with Tukey post-test. n.s., not significant.

2.2.9 Dormant tumor cells are hypomethylated and respond to angiocrine Wnt

To provide firm evidence that hypomethylation underlies metastatic TC behavior, dormant and proliferative TCs were purified from the metastatic niche using FACS and subjected to whole genome bisulfite-sequencing (WGBS). Surprisingly, dormant TCs did not display global genome-wide hypomethylation (Fig. 19a). However, zooming in on individual genes and gene regulatory elements revealed a general trend for hypomethylation in promoter sequences and gene bodies in dormant TCs, while enhancer sequences were not differentially methylated (Fig. 19b-d). Interestingly, these hypomethylation events mainly occurred in genes and promoters that had high (>70%) methylation levels in proliferative TCs, indicating that especially epigenetically sealed genes were affected. This finding, together with the previous observation that TCs occupy distinct baseline Wnt- and EMT-states supported a model in which demethylation would occur stochastically *in vitro* prior to the injection of the cells with niche factors instructing epigenetically susceptible tumor cells to acquire a dormant phenotype, rather than a signaling-directed demethylation event with subsequent selection *in vivo*. In line with that, computing the overlap of genes with >10% differences in methylation and the mouse signature database [193] revealed the enrichment of general gene programs underlying cellular plasticity, such as transcription factor binding and cell fate processes (Fig. 19e). Collectively, these results strongly suggest that metastatic dormancy is driven by spontaneous hypomethylation events that establish epigenetic plasticity, which renders TCs responsive towards homeostatic niche-derived dormancy-inducing factors.

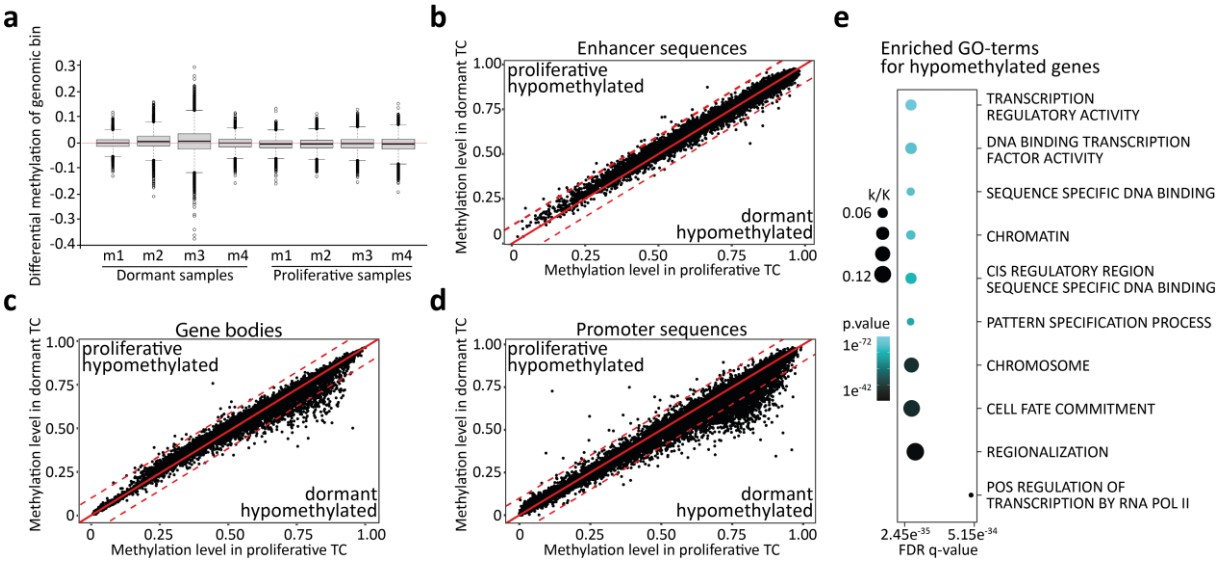

Figure 19: Dormant tumor cells are hypomethylated. a) Boxplot reflecting the genome-wide differential methylation level. Genome was binned in parts of 2000 bp. Methylation fractions were calculated for each bin by the ratio of methylated to total CpG island per bin. Methylation levels were assessed by subtracting the median methylation fraction of a bin across all samples from each individual bin. Red line indicates median methylation fraction of genomic bin. Black lines indicate median methylation level for each sample. **b**) Scatter plot of methylation level (fraction of methylated CpG islands) for enhancer sequences, **c**) gene bodies and **d**) promoters in dormant TCs and proliferative TCs. Red line indicates no differences in methylation for a sequence between dormant and proliferative sample, dotted red lines indicate thresholds for >10% differences in methylation, with the upper dotted line representing the threshold for sequences hypomethylated in proliferative samples and the lower dotted line for hypomethylated sequences in dormant samples. **e**) Enriched GO-terms for hypomethylated genes in dormant TCs. k/K, overlap of queried gene list and GO-term associated genes. FDR, false discovery rate.

Discussion

3.1 Cellular predetermination drives metastatic fates

Tumor cell predetermination is an emerging concept. Recent work has identified rare subtypes within morphologically homogeneous melanoma cell lines that express an intrinsic drug resistance program. Upon applying selective pressure, these rare subtypes emerge and reconstitute the cell pool, thereby leading to tumor recurrence and therapy-resistance. Notably, the cellular resistance program was found to be inheritable and stably expressed over several cell divisions [194-197]. Conceptually similar, but more general observations were made by comparing the metastatic phenotypes of xenografted cell lines [181]. A key finding of the study was that the metastatic behavior of the individual cell pools was predictable and inheritable, arguing for the genomic or epigenomic control of metastasis. However, up until now, no direct proof of an underlying epigenetic control of the observed transcriptomic and phenotypic heterogeneity was provided.

In this dissertation, DNA methylation was identified as a key regulator of metastatic tumor cell behavior. Tumor cell hypomethylation enabled tumor cell responsiveness towards dormancy-inducing metastatic niche-derived factors. I hypothesize that in culture, the epigenetically sealed non-responsive state forms an equilibrium with the plastic-responsive state, which is established by stochastic de-methylation events within the cell. This hypothesis is supported by the finding that changes in methylation between dormant and proliferative cells were subtle and mostly occurred in genes that had a high abundance of CpG methylation sites and high methylation status. Strongly methylated genes would thereby have a higher likelihood of spontaneously losing methylation. Moreover, stochastic de-methylation events would explain why agonistic treatment of tumor cells only resulted in phenotypes in long-term treatment approaches.

Assuming that metastatic niche-derived signaling is saturated, the gain-of-function would require the epigenetic remodeling of tumor cells. In a stochastic model, the plastic cell state would be stabilized by agonistic treatment, leading to a linear accumulation of dormancy-prone plastic tumor cells in the culture dish. The metastatic behavior at the population level would therefore correlate with treatment time. Here, two weeks of treatment led to a 2-fold increase in dormant tumor cells. Given the initial rarity of dormant tumor cells in the culture dish, it is no surprise that bulk assessment of gene expression programs between pulse and reprogrammed TCs did not reveal major changes, and the core cellular identity presumably was maintained. However, phenotype-switching by long-term *in vitro* treatment or by targeted genetic manipulation that directly affected the metastatic potential was reported previously [198, 199]. Prolonging the treatment in this study or assessing cellular heterogeneity at the single-cell level could therefore ultimately answer this question.

Epigenetic plasticity and accompanying state transitions were also observed *in vivo*. Circulating tumor cells that were freshly isolated from breast cancer patients showed remarkable heterogeneity

in DNA methylation, which was further identified as a driver of metastatic potential [192]. Additionally, the epigenetic control of the transcriptional regulator nuclear receptor subfamily 2 group F member 1 (NR2F1) was found to directly regulate dormancy in breast cancer [200]. Colorectal cancer cells were shown to display tremendous state transition potential, switching from a primary tumor-like phenotype, as evidenced by expression of Leucine-rich repeat-containing G-protein coupled receptor 5 (LGR5), to a disseminating phenotype that is void of Lgr5 during metastasis and reverting to the Lgr5 expressing phenotype that eventually is a pre-requisite for metastatic outgrowth [201].

These data also indicate that the primary tumor serves as a heterogenic amplifier that raises distinct cell states that arise through exposure to high selective pressures, thereby enabling seamless cell state continua. For instance, EMT was identified as a master regulator of metastatic dissemination. However, against prevailing views, EMT is not discrete but also exists in intermediate states, generating tumor cells of hybrid epithelial-mesenchymal characteristics [182, 202, 203]. While EMT is necessary for intravasation and dissemination, too much EMT limits metastatic outgrowth [182]. In this dissertation, the mesenchymal-phenotype of cancer cells also correlated with dormancy. While disseminated tumor cells maintained their epithelial identity and did not upregulate classical EMT-associated genes, such as *N-Cadherin* or the transcription factors *Snail* and *Twist*, the overall phenotype of dormant tumor cells was found to be mesenchymal-like. These EMT high cells could already be observed in cell culture and were likely established as a direct consequence of the removal of epigenetic barriers. Epigenetically plastic cells would show high EMT states and follow the extravasation-dormancy route, whereas epigenetically sealed TCs would form macro-metastases. Probing the epigenetic and transcriptomic state of CTCs could therefore serve as a crucial diagnostic tool to assess the likelihood of metastatic relapse and therapy resistance.

3.2 Instructive niche-factors: beyond classical signaling molecules

In this work, the metastatic fate of TCs was found to depend on both epigenetic predetermination and instructive niche-derived signaling molecules. The data identified endothelium-derived angiocrine Wnt-signaling as a prototypic example of such interdependency, by exploiting hypomethylated TC states and instructing an extravasation-dormancy phenotype. This was insofar surprising, as Wnt ligands were previously reported as crucial growth factors during primary tumor growth, but also for CTC survival and metastatic outgrowth in the lung niche [167, 186, 204]. However, these studies focused exclusively on the implications of autocrine Wnt signaling. Autocrine Wnt was found to promote cell survival of pancreatic cancer CTCs and anti-androgen therapy resistance in the metastatic niche while metastasizing lung cancer dormant TCs upregulated dickkopf WNT signaling pathway inhibitor 1 (DKK1) to block growth promoting autocrine Wnt signaling [167,

204, 205]. Contrarily, dormant lung metastases of melanoma were shown to require autocrine Wnt signaling to maintain their quiescent phenotype. Recent work established that ageing is accompanied by altered transcriptional programs of lung stromal cells, leading to the secretion of Wnt-scavenging secreted frizzled related protein 1 (sFRP1), which in turn blocked the quiescence-inducing autocrine Wnt-loop and awoke dormant melanoma by phenotype switching [168]. Similarly, Wnt-signaling in prostate cancer bone metastasis was described to promote dormancy [166], highlighting the multifaceted role of the signaling-pathway during metastasis.

The context-dependent pro-proliferative or dormancy-inducing properties of Wnt-signaling could be explained by the general promiscuity of the pathway. With 19 known ligands and 15 receptors and co-receptors [50] in combination with the short transcript half-life of Wnt-ligands [14], the pathway can be tightly regulated and is likely to crosstalk with other niche-derived signaling cues. Most notably, in this work, dormant TCs were found to be enriched for Wnt- and TGFβ-associated genes. Both pathways were previously shown to converge and act synergistically [206]. Given the well-established role of TGFβ as a dormancy-maintainer [163-165], a similar synergy could underlie dormancy-induction. In line with this hypothesis are the numerous reports that so far identified a multitude of factors and cellular sources that are relevant for the establishment and maintenance of metastatic dormancy, clearly neglecting the possibility of a one-master pathway regulation [146, 207-210].

One of the most intriguing findings of this study was that homeostatic niche-signaling was sufficient to drive metastatic tumor cell behavior, which opens new opportunities regarding disease prediction and therapeutic intervention [139, 161, 162]. In this sense, the lung niche was identified as a default tumor-suppressor. Similar default states were reported previously for example in the bone [163] or skeletal muscle [170]. While bone and lung instruct dormancy by active signaling, the skeletal muscle impairs metastatic growth through reactive oxygen species (ROS) [170]. Biophysical parameters, such as matrix stiffness or mechanical stretching of cells were identified as other crucial regulators of metastatic behavior. This work provided first evidence that proliferating TCs actively instructed cells of the micro-niche to produce extracellular matrix (ECM), whereas dormant TCs failed to do so. Changing the biophysical parameters of the niche was shown to have drastic effects on disseminated TC phenotypes. Inflammation-induced remodeling events were sufficient to awaken long-term dormant TCs and promote metastasis formation [175]. Similarly, the stripping of astrocytic laminin in the perivascular brain niche was found to precede the metastatic outgrowth of dormant tumor cells [171]. These remodeling events ultimately led to the mechanical stretching of the cells, which resulted in activation of the Hippo-pathway and YAP/TAZ-directed proliferation [157].

It was previously shown that primary tumor-derived signaling leads to remodeling events in non-tumorous tissues [120, 121, 123, 129, 130, 178], which could change the default metastatic

properties of the niche. The necessity for pre-metastatic niche establishment for metastatic outgrowth was recently put in question by the finding that, in contrast to the long-prevailing view, dissemination is an early event during tumor progression [134, 137, 138]. Putting these findings in context, rather than establishing a pre-metastatic niche, primary tumor-derived signals could actively reshape the micro-niche of single disseminated tumor cells and thereby initiate metastatic outgrowth. Besides producing biomass and ECM in the micro-niche, this work solidified previous findings that the endothelium acts as a systemic signaling compartment with immune-regulatory function through the release of angiokines [129]. However, the ramifications of endothelial-immune regulation during metastatic disease and differences in signaling between dormant and proliferative phases of metastasis remain elusive.

3.3 A new model of metastatic tumor cell fate decisions

In conclusion, enabled by a unique experimental approach that captures all states of the metastatic colonization process in combination with scRNAseq, the present study provides the first blueprint of the transcriptional events underlying tumor cell fate decisions in the metastatic niche. Moreover, beyond identifying the transcriptional basis of tumor cell fate decisions, the extensive scRNAseq analyses in combination with *in vivo* labeling techniques also enabled the first deconvolution of systemic and micro-niche-specific responses of endothelium that is in contact with metastasizing tumor cells. The subsequent functional and mechanistic experiments identified angiocrine Wnt-signaling as a critical instructor of dormancy during the early steps of metastatic colonization. The data thereby integrate the synergistic involvement of several previously reported signaling pathways with novel tumor cell – endothelial cell interaction mechanisms that exert critical and rate-limiting functions during the metastatic cascade. This is of particular importance as the here presented findings demonstrate that homeostatic niche signaling is sufficient to exploit susceptible metastatic tumor cell states. Systemic changes may affect this default niche-signaling, thereby altering the course of disease progression. The present study, therefore, reflects a real paradigm-shift, as the default state of the niche and the molecular make-up of the tumor cell were identified to be of equal importance for the eventual metastatic outcome. Most importantly, the study identified the predetermination of tumor cell behavior in the metastatic niche. This will open a whole new field of single-cell-based diagnostics and disease monitoring, as the resolved predetermination pattern might enable disease course prediction. Lastly, in light of recent literature, the data advocate a model in which the primary tumor serves as a heterogenic amplifier that raises distinct tumor cell states with predetermined metastatic fates. Upon reaching the metastatic site, tumor cell fates are coined by default niche signaling. Once committed to their predestined fate, tumor cells actively change their

micro-niche to generate positive-feedback loops fueling their proliferative or quiescent phenotype (Fig. 20).

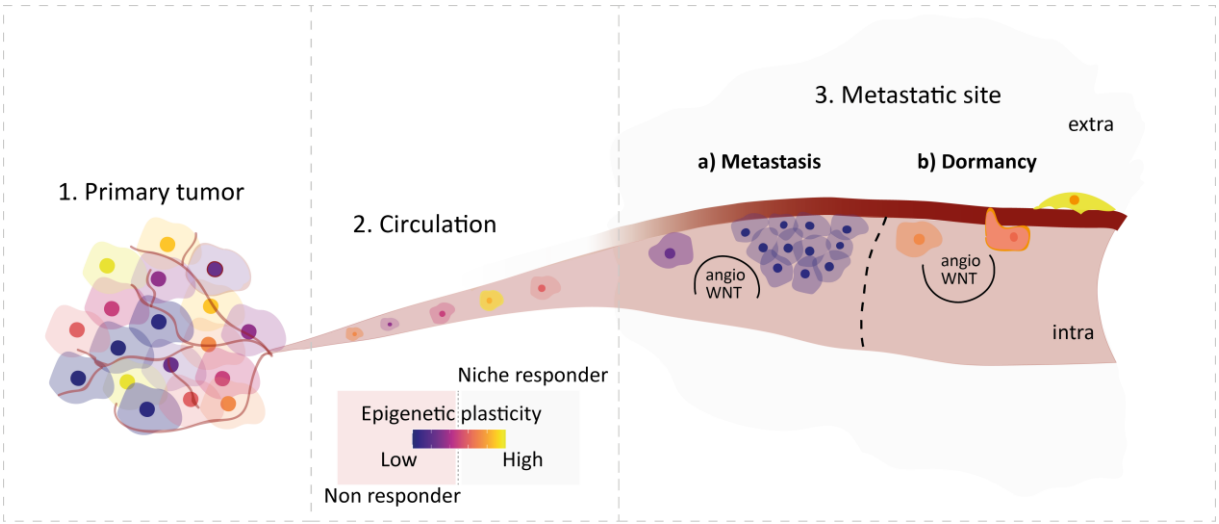

Figure 20: Mechanistic model. 1) The primary tumor serves as a heterogenic amplifier and raises TCs of distinct states. **2**) Upon entry in the blood stream, TC behavior is predetermined based on the epigenetic status, which defines whether TC will respond to niche factors. Niche responder, cells that respond to niche factors due to epigenetically plastic state. Non responder, epigenetically sealed cells that do not respond to niche factors. **3**) At the metastatic site, TCs are primed by angiocrine Wnt factors. **a**) Epigenetically sealed cells do not respond to Wnt and proliferate intraluminally to form metastasis. **b**) Epigenetically plastic cells respond to angiocrine Wnt ligands and extravasate to establish metastatic latency that is poised for dormancy. Angio WNT, angiocrine Wnt factors. intra, intravascular. extra, extravascular.

Materials and Methods

4.1 Materials

4.1.1 Chemicals

Chemicals used in this study were purchased from the following vendors:

Table 2: Chemicals

Company
AppliChem (www.applichem.com)
Carl Roth (www.carl-roth.de)
Gerbu (www.gerbu.de)
Merck (www.merk.de)
Roche (www.roche-applied-science.com)
Selleckchem (www.selleckchem.com)
Serva (www.serva.de)
Sigma Aldrich (www.sigmaaldrich.com)
Thermo Fisher Scientific (www.thermofisher.com)

4.1.2 Enzymes

Table 3: Enzymes

Reagent	Company
Liberase	Roche
Proteinase K	Gerbu
RNase free DNAse	R&D Systems
SuperScript™ II Reverse Transcriptase	Thermo Fisher Scientific

4.1.3 Cells

Table 4: Murine cell lines

Cell	Description	Source	Culture condition
4T1-GFP	Breast cancer cell line with GFP reporter	Dr. Robert Weinberg	DMEM + 10% FCS 1% PenStrep
4T1-GFP_tatCherry	Breast cancer cell line with GFP reporter + niche labeling construct	Dr. Robert Weinberg Dr. Ilaria Malanchi	DMEM + 10% FCS 1% PenStrep
4T1_mCherry	Breast cancer cell line with mCherry reporter	Dr. Robert Weinberg	DMEM + 10% FCS 1% PenStrep
B16F10	Melanoma cell line	ATCC	DMEM + 10% FCS 1% PenStrep
E0771-GFP	Breast cancer cell line with GFP reporter	Dr. Kairbaan Hodivala-Dilke	DMEM + 10% FCS 1% PenStrep
D2.0R-GFP	Breast cancer cell line with GFP reporter	Dr. Jonathan Sleeman	DMEM + 10% FCS 1% PenStrep
D2.0R-GFP_tatCherry	Breast cancer cell line with GFP reporter + niche labeling construct	Dr. Jonathan Sleeman Dr. Ilaria Malanchi	DMEM + 10% FCS 1% PenStrep

4.1.4 Reagents

4.1.4.1 Cell culture reagents

Table 5: Cell culture reagents

Reagent	Company
CHIR-99021	Selleckchem
Decitabine	Sigma Aldrich
Dimethylsulfoxide (DMSO)	AppliChem
Dulbecco's Modified Eagle medium - Glutamax (DMEM)	Thermo Fisher Scientific
Dulbecco´s phosphate buffered saline (PBS)	PAA
Fetal Calf Serum (FCS, heat inactivated)	PAA
Penicillin/streptomycin 100x 104U/10mg/ml (P/S)	PAA
SKL2001	Selleckchem
Trypan blue	Thermo Fisher Scientific
Trypsin-EDTA (10x)	Sigma Aldrich

4.1.4.2 PCR reagents

Table 6: Reagents for RT, PCR, qPCR and SMART-Seq2

Reagent	Company
Agencourt Ampure XP beads	Beckman Coulter
Betaine (5M)	Sigma Aldrich
Direct PCR Lysis Reagent	PeqLab
DNAaway	Thermo Fisher Scientific
DNase/RNase free H_2O	Thermo Fisher Scientific
Ethidium bromide	Roth
dNTP	Thermo Fisher Scientific
Magnesium chloride	Sigma Aldrich
KAPA HiFi HotStart ReadyMix	Roche
O'Generuler 100bp Plus DNA ladder	Thermo Fisher Scientific
O'Generuler 1kb Plus DNA ladder	Thermo Fisher Scientific
RedTaq® ReadyMix™ PCR Reaction Mix	Sigma-Aldrich
RNaseOUT	Thermo Fisher Scientific
RNaseZAP	Thermo Fisher Scientific
Taq DNA Polymerase	Qiagen
Taq DNA Polymerase Buffers	Qiagen
TaqMan® Fast Advanced PCR Master Mix	Thermo Fisher Scientific
Triton X-100	Sigma Aldrich

4.1.4.3 Staining reagents

Table 7: Staining reagents

Reagent	Company
CellTrace Violet	Thermo Fisher Scientific
CountBright Absolute Counting Beads	Thermo Fisher Scientific
Fixable Viability Dye eFluor™ 780	Thermo Fisher Scientific
Fluorescent mounting medium	Dako
FxCycle Violet	Thermo Fisher Scientific
Histomount	Thermo Fisher Scientific
Hoechst Dye 33258	Merck
Normal goat serum ready-to-use	Zymed

Reagent	Company
OneComp eBeads™ Compensation Beads	Thermo Fisher Scientific
Roti-Histofix 4%	Roth
Target Retrieval, pH 6.0	Dako
Tissue-Tek O.C.T. Compound	Sakura

4.1.4.4 Reagents for animal experimentation

Table 8: Reagents and tools for animal experimentation

Reagent	Company
4-hydroxy-tamoxifen	Merck
Bepanthen eye cream	Roche
Betaisodona	Mundipharma
Corn oil	Sigma Aldrich
Ethicon suture silk 4-0	Johnson & Johnson MEDICAL
Ethicon suture silk 5-0	Johnson & Johnson MEDICAL
Ketavet	Pfizer
LGK974	Selleckchem
Methylcellulose	Sigma Aldrich
NaCl solution 0.9%	Braun
Rompun	Bayer
Surgical tools and equipment	Fine Science Tools
Tween80	Sigma Aldrich

4.1.5 Kits

Table 9: Kits and RNA/DNA detection

Reagent	Company
Agilent High Sensitivity DNA Kit	Agilent
Agilent High Sensitivity DNA Kit	Agilent
Agilent High Sensitivity RNA Kit	Agilent
Agilent High Sensitivity RNA Kit	Agilent
Arcturus PicoPure RNA Isolation Kit	Thermo Fisher Scientific
GenElute Mammalian Total RNA Purification Kit	Merck

Reagent	Company
Genomic DNA ScreenTape	Agilent
Genomic DNA Reagents	Agilent
NEBNext® Ultra™ II DNA Library Prep Kit for Illumina	NEB
Nextera XT DNA Library Preparation	Illumina
NucleoSpin tissue mini kit for DNA from cells and tissue	Macherey-Nagel
High Sensitivity D1000 ScreenTape	Agilent
High Sensitivity D1000 Reagents	Agilent
Quant-iT™ DNA HS Assay	Thermo Fisher Scientific
QuantiTect Reverse Transcription Kit for cDNA Synthesis	Qiagen
Qubit DNA HS (High Sensitivity) Assay-Kit	Thermo Fisher Scientific
Qubit RNA HS (High Sensitivity) Assay-Kit	Thermo Fisher Scientific
RNeasy Mini Kit	Qiagen

4.1.6 Primers

Table 10: Primers and oligos

Name	Application	Sequence: 5'-3'
Actb-Fwd	Genotyping	CAATGGTAGGCTCACTCTGGGAGATGATA
Actb-Rev	Genotyping	AACACACACTGGCAGGACTGGCTAGG
Cre-Fwd	Genotyping	GCCTGCATTACCGGTCGATGCAACGA
Cre-Rev	Genotyping	GTGGCAGATGGCGCGGCAACACCATT
Wls-Fwd	Genotyping	AAGGAAACGAGATTGAGATGAGG
Wls-Rev	Genotyping	GTTTATTTTTCCTCTTACCACTCTG
oligo-dT	scRNAseq + RNAseq	AAGCAGTGGTATCAACGCAGAGTACTTTTTTTTTTTTTTTTTTTTTTTTTTTTVN
IS-PCR	scRNAseq + RNAseq	AAGCAGTGGTATCAACGCAGAGT
TSO	scRNAseq + RNAseq	AAGCAGTGGTATCAACGCAGAGTACATrGrG+G * riboguanosines (rG)/LNA-modified guanosine (+G)
501	index-scRNAseq	AATGATACGGCGACCACCGAGATCTACACTAGATCGCTCGTCGGCAGCGTCAGATGTG
502	index-scRNAseq	AATGATACGGCGACCACCGAGATCTACACCTCTCTATTCGTCGGCAGCGTCAGATGTG
503	index-scRNAseq	AATGATACGGCGACCACCGAGATCTACACTATCCTCTTCGTCGGCAGCGTCAGATGTG
504	index-scRNAseq	AATGATACGGCGACCACCGAGATCTACACAGAGTAGATCGTCGGCAGCGTCAGATGTG
505	index-scRNAseq	AATGATACGGCGACCACCGAGATCTACACGTAAGGAGTCGTCGGCAGCGTCAGATGTG
506	index-scRNAseq	AATGATACGGCGACCACCGAGATCTACACACTGCATATCGTCGGCAGCGTCAGATGTG

Name	Application	Sequence: 5'-3'
507	index-scRNAseq	AATGATACGGCGACCACCGAGATCTACACAAGGAGTATCGTCGGCAGCGTCAGATGTG
508	index-scRNAseq	AATGATACGGCGACCACCGAGATCTACACCTAAGCCTTCGTCGGCAGCGTCAGATGTG
509	index-scRNAseq	AATGATACGGCGACCACCGAGATCTACACTGGAAATCTCGTCGGCAGCGTCAGATGTG
510	index-scRNAseq	AATGATACGGCGACCACCGAGATCTACACAACATGATTCGTCGGCAGCGTCAGATGTG
511	index-scRNAseq	AATGATACGGCGACCACCGAGATCTACACTGATGAAATCGTCGGCAGCGTCAGATGTG
512	index-scRNAseq	AATGATACGGCGACCACCGAGATCTACACGTCGGACTTCGTCGGCAGCGTCAGATGTG
513	index-scRNAseq	AATGATACGGCGACCACCGAGATCTACACTTTCTAGCTCGTCGGCAGCGTCAGATGTG
514	index-scRNAseq	AATGATACGGCGACCACCGAGATCTACACTAACCAAGTCGTCGGCAGCGTCAGATGTG
515	index-scRNAseq	AATGATACGGCGACCACCGAGATCTACACGTGTATCGTCGTCGGCAGCGTCAGATGTG
516	index-scRNAseq	AATGATACGGCGACCACCGAGATCTACACTCCATCAATCGTCGGCAGCGTCAGATGTG
N701	index-scRNAseq	CAAGCAGAAGACGGCATACGAGATTCGCCTTAGTCTCGTGGGCTCGGAGATGT
N702	index-scRNAseq	CAAGCAGAAGACGGCATACGAGATCTAGTACGGTCTCGTGGGCTCGGAGATGT
N703	index-scRNAseq	CAAGCAGAAGACGGCATACGAGATTTCTGCCTGTCTCGTGGGCTCGGAGATGT
N704	index-scRNAseq	CAAGCAGAAGACGGCATACGAGATGCTCAGGAGTCTCGTGGGCTCGGAGATGT
N705	index-scRNAseq	CAAGCAGAAGACGGCATACGAGATAGGAGTCCGTCTCGTGGGCTCGGAGATGT
N706	index-scRNAseq	CAAGCAGAAGACGGCATACGAGATCATGCCTAGTCTCGTGGGCTCGGAGATGT
N707	index-scRNAseq	CAAGCAGAAGACGGCATACGAGATGTAGAGAGGTCTCGTGGGCTCGGAGATGT
N708	index-scRNAseq	CAAGCAGAAGACGGCATACGAGATCCTCTCTGGTCTCGTGGGCTCGGAGATGT
N709	index-scRNAseq	CAAGCAGAAGACGGCATACGAGATAGCGTAGCGTCTCGTGGGCTCGGAGATGT
N710	index-scRNAseq	CAAGCAGAAGACGGCATACGAGATCAGCCTCGGTCTCGTGGGCTCGGAGATGT
N711	index-scRNAseq	CAAGCAGAAGACGGCATACGAGATTGCCTCTTGTCTCGTGGGCTCGGAGATGT

Name	Application	Sequence: 5'-3'
N712	index-scRNAseq	CAAGCAGAAGACGGCATACGAGATTCCTCTACGTCTCGTGGGCTCGGAGATGT
N713	index-scRNAseq	CAAGCAGAAGACGGCATACGAGATATCACGACGTCTCGTGGGCTCGGAGATGT
N714	index-scRNAseq	CAAGCAGAAGACGGCATACGAGATACAGTGGTGTCTCGTGGGCTCGGAGATGT
N715	index-scRNAseq	CAAGCAGAAGACGGCATACGAGATCAGATCCAGTCTCGTGGGCTCGGAGATGT
N716	index-scRNAseq	CAAGCAGAAGACGGCATACGAGATACAAACGGGTCTCGTGGGCTCGGAGATGT
N717	index-scRNAseq	CAAGCAGAAGACGGCATACGAGATACCCAGCAGTCTCGTGGGCTCGGAGATGT
N718	index-scRNAseq	CAAGCAGAAGACGGCATACGAGATAACCCCTCGTCTCGTGGGCTCGGAGATGT
N719	index-scRNAseq	CAAGCAGAAGACGGCATACGAGATCCCAACCTGTCTCGTGGGCTCGGAGATGT
N720	index-scRNAseq	CAAGCAGAAGACGGCATACGAGATCACCACACGTCTCGTGGGCTCGGAGATGT
N721	index-scRNAseq	CAAGCAGAAGACGGCATACGAGATGAAACCCAGTCTCGTGGGCTCGGAGATGT
N722	index-scRNAseq	CAAGCAGAAGACGGCATACGAGATTGTGACCAGTCTCGTGGGCTCGGAGATGT
N723	index-scRNAseq	CAAGCAGAAGACGGCATACGAGATAGGGTCAAGTCTCGTGGGCTCGGAGATGT
N724	index-scRNAseq	CAAGCAGAAGACGGCATACGAGATAGGAGTGGGTCTCGTGGGCTCGGAGATGT

4.1.7 Taqman assays

Table 11: Taqman probes for qPCR

Gene	Application	Cat.nr.:
Wls	qPCR	Mm00509695_m1
Klf4	qPCR	Mm00516104_m1
Zeb1	qPCR	Mm00495564_m1
Snai1	qPCR	Mm00441533_g1
Twist1	qPCR	Mm00442036_m1
Axin2	qPCR	Mm00443610_m1

4.1.8 Antibodies

Table 12: Flow cytometry and immunofluorescence antibodies

Antigen	Clone/Cat.nr.	Dye	Dilution	Application	Company
CD31	MEC13.3	APC	1:200	FC	BD Biosciences
CD31	MEC13.3	PE	1:200	FC	BD Biosciences
CD31	MEC13.3	BV786	1:200	FC	BD Biosciences
CD31	MEC13.3	BV711	1:200	FC	BD Biosciences
CD45	30-F11	APC	1:400	FC	BD Biosciences
CD45	30-F11	PE	1:400	FC	BD Biosciences
CD45	30-F11	BV786	1:400	FC	BD Biosciences
TER-119	TER-119	APC	1:200	FC	BD Biosciences
TER-119	TER-119	PE	1:200	FC	BD Biosciences
TER-119	TER-119	BV785	1:200	FC	BioLegend
LYVE1	ALY7	eFluor660	1:250	FC	Thermo Fisher Scientific
LYVE1	ALY7	eFluor615	1:250	FC	Thermo Fisher Scientific
PDPN	eBio8.1.1	PE	1:200	FC	Thermo Fisher Scientific
PDPN	eBio8.1.1	eFluor660	1:200	FC	Thermo Fisher Scientific
CD324	DECMA-1	PE	1:200	FC	BioLegend
CD324	DECMA-1	AF647	1:200	FC	BioLegend
H2-Kd	SF1-1.1	APC	5µg	In vivo	BioLegend
H2-Kd	SF1-1.1	AF647	5µg	In vivo	BioLegend
H2-Kd	SF1-1.1	PE	5µg	In vivo	BioLegend
mouse IgG2α κ isotype	MOPC-173	APC	5µg	In vivo	BioLegend
mouse IgG2α κ isotype	MOPC-173	AF647	5µg	In vivo	BioLegend
mouse IgG2α κ isotype	MOPC-173	PE	5µg	In vivo	BioLegend
CD31	MEC13.3	-	1:100	IF-primary	BD Biosciences
Desmin	polyclonal/ab15200	-	1:100	IF-primary	Abcam
donkey anti-rabbit	polyclonal/A10040	AF546	1:500	IF-secondary	Thermo Fisher Scientific
chicken anti-rat	polyclonal/A-21472	AF647	1:500	IF-secondary	Thermo Fisher Scientific

4.1.9 Consumables

Table 13: Plastic ware and consumables

Consumable	Company
96 well plates - PCR	Steinbrenner Laborsysteme
96 well plates - non skirted - scRNAseq	Thermo Fisher Scientific
384 well plates - PCR	4titute
384 well plates - scRNAseq	Eppendorf
384 well plates – black wall	Corning
Biopsy punches	Stiefel
Cannula (18G)	BD Biosciences
Cell culture dishes (6 well plates, 10cm, 15cm)	Sarstedt
Cell strainer	BD Biosciences
Cotton swap	Edeka elcos face
Countess cell counting chamber slides	Thermo Fisher Scientific
Cryotubes	Roth
FACS tubes	BD Biosciences
FACS tubes with strainer cap	Corning
Microscope cover glasses	VWR international
Microscope glass slides	Menzel-Gläser
Octenisept	Schülke
Peel-A-Way Embedding Molds	Merck
Pipette tips	Nerbe
Pipette tips - filter	Sarstedt
Pipette tips - multichannel	Rainin
Pipette tips – multichannel electric	Integra
Pipette tips – low retention	Starlab
Reaction tubes (0.2, 0.5ml, 1.5ml, 2ml)	Eppendorf
Reaction tubes (1.5ml) - DNA LoBind	Eppendorf
Reaction tubes (1.5ml) - Biopur	Eppendorf
Reaction tubes (15ml, 50 ml)	Greiner
Sealing foil - qPCR	Thermo Fisher Scientific
Sealing foil - qpCR	4titude
Sealing foil - aluminium	Thermo Fisher Scientific

Consumable	Company
Sealing foil - scRNAseq	Sarstedt
Sterile pipettes	Corning
Syringe - SoftJect 1ml	Thermo Fisher Scientific
Syringe – Insulin 1ml 30G	SFM Hospital Products

4.1.10 Devices

Table 14: Devices and equipment

Equipment	Company
Agilent 2100 Bioanalyzer	Agilent
Agilent 4200 TapeStation	Agilent
Agarose gel documentation system	Peqlab
Aria cell sorting platform	BD Biosciences
BD LSRFortessa™ Cell Analyzer	BD Biosciences
Canto II BD Biosciences	BD Biosciences
Cell culture hood	Thermo Fisher Scientific
Cell culture incubator Thermo Fisher Scientific	Thermo Fisher Scientific
Centrifuge	Eppendorf
Classic E.O.S film developer	Agfa
Countess automated cell counter	Thermo Fisher Scientific
Digital Electronic Caliper	Fine Science Tools
Freezing box	Thermo Fisher Scientific
Heating block	Eppendorf
HM355S microtome	Thermo Fisher Scientific
Light cycler 480	Roche
MasterCycler 384-Well	Eppendorf
Magnetic stand	Thermo Fisher Scientific
Microtome Hyrax C50 Zeiss	Merck
Mosquito LV	SPTLabtech
Multistep pipette	Eppendorf
Multichannel pipette	Rainin
Multichannel pipette electric	Integra
Mr. Frosty Freezing Container	Thermo Fisher Scientific

Equipment	Company
Nanophotometer N60	Intas
Pipettes	Eppendorf
Power supply	BioRad
QIAxcel Advanced System	Qiagen
Scale	Ohaus
Special accuracy weighing device	Mettler Toledo
Shaver	Moser
STP120 spin tissue processor	Thermo Fisher Scientific
Stereomicroscope	Leica
Table centrifuge (5417R)	Eppendorf
Thermocycler	Thermo Fisher Scientific
Vortex	Neolab
Water bath	Julabo

4.1.11 Software

Table 15: Softwares

Software	Provider
FACSDiva	BD Biosciences
Fiji	ImageJ platform
FlowJo (v10.0.7)	BD Biosciences
Gene Set Enrichment Analysis	Broad Institute
Genepattern	Broad Institute
Graph Pad Prism (v6.0; v8.0)	Graph Pad
ImageQuant TL	GE Healthcare
Light Cycler 480 software	Roche
Molecular Signature Database	Broad Institute
R version 4.0.5	r-project.org
Rstudio Desktop	Rstudio
ZEN black	Zeiss
ZEN blue	Zeiss

4.1.12 Solutions

Table 16: Solutions and buffers

Buffer	Formulation	
Ammonium chloride potassium buffer	150 mM	NH_4Cl
(RBC lysis buffer)	10 M	$KHCO_3$
	100 mM	Na_2EDTA
		adjust pH 7.2-7.4
FACS buffer	5 % (v/v)	Fetal calf serum in PBS
Phosphate buffered saline (PBS)	1.34 M	NaCl
	27 mM	KCl
	200 mM	Na_2HPO_4
	4.7 mM	KH_2HPO_4
		adjust pH 7.4
RNA lysis buffer	0.1% (v/v)	Triton X-100
(SMART-Seq2)	1 U/µl	RNase inhibitor
	2 µM	Oligo-dT primer
	5 µM	dNTPs
		in NF-H_2O
Tris-Buffered Saline Tween-20	10 mM	Tris/HCl, pH 7.5
(TBS-T)	100 mM	NaCl
	0.1 %	Tween-20
Tris-Borate-EDTA buffer	89 mM	Tris-HCL pH 7.5
(TBE)	89 mM	NaCl
	1 mM	Tween-20
Zink fixative	3 mM	$Ca(C_2H_3O_2)2$
	2.2 mM	$Zn(C_2H_3O_2)2$
	3.6 mM	$ZnCl_2$
	0.1 M	Tris-HCl (pH 7.4)

4.1.13 Gene lists

Table 17: Gene lists for defining pathways and cell identities

EMT genes			Wnt genes	Biosyn-thesis genes	Angio-kine genes	Cycling EC marker	Large vessel EC marker	aCap marker	gCap marker
Abi3bp	Csf1	Sgcb	Apc	Glod5	Cxcl10	Hmgb2	Bmx	Ednrb	Plvap
Acta2	Csf1r	Sgcd	Apc2	Rpl18	Lrg1	Cdk1	Vwf	Alpl	Ptprb
Adam12	Csgalnact2	Sgcg	Axin1	Rpl32	Angpt2	Nusap1	Plac8	Tbx2	Cd93
Anpep	Cysltr1	Slc6a8	Axin2	Rps28	Slit3	Ube2c	Prss23	Adamtsl5	Kit
Aplp1	Dbn1	Slit2	Btrc	Upp1	Ccl5	Birc5	Apoe	Meox1	Tek
Areg	Ddr2	Slit3	Cacybp	Depp1		Tpx2	Ltbp4	Fibin	Gpr182
Asp1	Dnm1	Snai2	Camk2a	Col18a1		Top2a	Bgn	Prdm1	Ehd1
Basp1	Dok1	Sntb1	Camk2b	Col4a2		Ndc80	Fbln5	Gpx3	Sema3g
Bdnf	Ehbp1l1	Sparc	Camk2d	Ube2c		Cks2	Car8	Enho	Jam2
Bgn	Eno3	Spock1	Camk2g	Scgb3a1		Nuf2	Cytl1	Apln	Itga6
Bmp1	Epb41l2	Spp1	Ccnd1			Cks1b	Nr2f2	Cdkn2b	Aplnr
Cadm1	F13a1	Tagln	Ccnd2			Mki67	Hey1	Itgb5	Edn1
Cald1	Fam167b	Tfpi2	Ccnd3			Tmpo			Wfdc1
Calu	Fcgr2b	Tgfb1	Cer1			Cenpf			
Cap2	Fcgrt	Tgfbi	Chd8			Tacc3			
Capg	Fcrlb	Tgfbr3	Chp1			Pimreg			
Ccn1	Fkbp7	Tgm2	Chp2			Smc4			
Ccn2	Fkbp9	Thbs1	Crebbp			Ccnb2			
Cd44	Flnc	Thbs2	Csnk1a1			Ckap2l			
Cd59a	Folr2	Thy1	Csnk1e			Ckap2			
Cdh11	Fxyd5	Timp1	Csnk2a1			Aurkb			
Cdh2	Gamt	Timp3	Csnk2a2			Bub1			
Cdh6	Gnb4	Tnc	Csnk2b			Kif11			
Col11a1	Gpr34	Tnfaip3	Ctbp1			Anp32e			
Col12a1	Gpr85	Tnfrsf11b	Ctbp2			Tubb4b			
Col16a1	Gzmb	Tnfrsf12a	Ctnnb1			Gtse1			
Col1a1	Hhex	Tpm1	Ctnnbip1			Kif20b			
Col1a2	Hlx	Tpm2	Cul1			Hjurp			
Col3a1	Hspg2	Tpm4	Cxxc4			Cdca3			
Col4a1	Htra3	Vcam1	Daam1			Jpt1			
Col4a2	Ikbip	Vcan	Daam2			Cdc20			
Col5a1	Il18r1	Vegfa	Dkk1			Ttk			
Col5a2	Itgb1bp1	Vegfc	Dkk2			Cdc25c			
Col5a3	Jdp2	Vim	Dkk4			Rangap1			
Col6a2	Lamb1	Wdhd1	Dvl1			Ncapd2			
Col6a3	Loxl3	Wipf1	Dvl2			Dlgap5			
Col7a1	Lpar1	Wnt5a	Dvl3			Cdca2			
Col8a2	Lsp1	Adgra2	Ep300			Cdca8			

EMT genes			Wnt genes	Biosyn-thesis genes	Angio-kine genes	Cycling EC marker	Large vessel EC marker	aCap marker	gCap marker
Colgalt1	Ltc4s	Adprh	Fbxw11			Ect2			
Comp	Marveld1	Angptl2	Fosl1			Kif23			
Copa	Mcub	Ankrd1	Frat1			Hmmr			
Crlf1	Medag	Aox1	Frat2			Aurka			
Cthrc1	Mras	Ap1s2	Fzd1			Psrc1			
Cxcl1	Mrc1	Apbb1	Fzd10			Anln			
Cxcl12	Mrc2	Apbb2	Fzd2			Lbr			
Cxcl5	Mxra8	Arhgef40	Fzd3			Ckap5			
Dab2	Naaa	Arl6ip5	Fzd4			Cenpe			
Dcn	Nek9	Axl	Fzd5			Ctcf			
Dkk1	Nfatc1	B3gnt9	Fzd6			Nek2			
Dpysl3	Nr2f1	C1qtnf6	Fzd7			G2e3			
Dst	Nrp2	Ccdc102a	Fzd8			Gas2l3			
Ecm1	Nrros	Ccl8	Fzd9			Cbx5			
Ecm2	Olfm1	Ccr2	Gsk3b			Cenpa			
Edil3	Osr1	Cdh13	Jun						
Efemp2	Otud7b	Celf4	Lef1						
Eln	Pdgfra	Cfh	Lrp5						
Emp3	Phka1	Cfl2	Lrp6						
Eno2	Phldb1	Cfp	Map3k7						
Fap	Pkd1	Chrna1	Mapk10						
Fas	Pla2g15	Clec4a2	Mapk8						
Fbln1	Plat	Col6a1	Mapk9						
Fbln2	Plekha3	Zeb2	Mmp7						
Fbln5	Plxnd1	Olfml3	Myc						
Fbn1	Pofut2	Acvrl1	Nfat5						
Fbn2	Prrx2	Cmtm3	Nfatc1						
Fermt2	Rap1b	Gpr124	Nfatc2						
Fgf2	Rgs18	Lama4	Nfatc3						
Flna	Ripor1	Dact1	Nfatc4						
Fmod	Rnf157	Glt8d2	Nkd1						
Fn1	Rrad	Znf469	Nkd2						
Foxc2	S100a4	Klf6	Nlk						
Fstl1	Sacs	Klf10	Plcb1						
Fstl3	Scara3	Klf11	Plcb2						
Fuca1	Sec23a	Klf4	Plcb3						
Fzd8	Selenon	Klf5	Plcb4						
Gadd45a	Sema7a	Prrx1	Porcn						
Gadd45b	Sh3glb1	Prss2	Ppard						
Gas1	Snx20	Pthlh	Ppp2ca						
Gem	Snx6	Ptx3	Ppp2cb						

EMT genes			Wnt genes	Biosyn-thesis genes	Angio-kine genes	Cycling EC marker	Large vessel EC marker	aCap marker	gCap marker
Gja1	Snx9	Pvr	Ppp2r1a						
Glipr1	Spi1	Qsox1	Ppp2r1b						
Gpc1	Sptbn1	Rgs4	Ppp2r5a						
Gpx7	St3gal2	Rhob	Ppp2r5b						
Grem1	St8sia4	Sat1	Ppp2r5c						
Htra1	Stk17b	Scg2	Ppp2r5d						
Id2	Tgfbr2	Sdc1	Ppp2r5e						
Igfbp2	Timp2	Sdc4	Ppp3ca						
Igfbp3	Tjap1	Serpine1	Ppp3cb						
Igfbp4	Traf1	Serpine2	Ppp3cc						
Il15	Tspan4	Serpinh1	Ppp3r1						
Il6	Ttyh2	Sfrp1	Ppp3r2						
In(11)2Dn-d	Vsig4	Sfrp4	Prickle1						
Inhba	Was	Prrx1	Prickle2						
Itga2	Wnk1	Prss2	Prkaca						
Itga5	Zeb1	Pthlh	Prkacb						
Itgav	Zfpm2	Ptx3	Prkca						
Itgb1	Anln	Pvr	Prkcb						
Itgb3	Aplp2		Prkcg						
Itgb5	Cd63		Prkx						
Jun	Clic4		Psen1						
Lama1	Ctsb		Rac1						
Lama2	Cx3cr1		Rac2						
Lama3	Dsg2		Rac3						
Lamc1	Ednrb		Rbx1						
Lamc2	Emp1		Rhoa						
Lgals1	Enc1		Rock1						
Lox	Fgg		Rock2						
Loxl1	Fzd1		Ruvbl1						
Loxl2	Hmmr		Senp2						
Lrp1	L1cam		Sfrp1						
Lrrc15	Mfap1a		Sfrp2						
Lum	Pfn1		Sfrp4						
Magee1	Prkca		Sfrp5						
Matn2	Rab1a		Skp1						
Matn3	Ran		Smad2						
Mcm7	Rraga		Smad3						
Mest	Sdcbp		Smad4						
Mfap5	Selenop		Sox17						
Mgp	Smarca1		Tbl1x						
Mmp13	Spa17		Tbl1xr1						

EMT genes		Wnt genes	Biosyn-thesis genes	Angio-kine genes	Cycling EC marker	Large vessel EC marker	aCap marker	gCap marker
Mmp14	Tuba1a	Tcf7						
Mmp2	Tuba4a	Tcf7l1						
Mmp3	Tubb3	Tcf7l2						
Msx1	Arhgef18	Trp53inp2						
Myl9	Cgn	Vangl1						
Mylk	F11r	Vangl2						
Nid2	Fkbp1a	Wif1						
Nnmt	Pard3	Wnt1						
Notch2	Pard6a	Wnt10a						
Nt5e	Prkcz	Wnt10b						
Ntm	Rhoa	Wnt11						
Oxtr	Rps27a	Wnt16						
P3h1	Smurf1	Wnt2						
Pcolce	Tgfbr1	Wnt2b						
Pcolce2	Uba52	Wnt3						
Pdgfrb	Ubb	Wnt3a						
Pdlim4	Ubc	Wnt4						
Pfn2	Anxa6	Wnt5a						
Plaur	Lix1l	Wnt5b						
Plod1	Syt11	Wnt6						
Plod2	Gnai2	Wnt7a						
Plod3	Fyn	Wnt7b						
Pmepa1	Atp10a	Wnt8a						
Pmp22	Cnrip1	Wnt8b						
Postn	Emilin1	Wnt9a						
Ppib	Olfml2b	Wnt9b						

4.2 Methods

4.2.1 Animal studies

4.2.1.1 Animal husbandry

Female NOD-SCID and BALB/c mice were acquired from Janvier Labs. B6 *PDGFB-iCreERT2-IRES-EGFP* x *Wls* floxed mice were bred in barrier animal facilities of the German Cancer Research Centre. All animal work was performed following German national guidelines on animal welfare and the regulations of the regional council Karlsruhe under permit numbers G-164/16, G-107/18, DKFZ305, and DKFZ370. Mice were housed in sterile cages, maintained in a temperature-controlled room, and fed autoclaved water, and food *ad libitum*. All animals were monitored daily for signs of disease and ear punches were used for genotyping the mice. Imported mice were allowed to acclimatize for a minimum of seven days before each experiment. For all experiments, 8-12 weeks-old mice were used and euthanized via rapid cervical dislocation of the spinal cord at the experimental endpoint.

4.2.1.2 Experimental metastasis model

For experimental metastasis, tumor cells were resuspended in 200 µl PBS and injected into the tail vein of mice. For transcriptomic and epigenomic screening experiments female Balb/c mice were injected twice with $1x10^6$ tumor cells (4T1-GFP, niche-labeling 4T1-GFP, niche-labeling D2.0R-GFP) with a 30-minute break between injections (Fig. 6, 13, 19).

For pharmacological treatment studies, female Balb/c mice were injected once with $1x10^6$ 4T1-GFP cells (Fig. 10, 16-18) for day 1.5 and day 3.5 timepoints, with $1x10^5$ cells for the one-week timepoint and with $5x10^4$ cells the two-week timepoint. To adhere to the 3R principles, the data presented in Fig. 9i and Fig. 16g utilized the same control animals. As such, all animals and cells were treated with vehicle control or the respective pharmacological agent.

For genetic knockout experiments, male and female B6 B6 *PDGFB-iCreERT2-IRES-EGFP* x *Wls* floxed mice were injected with $2x10^5$ E0771-GFP or B16F10, respectively (Fig. 11).

4.2.1.3 Spontaneous metastasis model

To model spontaneous dissemination, $1x10^6$ 4T1-GFP cells in 100 µl PBS were injected into the inguinal mammary fat pad of female NOD-SCID mice. Tumor volumes were assessed by caliper measurements (tumor volume = ½ x length x width x width). Upon reaching tumor sizes of 100 mm^3, mice were treated daily with LGK974 for 5 days with subsequent resection of the primary tumor. LGK974 treatment continued for 2 days post-resection and mice were left to develop metastases for 2 weeks.

4.2.2 *In vivo* treatments

4.2.2.1 Tumor resection

Tumor resection surgeries were performed under anesthesia, induced by intraperitoneal administration of Ketamine (120 mg/kg) and Xylazine (15 mg/kg) in isotonic 0.9 % NaCl. Anesthetized mice were placed on a heat mat and eyes were protected from drying using bepanthen cream. Whole tumor-bearing mammary fat pads were resected. Large tumor vessels were electrocauterized to achieve hemostasis and prevent blood loss. Surgery wounds were sutured using 5-0 sutures for the peritoneum (continuous pattern) and 4-0 sutures for the skin (interrupted pattern).

4.2.2.2 Tamoxifen

EC-specific depletion of Wnt ligands was achieved using B6 *Cdh5-CreERT2* x *Wls* floxed mice. Genetic recombination was initiated by intraperitoneal delivery of 2 mg tamoxifen (Sigma Aldrich) dissolved in 50 µl corn oil with 5% ethanol. Both Cre+ and Cre- littermates received 5 consecutive daily injections and were subjected to a one-week washout period before the start of the experiment.

4.2.2.3 LGK974

Pharmacological systemic depletion of WNT was achieved by daily oral gavage of 10 mg/kg body weight LGK974 resuspended in sterile-filtered 0.5% methylcellulose (Sigma-Aldrich), 0.5% TWEEN 80 (Sigma-Aldrich) in PBS as described previously [211]. Control animals received equal volumes of the vehicle only.

4.2.2.4 LPS

To account for general inflammatory signatures in lung EC in the niche-labeling experiment (Fig. 13), mice were injected with 1 mg/kg LPS in 0.9% NaCl intraperitoneally 24 h prior to euthanasia.

4.2.2.5 Anti-H2-Kd antibody

To stain intravascular cells, 5 µg of fluorescently labeled anti-H2-Kd antibody in 50 µl PBS was injected intravenously into mice 2 min prior to euthanasia.

4.2.3 Tissue processing

4.2.3.1 Primary tumor

Resected primary tumors were rinsed in PBS, split into two halves, and fixed in formalin-free Zn-buffer overnight. After fixation, one-half of the tumor was placed in a cryomold and embedded in TissueTek Optimum Cutting Temperature (O.C.T.) compound, frozen on dry ice, and stored for further use at -80°C. The other half of the tumor was embedded in paraffin. For this purpose,

samples were washed with VE-water and further processed with the spin tissue processor STP120. Automated steps included incubations in a graded ethanol series (70-85-96 %), isopropanol, xylol, and paraffin. Afterward, samples were manually embedded in paraffin blocks.

4.2.3.2 Lungs

4.2.3.2.1 Macroscopic evaluation of metastatic burden

After euthanizing the mice, the lungs were resected and collected in ice-cold PBS. For B16F10 experiments, metastatic foci were manually counted using a stereomicroscope (Leica). For each sample, two independent and blinded counts were performed. For analysis, the average count per tissue was used. For primary tumor experiments and E0771-GFP experiments, lungs were excised and placed in ice-cold PBS. Metastatic lungs were weighed and lung weight-to-body weight ratios were determined for each mouse.

4.2.3.2.2 Single-cell suspensions

For primary tumor experiments, E0771-GFP, and pharmacological treatment experiments, metastatic burden was assessed using flow cytometry. Metastatic lungs were excised and rinsed in ice-cold PBS. Isolated lungs were minced on ice using curved serrated scissors. The minced tissue was resuspended in DMEM supplemented with Liberase Thermolysin Medium enzyme mix (0.2 mg/ml, Roche) and DNAse I (0.2mg/ml, Sigma Aldrich) and incubated at 37°C first for 15 min and then again for 12 minutes. After each incubation, minced tissues were passed through 18G cannula syringes 30 times. After the second incubation, digested tissues were passed through a 100 µm cell strainer to remove tissue debris and cell clumps. The following steps were all performed on ice and in pre-cooled centrifuges. The digestion reaction was quenched by adding ice-cold FCS and samples were centrifuged at 4°C and 400 *g* for 4 min. Erythrocytes were lysed by resuspending the cell pellet in pre-chilled 1x ammonium chloride potassium (ACK) buffer and incubating the mix for 5 min on ice. The reaction was quenched by adding ice-cold PBS, followed by centrifugation. Single-cell suspensions were then further processed for flow cytometry.

4.2.4 Flow cytometry and cell sorting

4.2.4.1 Sample preparation

Whole lung single cell suspensions were resuspended in 200 µl iced PBS and passed through a 40 µm cell strainer. The single cell suspension was preincubated with anti-mouse CD16/CD32 Fc block (1:100, Thermo Fisher Scientific) for 15 min in FACS buffer (PBS supplemented with 5% [v/v] FCS) and, subsequently, with the appropriate antibody-mix for 20 min on ice.

4.2.4.2 Gating strategy

For cell sorting and flow cytometry analysis, dead cells were excluded by staining with FxCycle™ Violet Stain (1:1000, Thermo Fisher Scientific) or Fixable Viability Dye eFluor™ 780 (1:1000, Thermo Fisher Scientific) according to the manufacturer's instructions. All samples were gated on intact cells followed by the exclusion of cell doublets, dead cells, and CD45+, LYVE1+, PDPN+, TER119+ cells using the BD FACS Diva Software (BD Biosciences). Tumor cells and endothelial cells were discriminated by reporter gene expression (GFP or mCherry) or marker gene expression (CD31), respectively. For flow cytometry, samples were recorded on the BD LSR Fortessa or BD FACSCanto II cell analyzer (both BD Biosciences), and flow data were analyzed with FlowJo software (BD Biosciences, v10). Cells were sorted using a BD Biosciences Aria cell sorting platform (BD Biosciences) with 100 µm nozzle.

4.2.4.3 Analysis

Tumor cell frequencies were calculated either as a percentage of sample-matched lung endothelial cells (relative tumor cell number) or as total tumor cell counts per mg lung tissue or per lung, respectively, using CountBright™ Absolute Counting Beads according to the manufacturer's protocol.

4.2.5 Cell culture

4.2.5.1 Maintenance

4T1-GFP, 4T1-mCherry, D2.0R, and E0771-GFP cells were gifts from the laboratories of Dr. Robert Weinberg (Whitehead Institute, Cambridge, MA), Dr. Jonathan Sleeman (Heidelberg University, Mannheim, Germany) and Dr. Kairbaan Hodivala-Dilke (Barts Cancer Institute, London, England), respectively. B16F10 cells were purchased from ATCC. All cells were maintained at 37°C and 5% CO2 in high humidity and cultured in high glucose DMEM (Gibco) supplemented with 10% (vol/vol) FCS and 100 U/mL penicillin/streptomycin (Sigma Aldrich). Cells were checked regularly for mycoplasma contamination by PCR and cell identity was confirmed by cell morphology.

4.2.5.2 Subculture

Cells were subcultured upon reaching 80-90% confluency by trypsin-EDTA (Sigma Aldrich) treatment. Dishes were rinsed with PBS and an appropriate volume of trypsin-EDTA (1 mL per ⌀ 10 cm cell culture dish / 3 mL per ⌀ 15 cm cell culture dish) was added. Cells were incubated for 3-5 min (D2.0R, E0771 and B16F10) or for 7-10 min (4T1) at 37°C and detached cells were resuspended in pre-warmed medium and split in 1:5 ratio.

4.2.5.3 Cryopreservation

Cryostocks were prepared for long-term storage of cells and tumor fragments. Cells were resuspended in cell type-specific media with 10 % DMSO and 10 % FCS. Cell suspensions (1 ml) were transferred to cryotubes and then slowly frozen to -80 °C in an isopropanol containing freezing box (Mr. Frosty Freezing Container, Thermo Fisher Scientific) over night, and subsequently transferred to liquid nitrogen tanks for long-term storage. For the thawing of cells, cryotubes were placed directly in a pre-heated water bath at 37 °C until completely thawed. Thawed cells were seeded without washing into a 10 cm or 15 cm cell culture dish containing the appropriate volume of culture medium, respectively.

4.2.5.4 Lentiviral transduction

D2.0R-GFP cells were generated by lentiviral transduction with TurboGFP reporter (Dharmacon, RHS4346). Niche-labeling cells were generated by lentiviral transduction of 4T1-GFP and D2.0R-GFP cells. Niche-labeling lentivirus was provided by the laboratory of Dr. Ilaria Malanchi (Francis Crick Institute, London, England).

4.2.5.5 *In vitro* treatments

Cell media were supplemented with 20 mM SKL2001 (Selleckchem) in DMSO (Sigma Aldrich), 3 mM CHIR99021 (Selleckchem) in DMSO, or 1 µM decitabine (Sigma Aldrich) in PBS. Cells were treated overnight (~17 h) for pulse treatments (SKL2001, CHIR99021, decitabine) or 2 weeks with daily media changes for reprogramming (SKL2001, CHIR99021). For all treatments vehicle controls (solvent only) of equal volume and with daily media changes were included.

4.2.5.6 Cell counting

Cells were detached from plates, washed, and resuspended in an appropriate volume of PBS. 10 µL of the cell suspension was withdrawn and mixed with 10 µL trypan blue. 10 µL of the cell-dye mix was loaded onto a counting chamber and counted in an automated cell counting machine (Countess, Thermo Fisher Scientific) according to the manufacturer's instructions. Cell solutions with desired concentration were prepared for tumor cell injection or for seeding in cell culture dishes.

4.2.5.7 CellTracer staining

Tumor cells were detached from the culture dish, counted, and washed with PBS. CellTracer dye (Thermo Fisher Scientific) was reconstituted according to the manufacturer's instruction and added to the tumor cell suspension. Cell-dye mix was incubated for 20 min protected from light at 37°C. After incubation, cells were pelleted and resuspended in 5 mL pre-warmed cell culture medium to

remove excess dye. Cells were washed twice in PBS, counted and diluted to the desired cell concentration. After injections, leftover cells were recorded with flow cytometer to setup the instrument and verify the staining.

4.2.6 Molecular biology

4.2.6.1 PCR

Ear punches were lysed in 100 µl Direct PCR Lysis Reagent with 10 µg Proteinase K for at 55°C overnight. Digestion was stopped by heat inactivation at 95°C for 20 min. Tissue lysates were centrifuged to pellet cell and tissue debris and the supernatant was used for genotyping. Remaining lysates were stored at 4°C for days and at -20 °C for long-term storage.

For mycoplasma detection, 1 ml cell culture medium was centrifuged to remove cell debris and 2 µl of supernatant was directly used for detection PCR. PCRs for genotyping and mycoplasma detection were performed using REDTaq ReadyMix (Thermo Fisher Scientific) or Taq polymerase kit (Qiagen) with appropriate primers according to the manufacturer's instructions. Specific cycle specifications for each PCR product were set in a thermocycler (Applied Biosystems). PCR reactions were analyzed by 1-2 % agarose gel electrophoresis (Mycoplasma detection) or with the automated QIAxcel Advanced system according to the manufacturer's protocol (genotyping).

4.2.6.2 Agarose gel electrophoresis

Agarose was dissolved in 1x TBE buffer at a concentration of 1-2 % [w/v] and heated in a microwave for 30 sec at maximum power. The agarose solution was allowed to cool down and 5 µl ethidium bromide was added to a 100 ml gel before polymerization occurred. Gels were cast and genotyping reactions and 7 µl of the O'Generuler 100 bp Plus DNA ladder were loaded into individual pockets of the gel. DNA fragments were separated by size at 140 V for 45 min and DNA bands were detected with a UV transluminator. Fragment length was estimated in relation to the DNA ladder.

Table 18: Mycoplasma detection PCR

PCR mix (Quiagen)		qPCR program		
ddH_2O	6.8 µl	Step	Temperature	Time
Q-solution	2.6 µl	1	95°C	5 sec
Buffer 10x	1.25 µl	2	95°C	30 sec
$MgCl_2$	0.5 µl	3	58°C	30 sec
dNTP (2.5 mM)	0.25 µl	4	72°C	1 min
MGSO (10 µM)	0.25 µl	Go to step 2: x40		
GPO (10 µM)	0.25 µl	5	72°C	10 min
Taq (5 U/µl)	0.1 µl	6	4°C	∞
DNA	2.0 µl			
Mycoplasma contamination: 270 bp				

Table 19: Genotyping of Cre-ERT2

PCR mix (REDTaq ReadyMix)		qPCR program		
ddH_2O	7 µl	Step	Temperature	Time
REDTaq ReadyMix	10 µl	1	95°C	2 min
Cre-Fwd	1 µl	2	95°C	30 sec
Cre-Rev	1 µl	3	58°C	45 sec
Actb-Fwd	1 µl	4	72°C	2 min
Actb-Rev	1 µl	Go to step 2: x35		
DNA	1 µl	5	72°C	2 min
		6	4°C	∞
Transgene: 400 bp; internal control: 300 bp				

Table 20: Genotyping of Wls-floxed

PCR mix (REDTaq ReadyMix)		qPCR program		
ddH_2O	9 µl	Step	Temperature	Time
REDTaq ReadyMix	10 µl	1	95°C	5 min
Wls-Fwd	1 µl	2	95°C	30 sec
Wls-Rev	1 µl	3	50°C	30 sec
DNA	1 µl	4	72°C	1 min
		Go to step 2: x44		
		5	72°C	10 min
		6	4°C	∞
Floxed allele: 210 bp; wildtype allele: 340 bp				

4.2.6.3 RNA isolation

RNA of FACS-sorted mouse cells for sequencing experiments was isolated using the Arcturus PicoPure RNA Isolation Kit (Thermo Fisher Scientific) following the manufacturer's instructions. RNA was typically eluted in 11 µl RNase-free H_2O.

RNA of cultured cells was extracted using the GenElute Mammalian Total RNA Purification Kit (Merck). For this, the culture medium was aspirated and 400 µl of RNA lysis buffer was added directly to the cells. Cells were incubated for 15 min and lysis buffer containing extracted RNA was processed according to the manufacturer's instructions. Purified RNA was eluted in 30 µl RNase free H_2O. For sequencing experiments, RNA concentrations were measured on a Qubit 3.0 using the RNA HS kit according to the manufacturer's protocol. For gene expression analyses using quantitative PCR, purified RNA concentrations were measured using NanoPhotometer N60. Purified RNA was either immediately processed or stored at -80°C until further use.

4.2.6.4 Reverse Transcription

Isolated RNA was reverse transcribed using the QuantiTect Reverse Transcription Kit (Qiagen) following the manufacturer's protocol. 1000 ng of RNA/sample were transcribed. In case of insufficient sample quantity, RNA was normalized to the least abundant sample to ensure minimal technical batch effects. cDNA was stored at -20°C up until further use.

4.2.6.5 Quantitative PCR

Gene expression analysis was performed by quantitative PCR using TaqMan reactions (Thermo Fisher Scientific) and Lightcycler 480 (Roche). Each sample was analyzed in technical triplicates. Gene expression levels were assessed using the Ct-method and normalized to the expression of Actb, resulting in ΔC_t-values. Relative gene expression was calculated by normalizing ΔC_t-values of individual samples to the average control ΔC_t-value, resulting in $\Delta\Delta C_t$-values. Relative fold changes to control were then calculated as $2^{-\Delta\Delta Ct}$ 212.

Table 21: Reaction setup for quantitative PCR

qPCR reaction mix		qPCR program		
	1 reaction	Step	Temperature	Time
cDNA	4 µl	1. Pre-denaturation	95°C	30 sec
TaqMan Fast Advanced Master Mix	5 µl	2. Denaturation	95°C	2 sec
TaqMan gene expression assay	0.5 µl	3. Amplification	60°C	20 sec
Nuclease-free H_2O	0.5 µl	Go to step 2: x45		

4.2.7 Histology

4.2.7.1 Tissue staining

Paraffin-embedded primary tumors were cut into 7 µm sections using the rotary microtome HM355S. Sections were deparaffinized and rehydrated and antigen retrieval was performed by incubation with Proteinase K (20 µg/ml, Gerbu Biotechnik) for 5 min at 37°C. Tissues were blocked in 10% ready-to-use goat serum (Zymed) for 1 hour at room temperature, followed by overnight incubation with rat anti-CD31 (1:100, BD Bioscience) and rabbit anti-Desmin (1:100, Abcam) antibodies diluted in blocking buffer at 4 °C. After three washes in TBS-T, slides were stained with anti-rat Alexa647 and anti-rabbit Alexa546 antibody at room temperature for 1 hr. Cell nuclei were counterstained with 1:2000 Hoechst 33342 (Sigma-Aldrich) and sections were mounted with DAKO mounting medium (Agilent).

4.2.7.2 Image acquisition and analysis

Images were acquired as whole-area tile scans using an Axio Scan.Z1 slide scanner (Zeiss). Image analysis was performed using Fiji software (ImageJ, 1.53q). After region-of-interest (ROI) selection, CD31, Desmin, and DAPI channels were binarized using manual thresholding. For the vessel area, the percentage of CD31+ area within the ROI was calculated. For the vessel coverage, the CD31 channel was masked and the Desmin overlap with CD31 was calculated. CD31+/Desmin+ double-positive

vessel were considered covered and coverage was calculated as the ratio of covered/uncovered vessels.

4.2.8 Sequencing experiments

4.2.8.1 Single-cell RNA-sequencing

ScRNAseq on tumor cell subpopulations and endothelial cells was performed using a modified SMART-Seq2 protocol [185]. In brief, single cells were sorted directly into 96 well plates containing 1 µl of lysis buffer per well, centrifuged, and snap-frozen on dry ice. For CD45- PDPN- LYVE- TER119- CD31+ ECs, four plates (384 cells) were sorted for each of the 3 biological replicates on day 1.5 and day 3.5 (total of 1152 cells per timepoint). Day 0 control samples were split and three plates (288 cells) were sorted for 2 biological replicates on day 1.5, as well as on day 3.5 (total of 1152 cells), respectively, to account for technical batch effects. For TCs, 1 plate of matched intravascular and extravascular fractions (each 96 cells) was sorted for each of the 4 biological replicates (total of 384 cells per fraction) on day 1.5. Similarly, 1 plate of matched dormant and proliferative fractions was sorted for each of the 4 biological replicates on day 3.5. Frozen plates were thawed on ice and oligo-dT-primers were annealed at 70°C for 3 min. 1.3 µl of reverse transcription mix with template-switching oligo was added to each well and isolated mRNA was transcribed to full-length cDNA. Full-length cDNA was then amplified by adding 2.4 µl of PCR mastermix to each well. Due to their low RNA-content, EC cDNA was amplified using 22 cycles, while TC cDNA was amplified with 18 cycles. Amplified cDNA was purified using AMPure XP beads (Beckman Coulter) and random wells were selected for quality control using 2100 Bioanalyzer (Agilent) and Qubit fluorometer (Thermo Fisher Scientific). DNA concentration for each well was measured using Quant-iT^{TM} high sensitivity kit (Thermo Fisher Scientific) and concentrations were manually adjusted to 0.1 - 0.3 ng/µl. Tagmentation was performed using the Nextera XT DNA library preparation kit (Illumina) and a mosquito liquid handler (SPT Labtech). For this purpose, 1.2 µl of Nextera XT – TD buffer mix was added to each well of a 384 well plate with 0.4 µl of cDNA. For ECs, 96 well plates from the individual biological replicates were pooled into one 384 well plate, whereas TC replicates were pooled according to sort gates. After tagmentation, customized i5 and i7 index primers were added, resulting in unique labeling of each well in the 384 well plate and tagmented cDNA was amplified using 14 PCR cycles. All uniquely labeled wells from each plate were pooled and multiplexed libraries were purified and quality controlled using TapeStation (Agilent) and Qubit fluorometer (Thermo Fisher Scientific), resulting in one multiplex per biological replicate for ECs and one multiplex per FACS-sorted TC fraction. Multiplexes were then sequenced on individual lanes on a HiSeq2000 (Illumina) using V4 50 cycle single read kit generating approximately 500.000 reads per cell.

4.2.8.2 Bulk RNA-sequencing of labeled niche EC

For the niche-labeling experiment 50.000 unlabelled lung ECs and sample-matched total labeled ECs were directly sorted as described above into RNase-free 1.5 ml microcentrifuge tubes containing 100 µl lysis buffer and immediately snap-frozen on dry ice. For each condition, 6 biological replicates were included. For control samples (LPS control and PBS control) 50.000 lung ECs were sorted. Snap-frozen RNA was extracted using Arcturus PicoPure RNA Isolation Kit (Thermo Fisher Scientific) according to manufacturer instructions. RNA was quality controlled by Qubit fluorometer (Thermo Fisher Scientific) and 2100 Bioanalyzer (Agilent). Samples with RNA integrity number (RIN)-values below 8 were discarded. RNA was transcribed to full-length cDNA using the SMART-Seq2 protocol [185] and RNA-sequencing libraries were generated using the NEBNext® Ultra™ II FS DNA library preparation kit (New England Biolabs) according to the manufacturer's protocol with DNA input below 100 ng. Libraries were indexed using unique i5 and i7 combinations and equimolarly pooled into one multiplex. The multiplex was sequenced over two lanes on a NovaSeq 6000 using the S1 100 cycle paired-end kit generating approximately $35x10^6$ reads per sample.

4.2.8.3 Whole genome bisulfite sequencing

For whole genome bisulfite sequencing (WGBS) analysis of dormant and proliferative TC, lungs of 6 mice were pooled into one sample and 200.000 proliferative TCs, as well as total dormant TCs were sorted from 4 pools. Sorted samples were centrifuged and cell pellets were snap-frozen on dry ice. Genomic DNA was extracted using the NucleoSpin tissue mini kit for DNA from cells and tissue (Macherey-Nagel). DNA integrity was assessed by TapeStation (Agilent) and samples with DNA integrity number (DIN)-values below 7 were discarded. WGBS libraries were prepared using the xGen™ Methyl-Seq DNA Library Prep Kit (IDT) with partially modified steps in bead clean-up/size selection. Briefly, 200ng genomic DNA was fragmented to 700 – 1000 bp using Covaris ultrasonicator (Covaris, Inc.) and quality checked using TapeStation (Agilent Technologies). Fragmented DNA samples were treated with bisulfite using the EpiTect Bisulfite Kit (Qiagen) following the instructions in the Illumina WGBS for Methylation Analysis Guide (Part # 15021861 Rev. B). After bisulfite conversion adapters were attached to 3`ends of single-stranded DNA fragments which are then extended to generate complementary uracil-free molecules as described in manufactures protocol. The double-stranded DNA fragments were subsequently cleaned up using 1.6x AMPure XP beads (Beckman Coulter) and size selected with a bead ratio of 0.6x and 0.2x, followed by ligation of truncated adapter 2 to uracil-free strand. The adapter-ligated libraries were enriched and indexed using 6 cycles of PCR and purified using magnetic beads according to the protocol. Amplified libraries were quality-checked using Qubit fluorometer (Thermo Fisher Scientific) and TapeStation (Agilent).

Libraries were pooled equimolarly into one multiplex and sequenced over two lanes on a NovaSeq 6000 using the S1 150 cycle paired-end kit enabling an average genomic coverage of >15.

4.2.9 Data analysis

4.2.9.1 Niche-labeling RNA-Sequencing analysis

Raw sequencing data were demultiplexed and FASTQ files were generated using bcl2fastq software (Illumina, v2.20.0.422). FASTQ files were mapped to the GRCm38 mouse reference genome using salmon (v0.7.2) [213] and count matrices were constructed with the R package tximport (v1.18.0) [214]. Differential gene expression analysis was performed using DESeq2 (v.1.30.1) [215]. Each condition was tested against each condition and differentially expressed genes were used for gene set enrichment analysis (GSEA). GSEA [216, 217] was performed using the R package clusterProfiler (v3.18.1) [218] or the GSEA java desktop application and the Molecular Signatures Database (MSigDB, v7.4) [193] provided by the Broad Institute.

For the proliferative niche EC gene panel, DEG were filtered for genes that were specifically upregulated in proliferative niche ECs in at least three comparisons ($p < 0.01$ & log2 fold change > 0.5) and were not regulated in non-proliferative niche EC comparisons. For the deconvolution of bulk samples aCap and gCap marker genes were defined using the scRNAseq dataset. Expression coefficients (aCap/gCap) of summed marker genes were calculated for each bulk sample using quasibinomal fitting and normalized to PBS injected control samples. Resulting ratios were exponentiated for plotting.

4.2.9.2 Single-cell RNA-seq analysis

4.2.9.2.1 Pre-processing and normalization

Raw sequencing data were processed as described above. Gene expression was normalized to the mean expression of a housekeeping gene panel (*Actb, Gapdh, Tubb5, Ppia, Ywhaz, B2m, Pgk1, Tbo, Arbp, Gusb, Hprt1*) for each cell, scaled with factor 10.000 and log10 normalized. Normalized count matrices were further analyzed using the R package Seurat (v4.0.1) [219, 220]. Gene counts per cell, read counts per cell, and percentage of mitochondrial transcripts were computed using the respective functions of the Seurat package. For the EC dataset, cells with a percentage of mitochondrial transcripts greater than 5%, along with those with fewer than 1000 genes were excluded. For the TC dataset, only cells with a mitochondrial transcript percentage of less than 5% and more than 2500 genes were kept for further analysis.

4.2.9.2.2 Dimension reduction and clustering

Shared nearest neighbour (SNN)-based clustering and UMAP visualization were performed using the FindClusters and RunUMAP functions within the Seurat package. Each of these were performed based on principal component analysis, which was performed using the RunPCA function of the Seurat package. For the EC dataset dimensional reduction was performed on 10 principal components (PC) and cells were classified based on the scored expression of known lung EC subtype genesets (Table 17). ECs with large vessel gene scores > 1 were considered large vessel ECs. ECs with cycle gene score > 0.5 were considered as cycling ECs. ECs with aCap gene score > 0 and gCap gene score < 0 were considered aerocytes, whereas general capillary ECs were defined as ECs with aCap gene scores < 0 and gCap gene scores > -0.5. For the TC dataset 15 PCs were used for dimension reduction and the resolution parameter was set to 0.5 for the FindClusters function. Clusters were annotated according to FACS gate enrichment. Contaminating cells were removed from the dataset based on expression of immune marker genes (*Ptprc, Itgam, Itgax, Adgre1, Cd3e, Cd19, Cd56*) or stromal cell and vessel mural cell marker genes (*Pdgfrb, Des, Myh11, Col1a2, Pdgfra, Cspg4, Pdpn, Acta2*).

4.2.9.2.3 Cell cycle scoring and differential gene expression

The cell-cycle state was assessed using the gene set and scoring system described previously [221]. Briefly, the S and G_2M scores were calculated based on a list of 43 S phase-specific and 54 G_2 or M phase-specific genes. Cells that originated from the dormant FACS gate and had summed scores of less than -1 were tested against cells from the proliferative gate that had score sums greater than 0. Differentially expressed genes were calculated by Wilcoxon rank sum test using FindMarkers-function in Seurat and used for GSEA as described above.

EMT and Wnt gene sets were compiled from MSigDB and gene scores for each cell were calculated using the AddModuleScore-function in Seurat.

4.2.9.2.4 Trajectory analysis

Trajectory analysis of lung resident TCs was performed using the R package Monocle (v.3 alpha) [222, 223]. The filtered and normalized TC count matrix was subset from the TC Seurat object. Clustering and dimension reduction was performed using default parameters in Monocle3. The trajectory graph was built by setting cells from the intravascular sorting-gate as starting point. Cells were colored according to cluster identities as identified in Seurat. Gene expression of EMT and Wnt gene sets was visualized using the plot_cells function.

4.2.9.2.5 Analysis of TC-EC interactions

Leveraging the biological replicates, TC pseudo-bulks were formed. To this end all counts from cells of a specific FACS gate and biological replicate were summed and differentially expressed genes (DEG) were computed for the experimental timepoints using DESeq2 [215]. DEG were filtered against CellPhoneDB database [187] to retrieve putative ligands and receptors. CellPhoneDB ligands and receptors were further filtered for expression of interaction partners in the day 1.5 EC dataset (for intravascular versus extravascular comparison) or for expression in the day 3.5 EC dataset (for dormant versus proliferative comparison), respectively. Log2 fold changes of TC-expressed ligands or receptors were plotted against each. Receptors or ligands with upregulation in extravasated and dormant TCs were considered trajectory defining, as well as receptors or ligands upregulated in intravascular and proliferative TCs.

4.2.9.2.6 Analysis of publicly available human CTC datasets

Normalized and filtered count matrices were downloaded from provided source data [190] or the gene expression omnibus (GEO) under the accession code GSE109761 [191]. Dimension reduction and visualization were performed in Seurat as described above using default parameters. Gene scores of human orthologues of the EMT and Wnt gene lists were computed as described above.

4.2.9.3 WGBS data analysis

Raw sequencing data were demultiplexed and FASTQ files were generated using bcl2fastq software (Illumina, v2.20.0.422). FASTQ files were trimmed using Trimgalore (v0.6.6) [224] and mapped to the GRCm39 mouse reference genome using Bismark (v0.22.3) [225]. Forward and reverse strands were collapsed and methylation sites were called in Bismark. Differentially methylated regions were determined with the R package bsseq using default parameters (v1.26.0) [226]. For this, biological replicates were summed and methylation fractions for annotated genomic regions between the two conditions were compared. Regulatory elements, promoters and gene bodies were annotated with annotation sheets downloaded from Ensembl database (release 105) [227].

4.2.9.4 Statistical Analysis

Statistical analysis was performed using GraphPad Prism (v6) and R (v4.0.5).

Abbreviations

µg	Microgram
µl	Microliter
ACK	Ammonium chloride potassium
Actb	Beta-Actin
AF	Alexa Fluor
ANGPT	Angopoeitin
APC	Allophycocyanin
ATCC	American type culture collection
BMP	Bone morphogenic protein
Ca^{2+}	Calcium ion
CD	Cluster of differentiation
Cdh5	Vascular endothelial cadherin
CEL	Cell Expression by Linear amplification and Sequencing
CI	Confidence interval
CO_2	Carbon dioxide
C_t	Threshold cycle
CTC	Circulating tumor cell
Ctrl	Control
Cytl1	Cytokine like 1
d	days
dd	Double-distilled
DAPI	4', 6-diamidino-2-phenylindole
DESeq2	Differential expression analysis for sequence count data
DMEM	Dulbecco's modified Eagles's medium
DMSO	Dimethylsulfoxide
DNA	Deoxyribonucleic acid
DNAse	Deoxyribonuclease
dNTP	Deoxynucleoside triphosphate
ds	Double stranded
DTC	Dormant tumor cell
E	Embryonic day
E-Selectin	Endothelial-leukocyte adhesion molecule 1
EC	Endothelial Cell
ECM	Extracellular Matrix
EMP	Erythro-myeloid progenitor
EMT	Epithelial to mesenchyme transition
EPC	Endothelial progenitor cell
FACS	Fluorescence activated cell sorting
FC	Flow Cytometry
FCS	Fetal calf serum
FDR	False discovery rate
FITC	Fluorescein isothiocyanate
fl	Floxed

FSC	Forward scatter
Fwd	Forward
Fzd	Frizzled Class Receptor
g	Gram
G-O-F	Gain of function
GFP	Green fluorescent protein
GO	Gene ontology
GSEA	Gene set enrichment analysis
h	hours
H_2O	Water
HCC	Hepatocellular carcinoma
HGF	Hepatocyte growth factor
HSPC	Hematopoietic stem and progenitor cells
hypo	Hypomethylated
i.p.	Intraperitoneal
i.v.	Intravenous
iECKO	Inducible EC-specific knockout
IF	Immunofluorescence
Ig	Immunoglobulin
IgG	Immunoglobulin G
kg	Kilogram
KO	Knockout
Kras	Kirsten rat sarcoma viral oncogene
l	Liter
L-O-F	Loss of function
Lrg	Leucine-rich alpha-2-glycoprotei
Lrp	Low density lipoprotein receptor-related protein
log2	Binary logarithm
log10	Common logarithm
LoxP	Locus of crossover in P1
LPS	Lipopolysaccharide
LYVE1	Lymphatic vessel endothelial hyaluronic acid receptor 1
MAPK	Mitogen-activated protein kinase
mCherry	Monomeric Cherry
MHC	Major histocompatibility complex
min	Minutes
ml	Milliliter
mRNA	Messenger RNA
Ms	Murine
MYC	Avian myelocytomatosis viral oncogene
n.s.	Not significant
NaCl	Sodium chloride
NF	Nuclease free
NOD-SCID	Non obese diabetic- Severe Combined Immunodeficiency
O_2	Oxygen
P/S	Penicillin/streptomycin

Padj	Adjusted P value
PBS	Phosphate buffered saline
PC	Principal component
PCA	Principal component analysis
PCP	Planar cell polarity
PCR	Polymerase chain reaction
PDGF	Platelet-derived growth factor
PDGFR	Platelet-derived growth factor receptor
PDPN	Podoplanin
PE	Phycoerythrin
PFA	Paraformaldehyde
pH	Power of hydrogen
POCN	Porcupine
qPCR	Quantitative PCR
Rev	Reverse
RIN	RNA integrity number
RNA	Ribonucleic acid
RNAse	Ribonuclease
RNAseq	RNA sequencing
ROI	Region of interest
RT	Room temperature
s	Seconds
scRNAseq	Single cell RNAseq
SD	Standard deviation
SMART	Switching Mechanism At the end of the 5'-end of the RNA Transcript
ss	Single stranded
SSC	Side scatter
Taq	Thermus aquaticus
tatCherry	transactivator of transcription kappa (TATκ) peptide LP-mCherry
TBS(-T)	Tris-buffered saline (-Tween-20)
TC	Tumor cell
TER119	Lymphocyte antigen 76
TGF	Transforming growth factor
Tie	Tyrosine kinase with immunoglobulin and EGF homology domains
TSO	Template switching oligonucleotide
U	Unit
UMAP	Uniform manifold approximation and projection
UMI	Unique molecular identifier
UV	Ultra violet
v/v	Volume/volume
VCAM	Vascular cell adhesion protein
VE	Vascular endothelial
VEGF	Vascular endothelial growth factor
VEGFR	Vascular endothelial growth factor receptor
Vwf	Von Willebrand factor
w/o	Without

w/v	Weight/volume
WGBS	Whole genome bisulfite sequencing
Wls	Evenness wntless
Wnt	Wingless-related integration site
WT	Wildtype

Publications

Corresponding manuscript to thesis:

Jakab M*,#, Lee KH*, Uvarovskii A, Ovchinnikova S, Kulkarni SR, Rostalski T, Anders S, Augustin HG#. Lung endothelium instructs dormancy of susceptible metastatic tumour cells. *bioRxiv*, doi:2022.06.18.496680 (2022)
**Equal contribution, #corresponding author*

Additional published work:

Gehrs S, Jakab M, Gutjahr E, Gu Z, Weichenhahn D, Mogler C, Schlesner M, Plass C, Augustin HG, Schlereth K. Endothelial Dnmt3a controls placenta vascularization and function to support fetal growth. *bioRxiv*, doi:2022.07.28.501807 (2022)

Jakab M*, Rostalski T*, Lee KH, Mogler C, Augustin HG. Tie2 Receptor in Tumor-Infiltrating Macrophages Is Dispensable for Tumor Angiogenesis and Tumor Relapse after Chemotherapy. *Cancer Res.* **82**, 1353-1364, doi:10.1158/0008-5472.CAN-21-3181 (2022)
**Equal contribution*

Inverso D, Shi J, Lee KH, Jakab M, Ben-Moshe S, Kulkarni SR, Schneider M, Wang G, Komeili M, Vélez PA, Riedel M, Spegg C, Ruppert T, Schaeffer-Reiss C, Helm D, Singh I, Boutros M, Chintharlapalli S, Heikenwalder M, Itzkovitz S, Augustin HG. A spatial vascular transcriptomic, proteomic, and phosphoproteomic atlas unveils an angiocrine Tie-Wnt signaling axis in the liver. *Dev. Cell*. **56**, 1677-1693, doi:10.1016/j.devcel.2021.05.001 (2021)

Jakab M, Augustin HG. Understanding angiodiversity: insights from single cell biology. *Development* **147**, doi:10.1242/dev.146621 (2020)

References

1 Jaffe, E. A. Cell biology of endothelial cells. *Human pathology* **18**, 234-239, doi:10.1016/s0046-8177(87)80005-9 (1987).

2 Tucker, W. D., Arora, Y. & Mahajan, K. in *StatPearls* (StatPearls Publishing Copyright © 2022, StatPearls Publishing LLC., 2022).

3 Aird, W. C. Phenotypic heterogeneity of the endothelium. *Circ. Res.* **100**, 158-173, doi:10.1161/01.RES.0000255691.76142.4a (2007).

4 Aird, W. C. Phenotypic heterogeneity of the endothelium. *Circ. Res.* **100**, 174-190, doi:10.1161/01.RES.0000255690.03436.ae (2007).

5 Augustin, H. G. & Koh, G. Y. Organotypic vasculature: from descriptive heterogeneity to functional pathophysiology. *Science* **357**, doi:10.1126/science.aal2379 (2017).

6 Garlanda, C. & Dejana, E. Heterogeneity of endothelial cells. Specific markers. *Arterioscler. Thromb. Vasc. Biol.* **17**, 1193-1202, doi:10.1161/01.atv.17.7.1193 (1997).

7 Jakab, M. & Augustin, H. G. Understanding angiodiversity: insights from single cell biology. *Development* **147**, doi:10.1242/dev.146621 (2020).

8 Gillich, A. *et al.* Capillary cell-type specialization in the alveolus. *Nature* **586**, 785-789, doi:10.1038/s41586-020-2822-7 (2020).

9 Niethamer, T. K. *et al.* Defining the role of pulmonary endothelial cell heterogeneity in the response to acute lung injury. *Elife* **9**, doi:10.7554/eLife.53072 (2020).

10 Vila Ellis, L. *et al.* Epithelial Vegfa specifies a distinct endothelial population in the mouse lung. *Dev. Cell* **52**, 617-630.e616, doi:10.1016/j.devcel.2020.01.009 (2020).

11 Aizarani, N. *et al.* A human liver cell atlas reveals heterogeneity and epithelial progenitors. *Nature* **572**, 199-204, doi:10.1038/s41586-019-1373-2 (2019).

12 Halpern, K. B. *et al.* Paired-cell sequencing enables spatial gene expression mapping of liver endothelial cells. *Nat. Biotechnol.* **36**, 962-970, doi:10.1038/nbt.4231 (2018).

13 Halpern, K. B. *et al.* Single-cell spatial reconstruction reveals global division of labour in the mammalian liver. *Nature* **542**, 352-356, doi:10.1038/nature21065 (2017).

14 Inverso, D. *et al.* A spatial vascular transcriptomic, proteomic, and phosphoproteomic atlas unveils an angiocrine Tie-Wnt signaling axis in the liver. *Dev. Cell* **56**, 1677-1693.e1610, doi:10.1016/j.devcel.2021.05.001 (2021).

15 Koch, P.-S., Lee, K. H., Goerdt, S. & Augustin, H. G. Angiodiversity and organotypic functions of sinusoidal endothelial cells. *Angiogenesis* **24**, 289-310, doi:10.1007/s10456-021-09780-y (2021).

16 MacParland, S. A. *et al.* Single cell RNA sequencing of human liver reveals distinct intrahepatic macrophage populations. *Nat. Comm.* **9**, 4383, doi:10.1038/s41467-018-06318-7 (2018).

17 Mantovani, A. & Dejana, E. Cytokines as communication signals between leukocytes and endothelial cells. *Immunol. Today* **10**, 370-375, doi:10.1016/0167-5699(89)90270-3 (1989).

18 Lammert, E., Cleaver, O. & Melton, D. Induction of pancreatic differentiation by signals from blood vessels. *Science* **294**, 564-567, doi:10.1126/science.1064344 (2001).

19 Makita, T., Sucov, H. M., Gariepy, C. E., Yanagisawa, M. & Ginty, D. D. Endothelins are vascular-derived axonal guidance cues for developing sympathetic neurons. *Nature* **452**, 759-763, doi:10.1038/nature06859 (2008).

20 Matsumoto, K., Yoshitomi, H., Rossant, J. & Zaret, K. S. Liver organogenesis promoted by endothelial cells prior to vascular function. *Science* **294**, 559-563, doi:10.1126/science.1063889 (2001).

21 Ding, B. S. *et al.* Divergent angiocrine signals from vascular niche balance liver regeneration and fibrosis. *Nature* **505**, 97-102, doi:10.1038/nature12681 (2014).

22 Ding, B. S. *et al.* Inductive angiocrine signals from sinusoidal endothelium are required for liver regeneration. *Nature* **468**, 310-315, doi:10.1038/nature09493 (2010).

23 Hu, J. *et al.* Endothelial cell-derived angiopoietin-2 controls liver regeneration as a spatiotemporal rheostat. *Science* **343**, 416-419, doi:10.1126/science.1244880 (2014).

24 Lorenz, L. *et al.* Mechanosensing by β1 integrin induces angiocrine signals for liver growth and survival. *Nature* **562**, 128-132, doi:10.1038/s41586-018-0522-3 (2018).

25 Rafii, S., Butler, J. M. & Ding, B. S. Angiocrine functions of organ-specific endothelial cells. *Nature* **529**, 316-325, doi:10.1038/nature17040 (2016).

26 Gomez-Salinero, J. M., Itkin, T. & Rafii, S. Developmental angiocrine diversification of endothelial cells for organotypic regeneration. *Dev. Cell* **56**, 3042-3051, doi:10.1016/j.devcel.2021.10.020 (2021).

27 Cao, Z. *et al.* Targeting of the pulmonary capillary vascular niche promotes lung alveolar repair and ameliorates fibrosis. *Nat. Med.* **22**, 154-162, doi:10.1038/nm.4035 (2016).

28 Ding, B. S. *et al.* Endothelial-derived angiocrine signals induce and sustain regenerative lung alveolarization. *Cell* **147**, 539-553, doi.org/10.1016/j.cell.2011.10.003 (2011).

29 Hisata, S. *et al.* Reversal of emphysema by restoration of pulmonary endothelial cells. *J. Exp. Med.* **218**, doi:10.1084/jem.20200938 (2021).

30 Rafii, S. *et al.* Platelet-derived SDF-1 primes the pulmonary capillary vascular niche to drive lung alveolar regeneration. *Nat. Cell Biol.* **17**, 123-136, doi:10.1038/ncb3096 (2015).

31 Chen, Q. *et al.* Angiocrine Sphingosine-1-phosphate activation of S1PR2-YAP signaling axis in alveolar type II cells is essential for lung repair. *Cell Rep.* **31**, 107828, doi:10.1016/j.celrep.2020.107828 (2020).

32 Ryanto, G. R. T. *et al.* An endothelial activin A-bone morphogenetic protein receptor type 2 link is overdriven in pulmonary hypertension. *Nat. Comm.* **12**, 1720, doi:10.1038/s41467-021-21961-3 (2021).

33 Dumas, S. J. *et al.* Single-cell RNA sequencing reveals renal endothelium heterogeneity and metabolic adaptation to water deprivation. *J. Am. Soc. Nephrol.* **31**, 118-138, doi:10.1681/asn.2019080832 (2020).

34 Dumas, S. J. *et al.* Phenotypic diversity and metabolic specialization of renal endothelial cells. *Nat. Rev. Nephrol.* **17**, 441-464, doi:10.1038/s41581-021-00411-9 (2021).

35 Menon, R. *et al.* Single cell transcriptomics identifies focal segmental glomerulosclerosis remission endothelial biomarker. *JCI insight* **5**, doi:10.1172/jci.insight.133267 (2020).

36 Panigrahy, D. *et al.* Epoxyeicosanoids promote organ and tissue regeneration. *Proc. Natl. Acad. Sci. U. S. A.* **110**, 13528-13533, doi:10.1073/pnas.1311565110 (2013).

37 Leibing, T. *et al.* Angiocrine Wnt signaling controls liver growth and metabolic maturation in mice. *Hepatology* **68**, 707-722, doi:10.1002/hep.29613 (2018).

38 Rocha, A. S. *et al.* The angiocrine factor Rspondin3 is a key determinant of liver zonation. *Cell Rep.* **13**, 1757-1764, doi:10.1016/j.celrep.2015.10.049 (2015).

39 Wang, B., Zhao, L., Fish, M., Logan, C. Y. & Nusse, R. Self-renewing diploid Axin2(+) cells fuel homeostatic renewal of the liver. *Nature* **524**, 180-185, doi:10.1038/nature14863 (2015).

40 Zeng, G. *et al.* Wnt'er in liver: expression of Wnt and frizzled genes in mouse. *Hepatology* **45**, 195-204, doi:10.1002/hep.21473 (2007).

41 Preziosi, M., Okabe, H., Poddar, M., Singh, S. & Monga, S. P. Endothelial Wnts regulate β-catenin signaling in murine liver zonation and regeneration: a sequel to the Wnt–Wnt situation. *Hepatol. Commun.* **2**, 845-860, doi.org/10.1002/hep4.1196 (2018).

42 Baker, N. E. Molecular cloning of sequences from wingless, a segment polarity gene in Drosophila: the spatial distribution of a transcript in embryos. *EMBO J.* **6**, 1765-1773, doi:10.1002/j.1460-2075.1987.tb02429.x (1987).

43 Nusse, R. & Varmus, H. Three decades of Wnts: a personal perspective on how a scientific field developed. *EMBO J.* **31**, 2670-2684, doi:10.1038/emboj.2012.146 (2012).

44 Nusse, R. & Varmus, H. E. Many tumors induced by the mouse mammary tumor virus contain a provirus integrated in the same region of the host genome. *Cell* **31**, 99-109, doi:10.1016/0092-8674(82)90409-3 (1982).

45 Nüsslein-Volhard, C. & Wieschaus, E. Mutations affecting segment number and polarity in Drosophila. *Nature* **287**, 795-801, doi:10.1038/287795a0 (1980).

46 Rijsewijk, F. *et al.* The Drosophila homolog of the mouse mammary oncogene int-1 is identical to the segment polarity gene wingless. *Cell* **50**, 649-657, doi:10.1016/0092-8674(87)90038-9 (1987).

47 Sharma, R. P. & Chopra, V. L. Effect of the Wingless (wg1) mutation on wing and haltere development in Drosophila melanogaster. *Dev. Biol.* **48**, 461-465, doi:10.1016/0012-1606(76)90108-1 (1976).

48 Nusse, R. *et al.* A new nomenclature for int-1 and related genes: the Wnt gene family. *Cell* **64**, 231, doi:10.1016/0092-8674(91)90633-a (1991).

49 Nusse, R. & Clevers, H. Wnt/β-Catenin signaling, disease, and emerging therapeutic modalities. *Cell* **169**, 985-999, doi:10.1016/j.cell.2017.05.016 (2017).

50 Niehrs, C. The complex world of WNT receptor signalling. *Nat. Rev. Mol. Cell Biol.* **13**, 767-779, doi:10.1038/nrm3470 (2012).

51 Bartscherer, K. & Boutros, M. Regulation of Wnt protein secretion and its role in gradient formation. *EMBO Rep.* **9**, 977-982, doi:10.1038/embor.2008.167 (2008).

52 Bartscherer, K., Pelte, N., Ingelfinger, D. & Boutros, M. Secretion of Wnt ligands requires Evi, a conserved transmembrane protein. *Cell* **125**, 523-533, doi:10.1016/j.cell.2006.04.009 (2006).

53 van den Heuvel, M., Harryman-Samos, C., Klingensmith, J., Perrimon, N. & Nusse, R. Mutations in the segment polarity genes wingless and porcupine impair secretion of the wingless protein. *EMBO J.* **12**, 5293-5302, doi:10.1002/j.1460-2075.1993.tb06225.x (1993).

54 Kalucka, J. *et al.* Single-cell transcriptome atlas of murine endothelial cells. *Cell* **180**, 764-779, doi:10.1016/j.cell.2020.01.015 (2020).

55 Goddard, L. M. *et al.* Hemodynamic forces sculpt developing heart valves through a KLF2-WNT9B paracrine signaling axis. *Dev. Cell* **43**, 274-289, doi:10.1016/j.devcel.2017.09.023 (2017).

56 Zhou, B. *et al.* The angiocrine Rspondin3 instructs interstitial macrophage transition via metabolic–epigenetic reprogramming and resolves inflammatory injury. *Nat. Immunol.* **21**, 1430-1443, doi:10.1038/s41590-020-0764-8 (2020).

57 Korn, C. *et al.* Endothelial cell-derived non-canonical Wnt ligands control vascular pruning in angiogenesis. *Development* **141**, 1757-1766, doi:10.1242/dev.104422 (2014).

58 Scholz, B. *et al.* Endothelial RSPO3 controls vascular stability and pruning through non-canonical WNT/Ca2+/NFAT signaling. *Dev. Cell* **36**, 79-93, doi:https://doi.org/10.1016/j.devcel.2015.12.015 (2016).

59 Liu, Y. *et al.* A specialized bone marrow microenvironment for fetal haematopoiesis. *Nat. Commun.* **13**, 1327, doi:10.1038/s41467-022-28775-x (2022).

60 Itkin, T. *et al.* Distinct bone marrow blood vessels differentially regulate haematopoiesis. *Nature* **532**, 323-328, doi:10.1038/nature17624 (2016).

61 Kusumbe, A. P., Ramasamy, S. K. & Adams, R. H. Coupling of angiogenesis and osteogenesis by a specific vessel subtype in bone. *Nature* **507**, 323-328, doi:10.1038/nature13145 (2014).

62 Ramasamy, S. K. *et al.* Regulation of hematopoiesis and osteogenesis by blood vessel–derived signals. *Annu. Rev. Cell Dev. Biol.* **32**, 649-675, doi:10.1146/annurev-cellbio-111315-124936 (2016).

63 Ramasamy, S. K., Kusumbe, A. P., Wang, L. & Adams, R. H. Endothelial Notch activity promotes angiogenesis and osteogenesis in bone. *Nature* **507**, 376-380, doi:10.1038/nature13146 (2014).

64 Rohde, D. *et al.* Bone marrow endothelial dysfunction promotes myeloid cell expansion in cardiovascular disease. *Nat. Cardiovasc. Res.* **1**, 28-44, doi:10.1038/s44161-021-00002-8 (2022).

65 Tuckermann, J. & Adams, R. H. The endothelium-bone axis in development, homeostasis and bone and joint disease. *Nat. Rev. Rheumatol.* **17**, 608-620, doi:10.1038/s41584-021-00682-3 (2021).

66 Shen, Q. *et al.* Endothelial cells stimulate self-renewal and expand neurogenesis of neural stem cells. *Science* **304**, 1338-1340, doi:10.1126/science.1095505 (2004).

67 Shen, Q. *et al.* Adult SVZ stem cells lie in a vascular niche: a quantitative analysis of niche cell-cell interactions. *Cell Stem Cell* **3**, 289-300, doi: 10.1016/j.stem.2008.07.026 (2008).

68 Tavazoie, M. *et al.* A specialized vascular niche for adult neural stem cells. *Cell Stem Cell* **3**, 279-288, doi:10.1016/j.stem.2008.07.025 (2008).

69 Crisan, M. *et al.* A perivascular origin for mesenchymal stem cells in multiple human organs. *Cell Stem Cell* **3**, 301-313, doi:10.1016/j.stem.2008.07.003 (2008).

70 Tang, W. *et al.* White fat progenitor cells reside in the adipose vasculature. *Science* **322**, 583-586, doi:doi:10.1126/science.1156232 (2008).

71 Lazarus, A. *et al.* A perfusion-independent role of blood vessels in determining branching stereotypy of lung airways. *Development* **138**, 2359-2368, doi:10.1242/dev.060723 (2011).

72 Lu, P. & Werb, Z. Patterning mechanisms of branched organs. *Science* **322**, 1506-1509, doi:10.1126/science.1162783 (2008).

73 Magenheim, J. *et al.* Blood vessels restrain pancreas branching, differentiation and growth. *Development* **138**, 4743-4752, doi:10.1242/dev.066548 (2011).

74 Pierreux, C. E. *et al.* Epithelial: Endothelial cross-talk regulates exocrine differentiation in developing pancreas. *Dev. Biol.* **347**, 216-227, doi:10.1016/j.ydbio.2010.08.024 (2010).

75 Ramasamy, S. K., Kusumbe, A. P. & Adams, R. H. Regulation of tissue morphogenesis by endothelial cell-derived signals. *Trends Cell Biol.* **25**, 148-157, doi.org/10.1016/j.tcb.2014.11.007 (2015).

76 Rupnick, M. A. *et al.* Adipose tissue mass can be regulated through the vasculature. *Proc. Natl. Acad. Sci. U. S. A.* **99**, 10730-10735, doi:10.1073/pnas.162349799 (2002).

77 Woik, N. & Kroll, J. Regulation of lung development and regeneration by the vascular system. *Cell. Mol. Life Sci.* **72**, 2709-2718, doi:10.1007/s00018-015-1907-1 (2015).

78 Palikuqi, B. *et al.* Adaptable haemodynamic endothelial cells for organogenesis and tumorigenesis. *Nature* **585**, 426-432, doi:10.1038/s41586-020-2712-z (2020).

79 Pijuan-Sala, B. *et al.* A single-cell molecular map of mouse gastrulation and early organogenesis. *Nature* **566**, 490-495, doi:10.1038/s41586-019-0933-9 (2019).

80 Pijuan-Sala, B. *et al.* Single-cell chromatin accessibility maps reveal regulatory programs driving early mouse organogenesis. *Nat. Cell Biol.* **22**, 487-497, doi:10.1038/s41556-020-0489-9 (2020).

81 Baron, C. S. *et al.* Single-cell transcriptomics reveal the dynamic of haematopoietic stem cell production in the aorta. *Nat. Commun.* **9**, 2517, doi:10.1038/s41467-018-04893-3 (2018).

82 Bergiers, I. *et al.* Single-cell transcriptomics reveals a new dynamical function of transcription factors during embryonic hematopoiesis. *eLife* **7**, e29312, doi:10.7554/eLife.29312 (2018).

83 Chen, Michael J. *et al.* Erythroid/Myeloid Progenitors and Hematopoietic Stem Cells Originate from Distinct Populations of Endothelial Cells. *Cell Stem Cell* **9**, 541-552, doi:10.1016/j.stem.2011.10.003 (2011).

84 Kissa, K. & Herbomel, P. Blood stem cells emerge from aortic endothelium by a novel type of cell transition. *Nature* **464**, 112-115, doi:10.1038/nature08761 (2010).

85 Tanaka, H. Antiaging Effects of Aerobic Exercise on Systemic Arteries. *Hypertension* **74**, 237-243, doi:10.1161/HYPERTENSIONAHA.119.13179 (2019).

86 Yousef, H. *et al.* Aged blood impairs hippocampal neural precursor activity and activates microglia via brain endothelial cell VCAM1. *Nat. Med.* **25**, 988-1000, doi:10.1038/s41591-019-0440-4 (2019).

87 Chen, Y. *et al.* Aging reprograms the hematopoietic-vascular niche to impede regeneration and promote fibrosis. *Cell Metab.* **33**, 395-410, doi:10.1016/j.cmet.2020.11.019 (2021).

88 Ding, B. S. *et al.* Aging suppresses Sphingosine-1-phosphate chaperone ApoM in circulation resulting in maladaptive organ repair. *Dev. Cell* **53**, 677-690, doi:10.1016/j.devcel.2020.05.024 (2020).

89 Chen, J. *et al.* Decreased blood vessel density and endothelial cell subset dynamics during ageing of the endocrine system. *EMBO J.* **40**, e105242, doi:10.15252/embj.2020105242 (2021).

90 Chen, J. *et al.* High-resolution 3D imaging uncovers organ-specific vascular control of tissue aging. *Sci. Adv.* **7**, doi:10.1126/sciadv.abd7819 (2021).

91 Kusumbe, A. P. *et al.* Age-dependent modulation of vascular niches for haematopoietic stem cells. *Nature* **532**, 380-384, doi:10.1038/nature17638 (2016).

92 Grunewald, M. *et al.* Counteracting age-related VEGF signaling insufficiency promotes healthy aging and extends life span. *Science* **373**, eabc8479, doi:doi:10.1126/science.abc8479 (2021).

93 Vasudev, N. S. & Reynolds, A. R. Anti-angiogenic therapy for cancer: current progress, unresolved questions and future directions. *Angiogenesis* **17**, 471-494, doi:10.1007/s10456-014-9420-y (2014).

94 Gimbrone , M. A., Jr., Leapman , S. B., Cotran , R. S. & Folkman , J. Tumor dormancy in vivo by prevention of neovascularization. *J. Exp. Med.* **136**, 261-276, doi:10.1084/jem.136.2.261 (1972).

95 Algire, G. H., Chalkley, H. W., Legallais, F. Y. & Park, H. D. Vasculae reactions of normal and malignant tissues in vivo. I. Vascular reactions of mice to wounds and to normal and neoplastic transplants. *J. Natl. Cancer Inst.* **6**, 73-85, doi:10.1093/jnci/6.1.73 (1945).

96 Folkman, J. Tumor angiogenesis: therapeutic implications. *N. Engl. J. Med.* **285**, 1182-1186, doi:10.1056/nejm197111182852108 (1971).

97 Folkman, J., Merler, E., Abernathy, C. & Williams, G. Isolation of a tumor factor responsible for angiogenesis. *J. Exp. Med.* **133**, 275-288, doi:10.1084/jem.133.2.275 (1971).

98 Leung, D. W., Cachianes, G., Kuang, W.-J., Goeddel, D. V. & Ferrara, N. Vascular endothelial growth factor is a secreted angiogenic mitogen. *Science* **246**, 1306-1309, doi:10.1126/science.2479986 (1989).

99 Folkman, J. Angiogenesis in cancer, vascular, rheumatoid and other disease. *Nat. Med.* **1**, 27-30, doi:10.1038/nm0195-27 (1995).

100 Kim, K. J. *et al.* Inhibition of vascular endothelial growth factor-induced angiogenesis suppresses tumour growth in vivo. *Nature* **362**, 841-844, doi:10.1038/362841a0 (1993).

101 Mazzone, M. *et al.* Heterozygous deficiency of PHD2 restores tumor oxygenation and inhibits metastasis via endothelial normalization. *Cell* **136**, 839-851, doi.org/10.1016/j.cell.2009.01.020 (2009).

102 Cantelmo, A. R. *et al.* Inhibition of the glycolytic activator PFKFB3 in endothelium induces tumorvessel normalization, impairs metastasis, and improves chemotherapy. *Cancer Cell* **30**, 968-985, doi:10.1016/j.ccell.2016.10.006 (2016).

103 La Porta, S. *et al.* Endothelial Tie1-mediated angiogenesis and vascular abnormalization promote tumor progression and metastasis. *J. Clin. Invest.* **128**, 834-845, doi:10.1172/jci94674 (2018).

104 Singhal, M. *et al.* Preclinical validation of a novel metastasis-inhibiting Tie1 function-blocking antibody. *EMBO Mol. Med.* **12**, e11164, doi:10.15252/emmm.201911164 (2020).

105 Jain, R. K. Normalizing tumor vasculature with anti-angiogenic therapy: a new paradigm for combination therapy. *Nat. Med.* **7**, 987-989, doi:10.1038/nm0901-987 (2001).

106 Jászai, J. & Schmidt, M. H. H. Trends and challenges in tumor anti-angiogenic therapies. *Cells* **8**, doi:10.3390/cells8091102 (2019).

107 Finn, R. S. *et al.* Atezolizumab plus bevacizumab in unresectable hepatocellular carcinoma. *N. Engl. J. Med.* **382**, 1894-1905, doi:10.1056/NEJMoa1915745 (2020).

108 Zhu, A. X. *et al.* Molecular correlates of clinical response and resistance to atezolizumab in combination with bevacizumab in advanced hepatocellular carcinoma. *Nat. Med.*, doi:10.1038/s41591-022-01868-2 (2022).

109 Bernier-Latmani, J. *et al.* Apelin-driven endothelial cell migration sustains intestinal progenitor cells and tumor growth. *Nat. Cardiovasc. Res.* **1**, 476-490, doi:10.1038/s44161-022-00061-5 (2022).

110 Weinberg, R. A. A molecular basis of cancer. *Sci. Am.* **249**, 126-142, doi:10.1038/scientificamerican1183-126 (1983).

111 Brabletz, T., Kalluri, R., Nieto, M. A. & Weinberg, R. A. EMT in cancer. *Nat. Rev. Canc.* **18**, 128-134, doi:10.1038/nrc.2017.118 (2018).

112 Lambert, A. W., Pattabiraman, D. R. & Weinberg, R. A. Emerging biological principles of metastasis. *Cell* **168**, 670-691, doi:10.1016/j.cell.2016.11.037 (2017).

113 Chiang, A. C. & Massagué, J. Molecular basis of metastasis. *N. Engl. J. Med.* **359**, 2814-2823, doi:10.1056/NEJMra0805239 (2008).

114 Chaffer, C. L. & Weinberg, R. A. A perspective on cancer cell metastasis. *Science* **331**, 1559-1564, doi:10.1126/science.1203543 (2011).

115 Hanahan, D. & Weinberg, R. A. The hallmarks of cancer. *Cell* **100**, 57-70, doi.org/10.1016/S0092-8674(00)81683-9 (2000).

116 Hanahan, D. & Weinberg, Robert A. Hallmarks of cancer: the next generation. *Cell* **144**, 646-674, doi.org/10.1016/j.cell.2011.02.013 (2011).

117 Hanahan, D. Hallmarks of cancer: new dimensions. *Cancer Discovery* **12**, 31-46, doi:10.1158/2159-8290.Cd-21-1059 (2022).

118 Paget, S. The distribution of secondary growths in cancer of the breast. *The Lancet* **133**, 571-573, doi.org/10.1016/S0140-6736(00)49915-0 (1889).

119 Kaplan, R. N. *et al.* VEGFR1-positive haematopoietic bone marrow progenitors initiate the pre-metastatic niche. *Nature* **438**, 820-827, doi:10.1038/nature04186 (2005).

120 Peinado, H. *et al.* Melanoma exosomes educate bone marrow progenitor cells toward a pro-metastatic phenotype through MET. *Nat. Med.* **18**, 883-891, doi:10.1038/nm.2753 (2012).

121 Costa-Silva, B. *et al.* Pancreatic cancer exosomes initiate pre-metastatic niche formation in the liver. *Nat. Cell Biol.* **17**, 816-826, doi:10.1038/ncb3169 (2015).

122 Hoshino, A. *et al.* Tumour exosome integrins determine organotropic metastasis. *Nature* **527**, 329-335, doi:10.1038/nature15756 (2015).

123 Peinado, H. *et al.* Pre-metastatic niches: organ-specific homes for metastases. *Nat. Rev. Canc.* **17**, 302-317, doi:10.1038/nrc.2017.6 (2017).

124 Rodrigues, G. *et al.* Tumour exosomal CEMIP protein promotes cancer cell colonization in brain metastasis. *Nat. Cell Biol.* **21**, 1403-1412, doi:10.1038/s41556-019-0404-4 (2019).

125 Hoshino, A. *et al.* Extracellular vesicle and particle biomarkers define multiple human cancers. *Cell* **182**, 1044-1061.e1018, doi:10.1016/j.cell.2020.07.009 (2020).

126 García-Silva, S. *et al.* Melanoma-derived small extracellular vesicles induce lymphangiogenesis and metastasis through an NGFR-dependent mechanism. *Nat. Cancer* **2**, 1387-1405, doi:10.1038/s43018-021-00272-y (2021).

127 Padua, D. *et al.* TGFβ primes breast tumors for lung metastasis seeding through Angiopoietin-like 4. *Cell* **133**, 66-77, doi.org/10.1016/j.cell.2008.01.046 (2008).

128 Murgai, M. *et al.* KLF4-dependent perivascular cell plasticity mediates pre-metastatic niche formation and metastasis. *Nat. Med.* **23**, 1176-1190, doi:10.1038/nm.4400 (2017).

129 Singhal, M. *et al.* Temporal multi-omics identifies LRG1 as a vascular niche instructor of metastasis. *Sci. Transl. Med.* **13**, eabe6805, doi:10.1126/scitranslmed.abe6805 (2021).

130 Hongu, T. *et al.* Perivascular tenascin C triggers sequential activation of macrophages and endothelial cells to generate a pro-metastatic vascular niche in the lungs. *Nat. Cancer* **3**, 486-504, doi:10.1038/s43018-022-00353-6 (2022).

131 McAllister, S. S. & Weinberg, R. A. The tumour-induced systemic environment as a critical regulator of cancer progression and metastasis. *Nat. Cell Biol.* **16**, 717-727, doi:10.1038/ncb3015 (2014).

132 Harper, K. L. *et al.* Mechanism of early dissemination and metastasis in Her2(+) mammary cancer. *Nature* **540**, 588-592, doi:10.1038/nature20609 (2016).

133 Hosseini, H. *et al.* Early dissemination seeds metastasis in breast cancer. *Nature* **540**, 552-558, doi:10.1038/nature20785 (2016).

134 Hüsemann, Y. *et al.* Systemic spread is an early step in breast cancer. *Cancer Cell* **13**, 58-68, doi:10.1016/j.ccr.2007.12.003 (2008).

135 Podsypanina, K. *et al.* Seeding and propagation of untransformed mouse mammary cells in the lung. *Science* **321**, 1841-1844, doi:10.1126/science.1161621 (2008).

136 Obradović, M. M. S. *et al.* Glucocorticoids promote breast cancer metastasis. *Nature* **567**, 540-544, doi:10.1038/s41586-019-1019-4 (2019).

137 Klein, C. A. Parallel progression of primary tumours and metastases. *Nat. Rev. Canc.* **9**, 302-312, doi:10.1038/nrc2627 (2009).

138 Klein, C. A. Cancer progression and the invisible phase of metastatic colonization. *Nat. Rev. Canc.* **20**, 681-694, doi:10.1038/s41568-020-00300-6 (2020).

139 Ghajar, C. M. Metastasis prevention by targeting the dormant niche. *Nat. Rev. Canc.* **15**, 238-247, doi:10.1038/nrc3910 (2015).

140 Gupta, G. P. *et al.* Mediators of vascular remodelling co-opted for sequential steps in lung metastasis. *Nature* **446**, 765-770, doi:10.1038/nature05760 (2007).

141 Srivastava, K. *et al.* Postsurgical adjuvant tumor therapy by combining anti-angiopoietin-2 and metronomic chemotherapy limits metastatic growth. *Cancer Cell* **26**, 880-895, doi:10.1016/j.ccell.2014.11.005 (2014).

142 Kim, K. J. *et al.* STAT3 activation in endothelial cells is important for tumor metastasis via increased cell adhesion molecule expression. *Oncogene* **36**, 5445-5459, doi:10.1038/onc.2017.148 (2017).

143 Tavora, B. *et al.* Tumoural activation of TLR3-SLIT2 axis in endothelium drives metastasis. *Nature* **586**, 299-304, doi:10.1038/s41586-020-2774-y (2020).

144 Cao, Z. *et al.* Angiocrine factors deployed by tumor vascular niche induce B cell lymphoma invasiveness and chemoresistance. *Cancer Cell* **25**, 350-365, doi:10.1016/j.ccr.2014.02.005 (2014).

145 Cunha, S. I. *et al.* Endothelial ALK1 is a therapeutic target to block metastatic dissemination of breast cancer. *Cancer Res.* **75**, 2445-2456, doi:10.1158/0008-5472.Can-14-3706 (2015).

146 Wieland, E. *et al.* Endothelial Notch1 activity facilitates metastasis. *Cancer Cell* **31**, 355-367, doi.org/10.1016/j.ccell.2017.01.007 (2017).

147 Esposito, M. *et al.* Bone vascular niche E-selectin induces mesenchymal–epithelial transition and Wnt activation in cancer cells to promote bone metastasis. *Nat. Cell Biol.* **21**, 627-639, doi:10.1038/s41556-019-0309-2 (2019).

148 Yip, R. K. H. *et al.* Mammary tumour cells remodel the bone marrow vascular microenvironment to support metastasis. *Nat. Commun.* **12**, 6920, doi:10.1038/s41467-021-26556-6 (2021).

149 Schumacher, D., Strilic, B., Sivaraj, K. K., Wettschureck, N. & Offermanns, S. Response to Harper et al. *Cancer Cell* **24**, 288, doi:10.1016/j.ccr.2013.08.015 (2013).

150 Bolik, J. *et al.* Inhibition of ADAM17 impairs endothelial cell necroptosis and blocks metastasis. *J. Exp. Med.* **219**, doi:10.1084/jem.20201039 (2022).

151 Strilic, B. *et al.* Tumour-cell-induced endothelial cell necroptosis via death receptor 6 promotes metastasis. *Nature* **536**, 215-218, doi:10.1038/nature19076 (2016).

152 Wettschureck, N., Strilic, B. & Offermanns, S. Passing the vascular barrier: endothelial signaling processes controlling extravasation. *Physiol. Rev.* **99**, 1467-1525, doi:10.1152/physrev.00037.2018 (2019).

153 Yang, L. *et al.* TAK1 regulates endothelial cell necroptosis and tumor metastasis. *Cell Death Differ.* **26**, 1987-1997, doi:10.1038/s41418-018-0271-8 (2019).

154 Kuczynski, E. A., Vermeulen, P. B., Pezzella, F., Kerbel, R. S. & Reynolds, A. R. Vessel co-option in cancer. *Nat. Rev. Clin. Oncol.* **16**, 469-493, doi:10.1038/s41571-019-0181-9 (2019).

155 Teuwen, L. A. *et al.* Tumor vessel co-option probed by single-cell analysis. *Cell Rep.* **35**, 109253, doi:10.1016/j.celrep.2021.109253 (2021).

156 Valiente, M. *et al.* Serpins promote cancer cell survival and vascular co-option in brain metastasis. *Cell* **156**, 1002-1016, doi.org/10.1016/j.cell.2014.01.040 (2014).

157 Er, E. E. *et al.* Pericyte-like spreading by disseminated cancer cells activates YAP and MRTF for metastatic colonization. *Nat. Cell Biol.* **20**, 966-978, doi:10.1038/s41556-018-0138-8 (2018).

158 Al-Mehdi, A. B. *et al.* Intravascular origin of metastasis from the proliferation of endothelium-attached tumor cells: a new model for metastasis. *Nat. Med.* **6**, 100-102, doi:10.1038/71429 (2000).

159 Wong, C. W. *et al.* Intravascular location of breast cancer cells after spontaneous metastasis to the lung. *Am. J. Pathol.* **161**, 749-753, doi:10.1016/s0002-9440(10)64233-2 (2002).

160 Risson, E., Nobre, A. R., Maguer-Satta, V. & Aguirre-Ghiso, J. A. The current paradigm and challenges ahead for the dormancy of disseminated tumor cells. *Nat. Cancer* **1**, 672-680, doi:10.1038/s43018-020-0088-5 (2020).

161 Crist, S. B. & Ghajar, C. M. When a house is not a home: a survey of antimetastatic niches and potential mechanisms of disseminated tumor cell suppression. *Annu. Rev. Pathol.* **16**, 409-432, doi:10.1146/annurev-pathmechdis-012419-032647 (2021).

162 Goddard, E. T., Bozic, I., Riddell, S. R. & Ghajar, C. M. Dormant tumour cells, their niches and the influence of immunity. *Nat. Cell Biol.* **20**, 1240-1249, doi:10.1038/s41556-018-0214-0 (2018).

163 Ghajar, C. M. *et al.* The perivascular niche regulates breast tumour dormancy. *Nat. Cell Biol.* **15**, 807-817, doi:10.1038/ncb2767 (2013).

164 Bragado, P. *et al.* TGF-β2 dictates disseminated tumour cell fate in target organs through TGF-β-RIII and p38α/β signalling. *Nat. Cell Biol.* **15**, 1351-1361, doi:10.1038/ncb2861 (2013).

165 Nobre, A. R. *et al.* Bone marrow NG2(+)/Nestin(+) mesenchymal stem cells drive DTC dormancy via TGFβ2. *Nat. Cancer* **2**, 327-339, doi:10.1038/s43018-021-00179-8 (2021).

166 Ren, D. *et al.* Wnt5a induces and maintains prostate cancer cells dormancy in bone. *J. Exp. Med.* **216**, 428-449, doi:10.1084/jem.20180661 (2019).

167 Malladi, S. *et al.* Metastatic latency and immune evasion through autocrine inhibition of WNT. *Cell* **165**, 45-60, doi.org/10.1016/j.cell.2016.02.025 (2016).

168 Fane, M. E. *et al.* Stromal changes in the aged lung induce an emergence from melanoma dormancy. *Nature* **606**, 396-405, doi:10.1038/s41586-022-04774-2 (2022).

169 Hendrikx, S. *et al.* Endothelial calcineurin signaling restrains metastatic outgrowth by regulating Bmp2. *Cell Rep.* **26**, 1227-1241.e1226, doi:10.1016/j.celrep.2019.01.016 (2019).

170 Crist, S. B. *et al.* Unchecked oxidative stress in skeletal muscle prevents outgrowth of disseminated tumour cells. *Nat. Cell Biol.* **24**, 538-553, doi:10.1038/s41556-022-00881-4 (2022).

171 Dai, J. *et al.* Astrocytic laminin-211 drives disseminated breast tumor cell dormancy in brain. *Nat. Cancer* **3**, 25-42, doi:10.1038/s43018-021-00297-3 (2022).

172 Di Martino, J. S. *et al.* A tumor-derived type III collagen-rich ECM niche regulates tumor cell dormancy. *Nat. Cancer* **3**, 90-107, doi:10.1038/s43018-021-00291-9 (2022).

173 Shibue, T., Reinhardt, F. & Weinberg, R. A. Syndecan-mediated ligation of ECM proteins triggers proliferative arrest of disseminated tumor cells. *Cancer Res.* **79**, 5944-5957, doi:10.1158/0008-5472.Can-19-1165 (2019).

174 Carlson, P. *et al.* Targeting the perivascular niche sensitizes disseminated tumour cells to chemotherapy. *Nat. Cell Biol.* **21**, 238-250, doi:10.1038/s41556-018-0267-0 (2019).

175 Albrengues, J. *et al.* Neutrophil extracellular traps produced during inflammation awaken dormant cancer cells in mice. *Science* **361**, doi:10.1126/science.aao4227 (2018).

176 Krall, J. A. *et al.* The systemic response to surgery triggers the outgrowth of distant immune-controlled tumors in mouse models of dormancy. *Sci. Transl. Med.* **10**, doi:10.1126/scitranslmed.aan3464 (2018).

177 De Cock, J. M. *et al.* Inflammation triggers Zeb1-dependent escape from tumor latency. *Cancer Res* **76**, 6778-6784, doi:10.1158/0008-5472.Can-16-0608 (2016).

178 Correia, A. L. *et al.* Hepatic stellate cells suppress NK cell-sustained breast cancer dormancy. *Nature* **594**, 566-571, doi:10.1038/s41586-021-03614-z (2021).

179 Borriello, L. *et al.* Primary tumor associated macrophages activate programs of invasion and dormancy in disseminating tumor cells. *Nat. Commun.* **13**, 626, doi:10.1038/s41467-022-28076-3 (2022).

180 Fluegen, G. *et al.* Phenotypic heterogeneity of disseminated tumour cells is preset by primary tumour hypoxic microenvironments. *Nat. Cell Biol.* **19**, 120-132, doi:10.1038/ncb3465 (2017).

181 Quinn, J. J. *et al.* Single-cell lineages reveal the rates, routes, and drivers of metastasis in cancer xenografts. *Science* **371**, doi:10.1126/science.abc1944 (2021).

182 Simeonov, K. P. *et al.* Single-cell lineage tracing of metastatic cancer reveals selection of hybrid EMT states. *Cancer Cell* **39**, 1150-1162, doi:10.1016/j.ccell.2021.05.005 (2021).

183 Mehlen, P. & Puisieux, A. Metastasis: a question of life or death. *Nat. Rev. Canc.* **6**, 449-458, doi:10.1038/nrc1886 (2006).

184 Butler, T. P. & Gullino, P. M. Quantitation of cell shedding into efferent blood of mammary adenocarcinoma. *Cancer Res.* **35**, 512-516 (1975).

185 Picelli, S. *et al.* Full-length RNA-seq from single cells using Smart-seq2. *Nat. Protoc.* **9**, 171-181, doi:10.1038/nprot.2014.006 (2014).

186 Tammela, T. *et al.* A Wnt-producing niche drives proliferative potential and progression in lung adenocarcinoma. *Nature* **545**, 355-359, doi:10.1038/nature22334 (2017).

187 Efremova, M., Vento-Tormo, M., Teichmann, S. A. & Vento-Tormo, R. CellPhoneDB: inferring cell-cell communication from combined expression of multi-subunit ligand-receptor complexes. *Nat. Protoc.* **15**, 1484-1506, doi:10.1038/s41596-020-0292-x (2020).

188 Ombrato, L. *et al.* Metastatic-niche labelling reveals parenchymal cells with stem features. *Nature* **572**, 603-608, doi:10.1038/s41586-019-1487-6 (2019).

189 Goveia, J. *et al.* An integrated gene expression landscape profiling approach to identify lung tumor endothelial cell heterogeneity and angiogenic candidates. *Cancer Cell* **37**, 421, doi:10.1016/j.ccell.2020.03.002 (2020).

190 Cheng, Y. H. *et al.* Hydro-Seq enables contamination-free high-throughput single-cell RNA-sequencing for circulating tumor cells. *Nat. Commun.* **10**, 2163, doi:10.1038/s41467-019-10122-2 (2019).

191 Szczerba, B. M. *et al.* Neutrophils escort circulating tumour cells to enable cell cycle progression. *Nature* **566**, 553-557, doi:10.1038/s41586-019-0915-y (2019).

192 Gkountela, S. *et al.* Circulating tumor cell clustering shapes DNA methylation to enable metastasis seeding. *Cell* **176**, 98-112, doi:10.1016/j.cell.2018.11.046 (2019).

193 Liberzon, A. *et al.* The Molecular Signatures Database (MSigDB) hallmark gene set collection. *Cell Syst.* **1**, 417-425, doi:10.1016/j.cels.2015.12.004 (2015).

194 Emert, B. L. *et al.* Variability within rare cell states enables multiple paths toward drug resistance. *Nat. Biotechnol.* **39**, 865-876, doi:10.1038/s41587-021-00837-3 (2021).

195 Shaffer, S. M. *et al.* Rare cell variability and drug-induced reprogramming as a mode of cancer drug resistance. *Nature* **546**, 431-435, doi:10.1038/nature22794 (2017).

196 Shaffer, S. M. *et al.* Memory sequencing reveals heritable single-cell gene expression programs associated with distinct cellular behaviors. *Cell* **182**, 947-959, doi:10.1016/j.cell.2020.07.003 (2020).

197 Torre, E. A. *et al.* Genetic screening for single-cell variability modulators driving therapy resistance. *Nat. Genet.* **53**, 76-85, doi:10.1038/s41588-020-00749-z (2021).

198 Pattabiraman, D. R. *et al.* Activation of PKA leads to mesenchymal-to-epithelial transition and loss of tumor-initiating ability. *Science* **351**, aad3680, doi:10.1126/science.aad3680 (2016).

199 Zhang, Y. *et al.* Genome-wide CRISPR screen identifies PRC2 and KMT2D-COMPASS as regulators of distinct EMT trajectories that contribute differentially to metastasis. *Nat. Cell Biol.* **24**, 554-564, doi:10.1038/s41556-022-00877-0 (2022).

200 Sosa, M. S. *et al.* NR2F1 controls tumour cell dormancy via SOX9- and RARβ-driven quiescence programmes. *Nat. Commun.* **6**, 6170, doi:10.1038/ncomms7170 (2015).

201 Fumagalli, A. *et al.* Plasticity of Lgr5-negative cancer cells drives metastasis in colorectal cancer. *Cell Stem Cell* **26**, 569-578, doi:10.1016/j.stem.2020.02.008 (2020).

202 Pastushenko, I. *et al.* Identification of the tumour transition states occurring during EMT. *Nature* **556**, 463-468, doi:10.1038/s41586-018-0040-3 (2018).

203 Pastushenko, I. *et al.* Fat1 deletion promotes hybrid EMT state, tumour stemness and metastasis. *Nature* **589**, 448-455, doi:10.1038/s41586-020-03046-1 (2021).

204 Yu, M. *et al.* RNA sequencing of pancreatic circulating tumour cells implicates WNT signalling in metastasis. *Nature* **487**, 510-513, doi:10.1038/nature11217 (2012).

205 Miyamoto, D. T. *et al.* RNA-Seq of single prostate CTCs implicates noncanonical Wnt signaling in antiandrogen resistance. *Science* **349**, 1351-1356, doi:10.1126/science.aab0917 (2015).

206 Warner, D. R., Greene, R. M. & Pisano, M. M. Cross-talk between the TGFbeta and Wnt signaling pathways in murine embryonic maxillary mesenchymal cells. *FEBS Lett.* **579**, 3539-3546, doi:10.1016/j.febslet.2005.05.024 (2005).

207 Montagner, M. *et al.* Crosstalk with lung epithelial cells regulates Sfrp2-mediated latency in breast cancer dissemination. *Nat. Cell Biol.* **22**, 289-296, doi:10.1038/s41556-020-0474-3 (2020).

208 Pein, M. *et al.* Metastasis-initiating cells induce and exploit a fibroblast niche to fuel malignant colonization of the lungs. *Nat. Commun.* **11**, 1494, doi:10.1038/s41467-020-15188-x (2020).

209 Singh, A. *et al.* Angiocrine signals regulate quiescence and therapy resistance in bone metastasis. *JCI Insight* **4**, doi:10.1172/jci.insight.125679 (2019).

210 Werner-Klein, M. *et al.* Interleukin-6 trans-signaling is a candidate mechanism to drive progression of human DCCs during clinical latency. *Nat. Commun.* **11**, 4977, doi:10.1038/s41467-020-18701-4 (2020).

211 Liu, J. *et al.* Targeting Wnt-driven cancer through the inhibition of Porcupine by LGK974. *Proc. Natl. Acad. Sci. U. S. A.* **110**, 20224-20229, doi:10.1073/pnas.1314239110 (2013).

212 Livak, K. J. & Schmittgen, T. D. Analysis of relative gene expression data using real-time quantitative PCR and the 2(-Delta Delta C(T)) Method. *Methods* **25**, 402-408, doi:10.1006/meth.2001.1262 (2001).

213 Patro, R., Duggal, G., Love, M. I., Irizarry, R. A. & Kingsford, C. Salmon provides fast and bias-aware quantification of transcript expression. *Nat. Methods* **14**, 417-419, doi:10.1038/nmeth.4197 (2017).

214 Soneson, C., Love, M. I. & Robinson, M. D. Differential analyses for RNA-seq: transcript-level estimates improve gene-level inferences. *F1000Research* **4**, 1521, doi:10.12688/f1000research.7563.2 (2015).

215 Love, M. I., Huber, W. & Anders, S. Moderated estimation of fold change and dispersion for RNA-seq data with DESeq2. *Genome Biol.* **15**, 550, doi:10.1186/s13059-014-0550-8 (2014).

216 Mootha, V. K. *et al.* PGC-1alpha-responsive genes involved in oxidative phosphorylation are coordinately downregulated in human diabetes. *Nat. Genet.* **34**, 267-273, doi:10.1038/ng1180 (2003).

217 Subramanian, A. *et al.* Gene set enrichment analysis: a knowledge-based approach for interpreting genome-wide expression profiles. *Proc. Natl. Acad. Sci. U. S. A.* **102**, 15545-15550, doi:10.1073/pnas.0506580102 (2005).

218 Yu, G., Wang, L. G., Han, Y. & He, Q. Y. clusterProfiler: an R package for comparing biological themes among gene clusters. *OMICS J. Integr. Biol.* **16**, 284-287, doi:10.1089/omi.2011.0118 (2012).

219 Hao, Y. *et al.* Integrated analysis of multimodal single-cell data. *Cell* **184**, 3573-3587, doi:10.1016/j.cell.2021.04.048 (2021).

220 Stuart, T. *et al.* Comprehensive integration of single-cell data. *Cell* **177**, 1888-1902, doi:10.1016/j.cell.2019.05.031 (2019).

221 Tirosh, I. *et al.* Dissecting the multicellular ecosystem of metastatic melanoma by single-cell RNA-seq. *Science* **352**, 189-196, doi:10.1126/science.aad0501 (2016).

222 Qiu, X. *et al.* Reversed graph embedding resolves complex single-cell trajectories. *Nat. Methods* **14**, 979-982, doi:10.1038/nmeth.4402 (2017).

223 Trapnell, C. *et al.* The dynamics and regulators of cell fate decisions are revealed by pseudotemporal ordering of single cells. *Nat. Biotechnol.* **32**, 381-386, doi:10.1038/nbt.2859 (2014).

224 Krueger F, Trimgalore, GitHub repository, https://github.com/FelixKrueger/TrimGalore, doi: 10.5281/zenodo.5127899 (2021)

225 Krueger, F. & Andrews, S. R. Bismark: a flexible aligner and methylation caller for Bisulfite-Seq applications. *Bioinformatics* **27**, 1571-1572, doi:10.1093/bioinformatics/btr167 (2011).

226 Hansen, K. D., Langmead, B. & Irizarry, R. A. BSmooth: from whole genome bisulfite sequencing reads to differentially methylated regions. *Genome Biol.* **13**, R83, doi:10.1186/gb-2012-13-10-r83 (2012).

227 Cunningham, F. *et al.* Ensembl 2022. *Nucleic Acids Res.* **50**, D988-D995, doi:10.1093/nar/gkab1049 (2021).